

MULTICHANNEL METHODS FOR RESTORATION IN COMPUTED IMAGING

Robert Lee Morrison, Jr., Ph.D.

Department of Electrical and Computer Engineering

University of Illinois at Urbana-Champaign, 2007

Minh N. Do, Adviser

This dissertation addresses data-driven image restoration for computed imaging systems. The work is focused on problems in two imaging modalities: the autofocus problem in synthetic aperture radar (SAR), and the problem of estimating coil sensitivities in parallel magnetic resonance imaging (PMRI). A common thread in both problems is their inherent multichannel nature, i.e., both exhibit special structure due to the redundancy provided by multiple signal measurements. By explicitly exploiting the multichannel structure, novel algorithms are developed offering improved restoration performance. We first present a theoretical study providing more insight into metric-based SAR autofocus techniques. Our analytical results show how metric-based methods implicitly rely on the multichannel defocusing model of SAR autofocus to form well-focused restorations. Utilizing the multichannel structure of the SAR autofocus problem explicitly, we develop a new noniterative restoration approach termed the MultiChannel Autofocus (MCA) algorithm. In this approach, the focused image is directly recovered using a linear algebraic formulation. Experimental results using actual and simulated SAR data demonstrate that MCA provides superior performance in comparison with existing autofocus methods. Lastly, we develop a new subspace-based approach for estimating receiver coil sensitivity functions used in PMRI reconstruction. Our approach does not rely on sum-of-squares assumptions used in previous PMRI techniques, thus avoiding potential problems such as poor image contrast and aliasing artifacts.

MULTICHANNEL METHODS FOR RESTORATION IN COMPUTED IMAGING

BY

ROBERT LEE MORRISON, JR.

B.S.E., University of Iowa, 2000
M.S., University of Illinois at Urbana-Champaign, 2002

DISSERTATION

Submitted in partial fulfillment of the requirements
for the degree of Doctor of Philosophy in Electrical and Computer Engineering
in the Graduate College of the
University of Illinois at Urbana-Champaign, 2007

Urbana, Illinois

© 2007 by Robert Lee Morrison, Jr. All rights reserved.

ABSTRACT

This dissertation addresses data-driven image restoration for computed imaging systems. The work is focused on problems in two imaging modalities: the autofocus problem in synthetic aperture radar (SAR), and the problem of estimating coil sensitivities in parallel magnetic resonance imaging (PMRI). A common thread in both problems is their inherent multichannel nature, i.e., both exhibit special structure due to the redundancy provided by multiple signal measurements. By explicitly exploiting the multichannel structure, novel algorithms are developed offering improved restoration performance. We first present a theoretical study providing more insight into metric-based SAR autofocus techniques. Our analytical results show how metric-based methods implicitly rely on the multichannel defocusing model of SAR autofocus to form well-focused restorations. Utilizing the multichannel structure of the SAR autofocus problem explicitly, we develop a new noniterative restoration approach termed the MultiChannel Autofocus (MCA) algorithm. In this approach, the focused image is directly recovered using a linear algebraic formulation. Experimental results using actual and simulated SAR data demonstrate that MCA provides superior performance in comparison with existing autofocus methods. Lastly, we develop a new subspace-based approach for estimating receiver coil sensitivity functions used in PMRI reconstruction. Our approach does not rely on sum-of-squares assumptions used in previous PMRI techniques, thus avoiding potential problems such as poor image contrast and aliasing artifacts.

To My Family

ACKNOWLEDGMENTS

I would first like to thank my thesis advisor, Prof. Minh N. Do, whose insight and vision have made this thesis possible. I credit Prof. Do with helping me to reach maturity as a researcher. His creativity and energy have been a powerful inspiration to me. Prof. Do's important role as a mentor and friend will leave a lasting imprint upon me in all of my future endeavors.

Second, I thank Prof. David C. Munson Jr. of the University of Michigan for his guidance, friendship, and continuing support. I am indebted to him for introducing me to the field of signal processing and the unique application of synthetic aperture radar.

Additionally, I thank Prof. Mathews Jacob of the University of Rochester for his valuable insight and contributions to the work in parallel magnetic resonance imaging presented in this thesis. I would also like to acknowledge Prof. Bradley Sutton for insightful discussions related to my work in magnetic resonance imaging, and Dr. Thomas Kragh of MIT Lincoln Laboratory for stimulating exchanges about the synthetic aperture radar autofocus problem.

I am grateful to friends in my graduate program. In particular, I would like to acknowledge Mark Butala, Dr. Jeffrey Brokish, Dr. Tyler Ralston, and Dr. Serdar Yuksel for their support and encouragement. I would also like to give heartfelt thanks to all the members of Prof. Do's research group for their support and friendship.

I would like to thank Prof. Yoram Bresler, Prof. Douglas Jones, and Prof. Farzad Kamalabadi for their service on my Ph.D. committee, and for their advice and feedback.

Lastly, I thank my wife Beth and my parents for their love and encouragement on my journey.

TABLE OF CONTENTS

LIST OF TABLES	ix
LIST OF FIGURES	x
CHAPTER 1 INTRODUCTION	1
1.1 Motivation	1
1.2 Dissertation Contribution	3
CHAPTER 2 BACKGROUND	6
2.1 The SAR Autofocus Problem	6
2.1.1 Problem statement	6
2.1.2 Existing approaches to SAR autofocus	11
2.2 Estimation of Coil Sensitivities in PMRI	13
2.2.1 Problem setup	13
2.2.2 Existing approaches to PMRI reconstruction	16
2.2.3 PMRI reconstruction using SENSE	18
2.2.4 PMRI reconstruction using GRAPPA	19
CHAPTER 3 SAR IMAGE AUTOFOCUS BY SHARPNESS OPTIMIZATION: A THEORETICAL STUDY	21
3.1 Introduction	21
3.2 Problem Setup	23
3.2.1 SAR image models	23
3.2.2 Image sharpness metrics	23
3.2.3 SAR autofocus as an optimization problem	24
3.3 Analysis of Single-Column Image Models	25
3.3.1 Approximate expressions for the objective function	25
3.3.2 Validation of the approximate expression	28
3.4 Analysis of Multicolumn Image Models	29
3.4.1 Asymptotic analysis	29
3.4.2 Quantitative analysis for a finite number of columns	32
3.4.3 Validation of analytical results	33
3.5 Separable Approximation for the Multivariate Objective Function	35
3.6 Experimental Results	37

CHAPTER 4 MCA: A MULTICHANNEL APPROACH TO SAR	
AUTOFOCUS	42
4.1 Introduction	42
4.2 Problem Setup	45
4.2.1 Notation	45
4.2.2 Problem description and characterization of the solution space	45
4.3 MCA Restoration Framework	46
4.3.1 Explicit multichannel condition	46
4.3.2 MCA direct solution approach	48
4.3.3 Restoration using the SVD	49
4.4 Performance Analysis	50
4.4.1 General properties of $\Phi_{\Omega}(\tilde{\mathbf{g}})$	50
4.4.2 Special case: Low-return rows	53
4.4.3 Efficient restoration procedure	56
4.5 Application of Sharpness Metric Optimization to MCA	57
4.5.1 Bringing metrics to the MCA framework	57
4.5.2 Performing the metric optimization	59
4.6 SAR Data Acquisition and Processing	60
4.7 Experimental Results	63
CHAPTER 5 MULTICHANNEL ESTIMATION OF COIL	
SENSITIVITIES IN PARALLEL MRI	72
5.1 Introduction	72
5.2 Problem Formulation	74
5.3 Reconstruction Framework	76
5.3.1 Subspace-based framework	76
5.3.2 Uniqueness of solutions	77
5.3.2.1 General basis expansion	77
5.3.2.2 Special case: Polynomial basis expansion	79
5.3.3 Estimation of coil sensitivities	81
5.3.4 Efficient estimation procedure	83
5.3.5 Constructing the basis functions	84
5.3.6 Validation of assumptions in the proposed technique	86
5.4 Coil Estimation and Reconstruction Results	90
CHAPTER 6 CONCLUSION	94
6.1 Summary	94
6.1.1 Autofocus by sharpness optimization	94
6.1.2 A multichannel approach to SAR autofocus	95
6.1.3 Multichannel estimation of coil sensitivities	96
6.2 Future Directions	96
6.2.1 Extensions to SAR autofocus	96
6.2.2 Extensions to optical coherence tomography	99

REFERENCES	100
AUTHOR'S BIOGRAPHY	105

LIST OF TABLES

Table		Page
5.1	SNR (dB) of the image reconstruction using the proposed technique versus acceleration factor and autocalibration data size. The SNR, using SOS estimates, is shown in parentheses for comparison.	93

LIST OF FIGURES

Figure	Page
2.1	Geometry of spotlight-mode SAR imaging scenario. 7
2.2	Polar annulus of acquired Fourier data. 8
2.3	Interpolation of polar-formatted SAR data to a Cartesian grid. 10
2.4	Restorations of an actual SAR image, where a white Fourier phase error has been applied, using PGA and the entropy-minimization technique: (a) defocused image (entropy = 11.38), (b) PGA restoration (entropy = 9.770), and (c) minimum-entropy restoration (entropy = 8.596). 12
2.5	Graphical illustration of an eight-coil PMRI array. 15
2.6	Images formed using a single receiver coil: (a) illustration showing activated coil (in black), (b) (unaliased) sensitivity-weighted image, (c) aliased image, where an acceleration factor of 2 is used in the k_y dimension, and (d) reconstructed image function using data from all coils. 16
2.7	Figure illustrating the acquired data in k -space from a particular coil. The central rectangular region shows the autocalibration data, collected at the Nyquist rate, that can be used to estimate the coil sensitivity functions (or used in other autocalibrating PMRI reconstruction methods). The horizontal lines show acquired lines in k -space that are undersampled in the k_y dimension (relative to the Nyquist rate). 17
2.8	Graphical illustration of GRAPPA. The solid and dashed lines indicate the available and missing k -space lines, respectively. In this example, $A = 3$, and it is desired to reconstruct the circled line of the third coil $\hat{\rho}_3(k_x, k_m + \Delta_m)$ 20
3.1	An approximate expression for the objective function using the intensity-squared cost: (a) perfectly focused range bin model, and (b) plots of $f_g(\phi \mathbf{e}_{18})$ versus $\phi \in [-\pi, \pi)$ for the model in (a), where the solid plot shows the exact numerically evaluated metric, and the dashed plot uses the approximate expression in (3.19). 29

3.2	Demonstration of the reinforcement of metric minima as an increased number of columns are included in the stochastic model. (a) One column of the stochastic model ($P = 9, M = 64$). (b)-(f): Normalized plots of the objective function along each coordinate direction $f_g(\phi \mathbf{e}_k), k = 0, 1, \dots, M - 1$ (shown superimposed), where (b) $N = 1$, (c) $N = 3$, (d) $N = 10$, (e) $N = 64$, and (f) $N = 256$	34
3.3	Log-scale plot showing the squared ℓ_2 -norm of the phase shifts (i.e., deviations from $\phi = 0$) as a function of the number of columns N (plot with cross markers). The behavior as a function of N is found to be proportional to $\frac{1}{N}$ (displayed in the dashed curve).	35
3.4	Experiment with an actual SAR image. (a) Intensity of perfectly focused SAR image (displayed in dB), (b) plots of the objective function ($k = 0, 1, \dots, 600$) for the image in (a), (c) plots of the objective function for column 491 ($k = 3, 11, 19, \dots, 595$), (d) defocused image where a small white phase error has been applied to (a), (e) applied phase error $\phi_e[k]$ (star markers) and phase estimate from simultaneous 1-D searches (circle markers) ($k = 3, 11, 19, \dots, 595$), and (f) image restored by applying the phase estimate in (e).	38
3.5	Experiment with an actual SAR image. (a) Intensity of perfectly focused SAR image (displayed in dB), (b) plots of the objective function ($k = 95, 191, 287, \dots, 2015$) for the image in (a), (c) plots of the objective function for column 680 ($k = 95, 191, 287, \dots, 2015$), (d) defocused image, (e) applied phase error $\phi_e[k]$ (star markers), and phase estimate obtained after one iteration of simultaneous coordinate descent (diamond markers) and three iterations (circle markers) for $k = 31, 63, \dots, 2015$, and (f) image restored after three iterations of simultaneous coordinate descent.	40
4.1	Diagram illustrating the multichannel nature of the autofocus problem. Here, \mathbf{b} is the blurring kernel, $\{\mathbf{g}^{[n]}\}$ are the perfectly focused image columns, and $\{\tilde{\mathbf{g}}^{[n]}\}$ are the defocused columns.	43
4.2	Illustration of the spatially limited image support assumption in the special case where there are low-return rows in the perfectly focused image.	53
4.3	The antenna pattern shown superimposed on the scene reflectivity function for a single range (y) coordinate. The finite beamwidth of the antenna causes the terrain to be illuminated only within a spatially limited window; the return outside the window is near zero.	61
4.4	Actual 2335×2027 pixel SAR image: (a) perfectly focused image, where the simulated sinc-squared antenna footprint in (b) has been applied to each column, (c) defocused image produced by applying a white phase error function, and (d) MCA restoration ($\text{SNR}_{out} = 10.52$ dB).	64

4.5	Experiments evaluating the robustness of MCA as a function of the attenuation in the low-return region: (a) window function applied to each column of the SAR image, where the gain at the edges of the window (corresponding to the low-return region) is varied with each experiment (a gain of 0.1 is shown); (b) plot of the quality metric SNR_{out} for the MCA restoration (measured with respect to the perfectly focused image) versus the window gain in the low-return region; (c) simulated perfectly focused 309×226 pixel image, where the window in (a) has been applied; (d) defocused image produced by applying a white phase error function; and (e) MCA restoration ($\text{SNR}_{out} = 9.583$ dB).	65
4.6	Comparison of MCA with existing autofocus approaches: (a) simulated 341×341 pixel perfectly focused image, where the window function in Figure 4.5(b) has been applied; (b) noisy defocused image produced by applying a quadratic phase error, where the input SNR is 40 dB (measured in the range-compressed domain); (c) MCA restoration ($\text{SNR}_{out} = 25.25$ dB); (d) PGA restoration ($\text{SNR}_{out} = 9.64$ dB); (e) entropy-based restoration ($\text{SNR}_{out} = 3.60$ dB); and (f) restoration using the intensity-squared sharpness metric ($\text{SNR}_{out} = 3.41$ dB).	67
4.7	Plots of the restoration quality metric SNR_{out} versus the input SNR for MCA, PGA, entropy-minimization autofocus, and intensity-squared minimization autofocus. In this experiment, we performed a Monte Carlo simulation where MCA was applied to noisy versions of the defocused image in Figure 4.6(b); ten different white complex-Gaussian noise realizations were used for each experiment at a particular input SNR.	69
4.8	Experiment using entropy optimization as a regularization procedure to improve the MCA restoration when the input SNR is low. The optimization is performed over a space of 15 basis functions determined by the smallest singular values of the MCA matrix. (a) Perfectly focused image where a sinc-squared window is applied, (b) noisy defocused image with range-compressed domain SNR of 19 dB produced using a quadratic phase error, (c) MCA restoration, and (d) regularized MCA restoration using the entropy metric.	70
5.1	Diagram illustrating the multichannel nature of the coil sensitivity problem. Here, $\rho[n, m]$ is the image function, $\{s_i[n, m]\}$ are the coil sensitivity functions, and $\{\rho_i[n, m]\}$ are the sensitivity-encoded images, where $\rho_i[n, m] = \rho[n, m]s_i[n, m]$ (i.e., the filtering operation is described by multiplication in the spatial domain).	73
5.2	Illustration of the convolution of polynomial basis coefficients associated with two coils for the case where $R = 2$	80

5.3	Example of a particular polynomial basis function: (a) basis function $\varphi_{(2,1)}[n, m] = n^2m$, (b) binary mask that is one within the object support and zero otherwise, (c) masked version of the basis function in (a), and (d) basis function after performing orthonormalization.	85
5.4	Illustration of the importance of the masking-and-orthonormalization sequence in constructing the basis functions: (a) singular values of the matrix of vectorized basis functions for the case where (i) orthonormalization has been performed prior to masking (circular markers) and (ii) orthonormalization is applied <i>after</i> masking (star markers), and (b) singular values of the matrix \mathbf{A} using the basis functions for the previous case in (a) (circular markers) and the later case (star markers). In the later case, the conditioning of \mathbf{A} is improved; i.e., there are fewer singular values close to zero.	86
5.5	Plots of the relative error (defined in (5.41)) between the actual sensitivity functions and their R -th order approximation in (5.40) as a function of R for each coil.	88
5.6	Plots of the restoration quality metric SNR_{out} in (5.44) as a function of input signal-to-noise ratio (defined in (5.43)). For simplicity, we assume that $\rho[n, m] = 1$ and that the actual sensitivity functions are described exactly by the selected basis. The three plots show cases where $R = 3$ (star markers), $R = 4$ (circular markers), and $R = 5$ (square markers). These plots reveal that the solution becomes more sensitive to noise as the polynomial order is increased.	89
5.7	Experiment using <i>simulated</i> sensitivity functions for an eight-channel head array coil, where the full-resolution image function is $N = 128$ by $M = 128$ pixels. An acceleration factor of $A = 2$ is used along the k_y -dimension, and a $N' = 64$ by $M' = 64$ block of autocalibration data is collected from each coil. In addition, additive white complex Gaussian noise with variance $NM(0.01a)^2$ (where a is the peak pixel magnitude) has been applied to the k -space data from each coil. (a) Applied sensitivity function for coil 4, (b) estimated sensitivity function using the proposed technique, (c) SOS sensitivity estimate, (d) the root sum of the squares of all the sensitivity functions (note that this is not constant over the image), (e) original image, (f) reconstructed image using SENSE with sensitivity estimates from our method (SNR = 26.30 dB), (g) SENSE reconstruction with the SOS sensitivity estimates (SNR = 17.10 dB), and (h) GRAPPA reconstruction (SNR = 17.06 dB).	91

5.8 Experiment using *actual* data from an eight-channel head array coil, where $A = 2$, $N = M = 256$, and $N' = M' = 64$: (a) SENSE image reconstruction using sensitivity estimates from the proposed technique, (b) SENSE reconstruction using SOS sensitivity estimates, (c) GRAPPA reconstruction, and (d) image reconstruction formed by applying SOS to the full k -space data where no subsampling is assumed ($N' = M' = 256$ and $A = 1$). Note the aliasing artifact at the center of the SOS SENSE reconstruction in (b) (indicated by the arrow), which is due to wrong sensitivity estimates towards the image center; in the proposed reconstruction (a), such artifacts are reduced, and the contrast is improved towards the center of the image in comparison with (b)-(d). 92

CHAPTER 1

INTRODUCTION

1.1 Motivation

The advent of next-generation high-resolution imaging systems has posed unique challenges for system design and image formation algorithms. Imaging systems manipulate raw signal measurements resulting from physical processes to form useful imagery. Such systems utilize mathematical models for the imaging process, where the signal measurements are assumed to be made in the absence of error. When the acquired signals are not accurately described by the model, or when the measurements are contaminated with noise, the produced imagery is subject to distortions. One approach for remedying these undesired effects is to put more emphasis on the system design, which often results in expensive hardware modifications and calibration. The focus of this dissertation lies in the alternative approach of applying signal processing concepts to the image formation to form useful imagery from imperfect signal measurements. The signal processing approach reduces expense and system complexity, and moves the effort of calibration away from the physical realm and into the algorithmic realm.

Synthetic aperture radar (SAR) exploits the phases of acquired signal data to form high-resolution imagery. In practice, the signal phases are noisy due to imprecise knowledge of the motion of the sensor, or due to signal propagation through a medium having a spatially varying propagation velocity. The result is that the Fourier transform of the scene is corrupted by multiplicative phase errors, so that the produced imagery is improperly focused. To compensate for the effects of phase errors, researchers have developed

a number of approaches to data-driven *autofocus*, where the unknown phase errors are estimated to correct the defocused image. Currently employed SAR autofocus algorithms are well-motivated, but they are also heuristic. They tend to perform poorly when the phase errors are large and highly random or when the scene contains little geometric structure.

In parallel magnetic resonance imaging (PMRI), multiple acquisitions of *subsampled* k -space (Fourier domain) data are obtained simultaneously using different receiver coils. The benefit of such an approach is to reduce the total acquisition time (i.e., the amount of time that a patient needs to stay in the MRI scanner). The image function can be recovered from the subsampled data given knowledge of the *sensitivity functions* associated with each coil. Estimates of the sensitivity functions can be obtained either through initial calibration scans, or through assumptions based on the physics of the imaging scenario. However, there are cases where these approaches do not produce sufficiently accurate estimates, resulting in distortions in the reconstructed image.

A common thread in both the SAR autofocus problem and the coil sensitivity estimation problem in PMRI is their multichannel nature. In SAR, the phase errors are often modeled as a 1-D function of the synthetic aperture, i.e., each row of the 2-D Fourier transform data has an undesired phase shift applied. The corresponding effect in the spatial domain is that each column of the image is blurred by the same kernel resulting from the phase errors. Likewise, in parallel MRI, multiple data acquisitions for the same object are obtained with different sensitivity encodings. This multichannel characterization is useful because it provides a special structure to the restoration problems that can be exploited to estimate the distortion-free image.

The goal of this research is to develop a modern image restoration methodology, where assumptions in the problem statement are systematically utilized to produce improved restoration procedures. The research is conducted within the frameworks of the forementioned restoration problems; this is due to their present-day relevance, and also due to common assumptions in both problems that provide an opportunity to export restoration technologies from one imaging modality to another.

1.2 Dissertation Contribution

In the first and second components of this dissertation, the SAR autofocus problem is considered. The research is focused on two aspects of SAR autofocus that are critical to the success of the restoration algorithms: (i) the image model and (ii) the multichannel nature of the SAR data. These two aspects of the problem statement suggest the following restoration approaches: (i) metric-based strategies that optimize image sharpness metrics, and (ii) subspace techniques that exploit the redundancy of the blurring operation on each column of the image.

SAR autofocus techniques that optimize sharpness metrics can produce excellent restorations in comparison with conventional autofocus approaches. To help formalize the understanding of metric-based SAR autofocus methods, and to gain more insight into their performance, a theoretical analysis of these techniques using simple image models is presented in the first component of the dissertation. Specifically, the intensity-squared metric and a dominant point-targets image model are considered, and expressions for the resulting objective function are derived. The conditions under which the perfectly focused image models correspond to stationary points of the objective function are examined. A key finding is that the sparsity assumption of the SAR image alone is not enough to guarantee a stationary point; the analytical results show how metric-based methods rely on the multichannel defocusing model of SAR autofocus to enforce this stationary point property for multiple image columns. Furthermore, the analysis shows that near the perfectly focused image, the objective function can be well approximated by a sum of 1-D functions of each phase error component. This allows fast performance through solving a sequence of 1-D optimization problems for each phase component simultaneously.

The analysis of metric-based techniques, together with the failure of these approaches in certain cases (e.g., cases where the suitability of sharpness metrics is not a good prior assumption for the underlying SAR scene), suggests that a means for exploiting the multichannel condition *explicitly* is needed. In the second component of the dissertation, the multichannel condition of the SAR autofocus problem is explicitly characterized

by constructing a low-dimensional subspace where the perfectly focused image resides, expressed in terms of a known basis formed from the given defocused image. A unique solution for the perfectly focused image is then directly determined through a linear algebraic formulation by invoking an additional image support condition. This approach is termed the MultiChannel Autofocus (MCA) algorithm. The MCA approach is found to be computationally efficient and robust, and does not require prior assumptions about the SAR scene used in existing methods. In addition, the vector space formulation of MCA allows sharpness metric optimization to be easily incorporated within the restoration framework as a regularization term, where the optimization is performed over a reduced set of parameters relative to the number of unknown phase error components.

In the third component of the dissertation, the problem of estimating receiver coil sensitivity functions in PMRI is considered. By exploiting the multichannel nature of the problem, where multiple acquisitions of the same image function are obtained with different sensitivity encodings, a subspace-based framework for directly solving for the sensitivity functions is obtained. The proposed approach does not rely on the sum-of-squares assumption used in existing estimation schemes; this assumption tends to be violated towards the center of the image, thus leading to errors in the sensitivity estimates. The new approach eliminates this problem, producing superior sensitivity estimates in comparison to the sum-of-squares technique. In addition, the proposed restoration procedure is noniterative, computationally efficient, and applicable both to cases where pilot scans are available or where autocalibration data are collected with each scan.

The organization of this dissertation is as follows. Chapter 2 presents an overview of both the SAR autofocus problem and the problem of estimating coil sensitivities in PMRI; a brief summary of existing approaches to each problem is provided. In Chapter 3, a theoretical study of autofocus techniques that optimize image sharpness metrics is presented. Chapter 4 covers the MultiChannel Autofocus algorithm, presenting theory and experimental results. In Chapter 5, the subspace-based approach for estimating coil

sensitivities in PMRI is proposed and studied using simulated and actual PMRI data. Chapter 6 summarizes this dissertation and presents a discussion of future applications.

CHAPTER 2

BACKGROUND

2.1 The SAR Autofocus Problem

2.1.1 Problem statement

In this section, we establish the notation to be used in this paper and present a statement of the problem. In our development, we will focus on *spotlight-mode SAR* because of the high-resolution imagery it offers, and because the algorithms used in this modality can also be applied to strip-mapping SAR [1–4]. The geometry of this imaging scenario is shown in Figure 2.1. Here, a patch of terrain is illuminated with multiple radar pulses over a range of look angles θ_m : $\theta_{min} \leq \theta_m \leq \theta_{max}$, $m = 0, 1, \dots, M - 1$. The goal is to create an image of the complex-valued reflectivity function $q(x, y)$, where typically only the magnitude $|q(x, y)|$ is used in the image display. The demodulated radar returns from each pulse are effectively 1-D Fourier transforms of the projection function of the reflectivity at the angle θ_m ; in other words, the projection function $p_{\theta_m}(r)$ represents line integrals of the reflectivity performed normal to the radar line-of-sight (LOS) at θ_m :

$$p_{\theta_m}(r) = \int_{t=-\infty}^{t=\infty} q(r \cos \theta_m - t \sin \theta_m, r \sin \theta_m + t \cos \theta_m) dt, \quad (2.1)$$

where the r -axis is along the radar LOS and the t -axis is normal to the radar LOS [2]. Through the *projection slice theorem*, the 1-D Fourier transform of $p_{\theta_m}(r)$, $P_{\theta_m}(f_r)$, is a “slice” of the 2-D Fourier transform of $q(x, y)$, $Q(f_x, f_y)$, taken at the angle θ_m :

$$P_{\theta_m}(f_r) = Q(f_r \cos \theta_m, f_r \sin \theta_m). \quad (2.2)$$

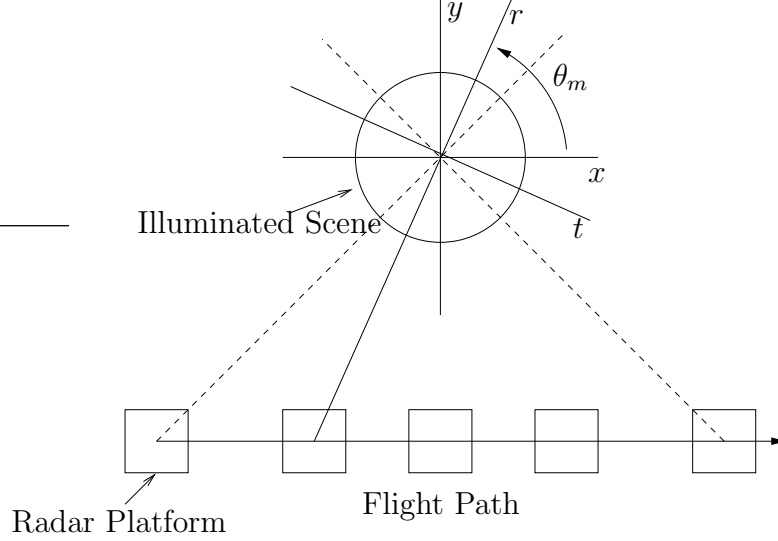


Figure 2.1 Geometry of spotlight-mode SAR imaging scenario.

In practice, the region over which the integral in (2.1) is performed is limited by the support of the *antenna footprint* $w(x, y)$. Therefore, we consider the weighted reflectivity function

$$g_a(x, y) = q(x, y)w(x, y), \quad (2.3)$$

where the support of w is effectively limited to a particular region in space: $(x, y) \in \Omega_a \subset \mathbb{R}^2$. Due to the properties of the radar pulse, only a bandlimited portion of the 2-D Fourier transform of $g_a(x, y)$, $G_a(f_x, f_y)$, is provided by the demodulated radar returns. Specifically, the transmitted radar pulses are described by the linear FM pulse

$$s(t) = \begin{cases} e^{j(2\pi\nu_0 t + \alpha t^2)} & \text{for } t \text{ satisfying } -\frac{\tau}{2} \leq t \leq \frac{\tau}{2}, \\ 0 & \text{otherwise,} \end{cases}$$

where ν_0 is the radar carrier frequency, τ is the duration of the pulse, and 2α is the FM rate [2]. The duration of the pulse τ determines the range of spatial frequencies present, and the carrier frequency ν_0 causes the available spatial-frequency data to be offset from the origin of Fourier space. The demodulated radar returns from each angle θ_m can be

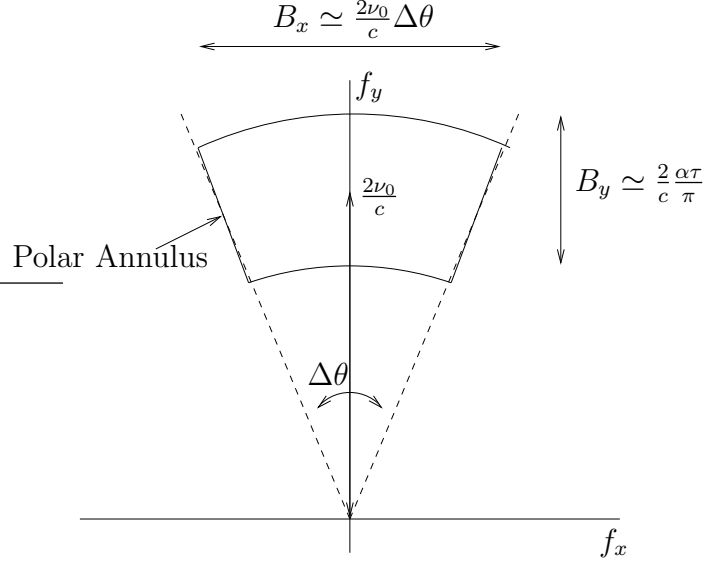


Figure 2.2 Polar annulus of acquired Fourier data.

modeled as

$$\mathcal{G}_{\theta_m}(f_r) = \begin{cases} G_a(f_r \cos \theta_m, f_r \sin \theta_m) & \text{for } f_r \text{ satisfying } \frac{2}{c} \left(\nu_0 - \frac{1}{2} \frac{\alpha\tau}{\pi} \right) \leq f_r \leq \frac{2}{c} \left(\nu_0 + \frac{1}{2} \frac{\alpha\tau}{\pi} \right). \\ 0 & \text{otherwise} \end{cases} \quad (2.4)$$

The Fourier data are observed to lie on a polar annulus, as shown in Figure 2.2, with frequency offset $f_0 = \frac{2\nu_0}{c}$, and bandwidth described by $B_x \approx \frac{2\nu_0}{c} \Delta\theta$, $\Delta\theta = |\theta_{max} - \theta_{min}|$, and $B_y \approx \frac{2}{c} \frac{\alpha\tau}{\pi}$. Here, we utilize the convention that the x -axis corresponds to the direction of the flight path or the trajectory of the radar, which is often denoted as the *cross-range* or *azimuth* dimension, and that the y -axis corresponds to the dimension normal to the flight path, referred to as the *range* dimension. For simplicity of analysis, we assume that the depression angle from the radar to the terrain patch is zero; when the radar platform is elevated as in airborne SAR, the SAR data can be compensated to correct for a nonground plane geometry [2].

The demodulated returns are sampled at the radar receiver, producing the set of discrete data $\{\mathcal{G}_{\theta_m}(f_{r,k})\}$, $m = 0, 1, \dots, M-1$, $k = 0, 1, \dots, K-1$, which represent samples of the 2-D Fourier transform $G_a(f_x, f_y)$ on a polar raster. To efficiently form an SAR image using a 2-D inverse FFT, the polar-formatted SAR data must be interpolated to

a Cartesian grid. We denote the interpolated Fourier transform as

$$\hat{G}_a(f_x, f_y) = \sum_{l=0}^{M-1} \sum_{k=0}^{K-1} \mathcal{G}_{\theta_l}(f_{r,k}) \Psi(f_x - f_{r,k} \cos \theta_l, f_y - f_{r,k} \sin \theta_l), \quad (2.5)$$

where Ψ is an appropriate interpolation kernel. The *SAR imaging data* are samples of the interpolated 2-D Fourier transform \hat{G}_a taken on a Cartesian sampling grid

$$G[k_m, k_n] = \hat{G}_a(k_m \Delta X, k_n \Delta Y), \quad (2.6)$$

where $k_m = 0, 1, \dots, M-1$, and $k_n = 0, 1, \dots, N-1$, are discrete spatial-frequency indices of the cross-range (x) and range (y) dimensions, respectively, and ΔX and ΔY are the sampling intervals in the Fourier domain for the respective dimensions.

To properly demodulate the SAR data returns, the two-way travel time of each radar pulse must be known with a particular degree of accuracy. When these measurements are inaccurate due to signal propagation through a medium with spatially varying propagation velocity, or due to deviations in the assumed radar platform trajectory, the result is an undesired and unknown phase shift on each demodulated radar return [1]. We model the phase corrupted demodulated returns as

$$\tilde{\mathcal{G}}_{\theta_m}(f_r) = \mathcal{G}_{\theta_m}(f_r) e^{j\phi_m}, \quad (2.7)$$

where \mathcal{G}_{θ_m} is the uncorrupted demodulated return in (2.4), and ϕ_m is an unknown phase shift that varies with each look angle θ_m . Assuming the range of look angles is sufficiently small so that the polar formatted slices of the 2-D Fourier transform correspond approximately to Cartesian slices, as shown in Figure 2.3, we can say to a good approximation that each row of the SAR imaging data (i.e., cross-range spatial frequency) is corrupted by a multiplicative phase term of the form $e^{j\phi_m}$. Thus, we can express the corrupt Fourier imaging data \tilde{G} as a function of the perfectly focused imaging data G

$$\tilde{G}[k_m, k_n] = G[k_m, k_n] e^{j\phi_e[k_m]}, \quad (2.8)$$

where $\phi_e[k_m]$ is a 1-D *Fourier phase error function*.

The presence of the Fourier phase error function causes the resulting SAR imagery to be improperly focused. To see this, we examine the *range-compressed* form of the

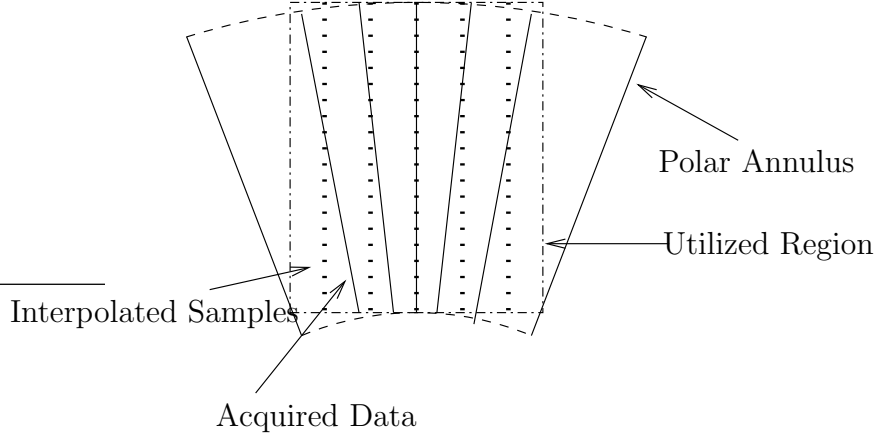


Figure 2.3 Interpolation of polar-formatted SAR data to a Cartesian grid.

imaging data, where a 1-D inverse DFT is applied to each row of the imaging data:

$\tilde{G}[k_m, n] = DFT_{k_n}^{-1}\{\tilde{G}[k_m, k_n]\}$. In range-compressed form, (2.8) becomes

$$\tilde{G}[k_m, n] = G[k_m, n]e^{j\phi_e[k_m]}. \quad (2.9)$$

The SAR image is formed by performing a 1-D inverse DFT on each column of the range-compressed data:

$$\tilde{g}[m, n] = DFT_{k_m}^{-1}\{\tilde{G}[k_m, n]\}, \quad (2.10)$$

where \tilde{g} is defocused because it is formed using the corrupted data \tilde{G} . In the spatial domain, the defocused image is related to the perfectly focused image

$$g[m, n] = DFT_{k_m}^{-1}\{G[k_m, n]\}$$

through the relationship

$$\tilde{g}[m, n] = g[m, n] \otimes_M b[m], \quad (2.11)$$

where \otimes_M denotes M -point circular convolution, and

$$b[m] = DFT_{k_m}^{-1}\left\{e^{j\phi_e[k_m]}\right\}.$$

Here, we see that each column of the perfectly focused image is defocused by a common blurring kernel $b[m]$.

The aim of *SAR autofocus* is to restore the perfectly focused image g given the defocused image \tilde{g} and assumptions about the characteristics of the underlying scene $g_a(x, y)$. Autofocus approaches typically create an estimate of the phase error function $\hat{\phi}[k_m]$, and apply this estimate to $\tilde{G}[k_m, n]$ to form the restored data

$$\hat{G}[k_m, n] = \tilde{G}[k_m, n]e^{-j\hat{\phi}[k_m]}, \quad (2.12)$$

where the restored image is formed as

$$\hat{g}[m, n] = DFT_{k_m}^{-1}\{\hat{G}[k_m, n]\}. \quad (2.13)$$

Many of these methods are iterative, evaluating some measure of image focus in the spatial domain (e.g., image sharpness metrics) and then perturbing the estimate of the Fourier phase error function in a manner that increases the focus metric.

2.1.2 Existing approaches to SAR autofocus

There have been many approaches addressing the SAR autofocus problem. An early class of autofocus methods, generally referred to as *Map Drift*, uses the shift property of the Fourier transform to create a piecewise approximation to the phase error [5–8]. Such an approach relies upon the assumption that the phase error can be modeled by a low-order polynomial, and tends to perform poorly when higher-order or random phase errors are considered [1]. A second class of autofocus techniques is based on inverse filtering, where bright isolated scatterers in the defocused image are used to approximate the blurring kernel response. *Phase Gradient Autofocus* (PGA) employs the basic principles of inverse filtering and augments them with an innovative iterative windowing and averaging process [1, 9–11]. PGA is widely used in practice, and typically produces an accurate approximation of the phase error for a variety of errors.

Exceptional restoration quality has been observed through the use of a third class of autofocus methods that *optimize image sharpness metrics* [12–18]. In these *metric-based* autofocus methods, the compensating phase estimate is selected through an optimization algorithm to maximize a particular sharpness metric evaluated on the defocused

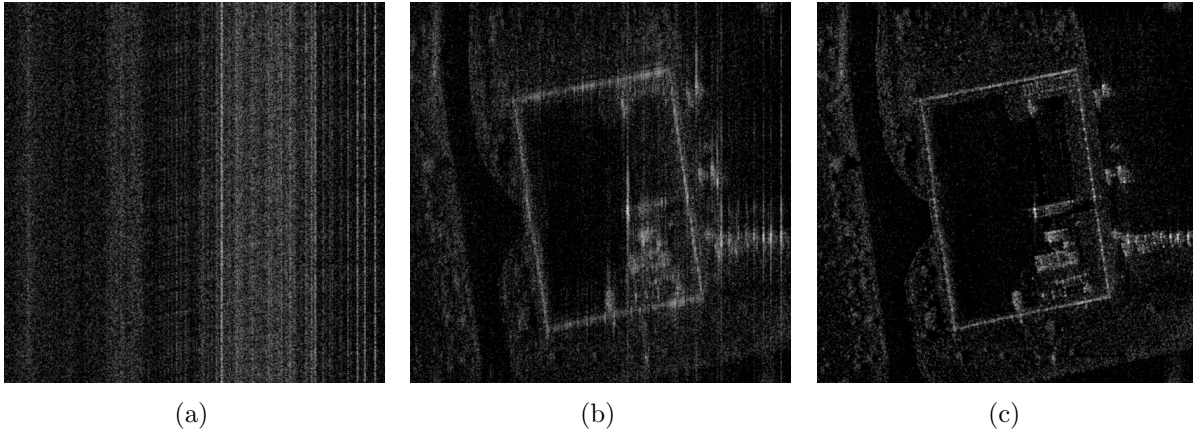


Figure 2.4 Restorations of an actual SAR image, where a white Fourier phase error has been applied, using PGA and the entropy-minimization technique: (a) defocused image (entropy = 11.38), (b) PGA restoration (entropy = 9.770), and (c) minimum-entropy restoration (entropy = 8.596).

image intensity. Examples of the optimization approaches used in these methods include gradient-descent techniques [15], coordinate direction searches [14], and monotonic iterative algorithms [17, 18]. The use of metric-based autofocus algorithms sometimes produces superior restorations in comparison with the conventional PGA method in experiments using both synthetic and actual SAR imagery [16], [19]. The metric-based methods are particularly promising because they have been found to accurately correct most classes of phase errors, sometimes including white phase errors (i.e., independent Fourier phase components uniformly distributed between $-\pi$ and π), which cause the most severe defocusing effects. Such phase errors are of practical importance in high-resolution SAR and ISAR systems that operate at very short wavelengths [20], and in space-borne SAR systems that image through the ionosphere [21]. In comparison to metric-based methods, PGA tends to perform less well on images defocused by rapidly varying or white phase errors, or when the underlying image lacks a sufficient number of bright isolated scatterers [19]. Figure 2.4(a) shows an actual SAR image defocused by a white phase error. Restorations using PGA and the metric-based approach in [18] with the entropy metric (defined in [15]) are shown in Figures 2.4(b) and (c), respectively. The entropy minimization result is found to be superior to PGA.

2.2 Estimation of Coil Sensitivities in PMRI

2.2.1 Problem setup

In magnetic resonance imaging (MRI), an image is formed of the proton density of an object. The proton density provides valuable information about the anatomical structure of tissue, which is rich in hydrogen atoms (where the nucleus consists of a single proton). Protons possess a property known as *angular momentum*, or *spin*, that causes the protons to precess when placed in an external magnetic field. The frequency of precession is proportional to the applied field strength. By Faraday's law, the precessing photons produce a time-varying magnetic field that can induce a measurable voltage in a receiver coil. Such phenomena underly the signal-generating mechanism used in MRI [22].

MRI systems use a spatially varying *magnetic field gradient*, which causes the protons within an object to precess at frequencies proportional to their location in space. The acquired MRI signal $M(t)$ can be modeled as a superposition of harmonic signals

$$M(t) = \int s(x, y)\rho(x, y)e^{-j2\pi\omega_x(x)t}dxdy, \quad (2.14)$$

where $\rho(x, y)$ is the *spin density* (the image function in MRI), $s(x, y)$ is the *coil sensitivity function*, which characterizes the detection sensitivity of the receiver coil [22], and $\omega_x(x)$ is the induced frequency due to the magnetic field gradient applied along the x -dimension. In many cases, the receiver coil is assumed to have a homogenous reception field over the object so that $s(x, y) \approx 1$ [22]. In addition, the gradient can be modeled as having a linear spatial variation: $\omega_x(x) = G_x x$, where G_x is the gradient strength. From these two assumptions, we observe the Fourier transform relationship

$$M(t) = \hat{\rho}(G_x t, 0) = \int \rho(x, y)e^{-j2\pi G_x x t}dxdy, \quad (2.15)$$

where $\hat{\rho}(k_x, k_y)$ is the 2-D Fourier transform of $\rho(x, y)$. Here, $M(t)$ provides a “slice” of $\hat{\rho}$ along the $k_y = 0$ axis, where $k_x(t) = G_x t$. We refer to this slice as a *line* in k -space (i.e., Fourier space); at each time t , a different value of the Fourier transform is obtained along the line. This process is referred to as *frequency encoding*.

In (2.15), only information along the x -dimension can be resolved; $M(t)$ gives the projection of $\rho(x, y)$ taken along the y -axis. To resolve detail along the y -dimension, a process of *phase encoding* is performed, which effectively modulates $\rho(x, y)$ to collect other lines in k -space. To accomplish this, the linear field gradient $\omega_y(y) = G_y y$ is applied along the y -dimension. This gradient is activated for a fixed time T prior to performing frequency encoding. After this fixed time, the MRI signal is collected

$$M'(t) = \hat{\rho}(G_x t, G_y T) = \int \rho(x, y) e^{-j2\pi G_y y T} e^{-j2\pi G_x x t} dx dy, \quad (2.16)$$

which provides a slice of $\hat{\rho}$ along the $k_y = G_y T$ axis. Note that $e^{-j2\pi G_y y T}$ applies a phase modulation to $\rho(x, y)$ that varies linearly with y , but that is independent of t during the readout interval.

The process of phase encoding and frequency encoding underlies the popular echo-planar imaging (EPI) scheme, where data are acquired on a Cartesian trajectory in k -space. By using more sophisticated field gradients, other k -space trajectories can be achieved (e.g., a spiral trajectory) that offer different hardware-implementation/algorithmic-complexity tradeoffs [22]. The following generalized expression can be used to model the acquired data for an arbitrary k -space trajectory $\mathbf{k}(t) = (k_x(t), k_y(t))$:

$$\hat{\rho}(\mathbf{k}(t)) = \int s(\mathbf{r}) \rho(\mathbf{r}) e^{-j2\pi \mathbf{k}(t) \cdot \mathbf{r}} d\mathbf{r}, \quad (2.17)$$

where $\mathbf{r} = (x, y)$ are spatial-domain coordinates.

The acquisition time in MRI is determined by the number of phase encoding lines and the amount of data collected along each line (i.e., the total bandwidth recorded in the k_x dimension). Recently, there has been an interest in techniques that reduce the total acquisition time by using multiple receiver coils [23–25]. This approach to fast imaging is referred to as *parallel magnetic resonance imaging* (PMRI). It offers the benefit of reducing the duration of time that it takes to scan a patient. Figure 2.5 presents a graphical illustration of the setup in a PMRI array. Here, there is a common object that is imaged using multiple coils; in this example, an eight-coil head array used for brain imaging is shown. The coils have different orientations in space relative to the imaged

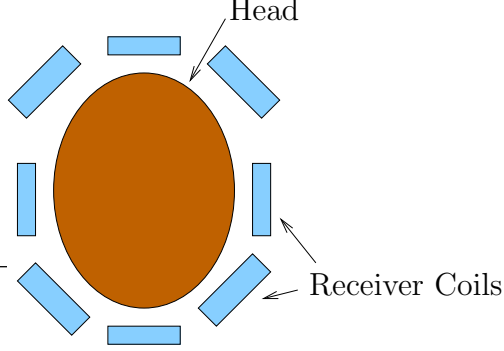


Figure 2.5 Graphical illustration of an eight-coil PMRI array.

object. The MR signals from the object are received with an intensity proportional to their displacement from the coils [25]. Thus, information about the object is spatially encoded by the sensitivity functions associated with each receiver coil. The diversity of the spatial encodings can be used to decrease the k -space sampling requirements, analogous to generalized sampling theory [26]. By reducing the sampling requirements, the total acquisition time is decreased.

We consider a PMRI setup where P different receiver coils are used. The following model describes the data collected from the i -th receiver coil, $i = 1, 2, \dots, P$:

$$\hat{\rho}_i(\mathbf{k}_l) = \int s_i(\mathbf{r})\rho(\mathbf{r})e^{-j2\pi\mathbf{k}_l \cdot \mathbf{r}} d\mathbf{r}, \quad (2.18)$$

where $\hat{\rho}_i(\mathbf{k}_l)$ and $s_i(\mathbf{r})$ are the k -space data and sensitivity functions for the i -th coil, respectively, and $\mathbf{k}_l = (k_x[l], k_y[l])$ ($1 \leq l \leq L$) are samples in k -space. Note that (2.18) is the Fourier transform of the sensitivity-encoded images

$$\rho_i(\mathbf{r}) \stackrel{\text{def}}{=} s_i(\mathbf{r})\rho(\mathbf{r}). \quad (2.19)$$

The goal is to recover $\rho(\mathbf{r})$ from $\hat{\rho}_i(\mathbf{k}_l)$, where the k -space data are *undersampled* with respect to the Nyquist condition. The Nyquist condition in this sense is based on recovering the object at full field-of-view (FOV) without aliasing. When the k -space data are undersampled, the image is aliased in the spatial domain.

Figure 2.6 presents an example of the images formed using a single receiver coil. Figure 2.6(a) depicts a single activated coil (shown in black) at the top left corner of

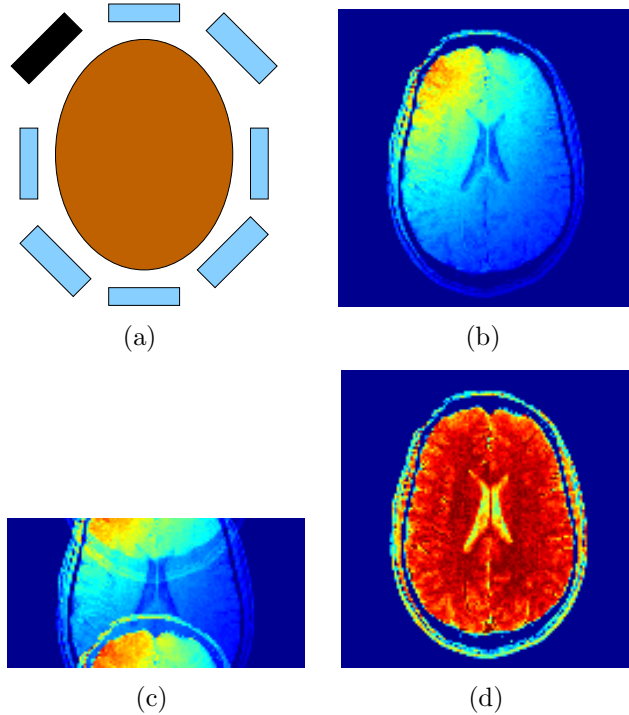


Figure 2.6 Images formed using a single receiver coil: (a) illustration showing activated coil (in black), (b) (unaliased) sensitivity-weighted image, (c) aliased image, where an acceleration factor of 2 is used in the k_y dimension, and (d) reconstructed image function using data from all coils.

the object. The unaliased sensitivity-encoded image from this coil is displayed in Figure 2.6(b). Figure 2.6(c) shows the aliased sensitivity-encoded image that is obtained when the k -space data are subsampled by an *acceleration factor* of two in the k_y dimension; in other words, only half of the phase encoding lines are collected. Figure 2.6(d) shows the reconstructed image function at full FOV, using data from all the receiver coils.

2.2.2 Existing approaches to PMRI reconstruction

Given knowledge of the sensitivity functions associated with each receiver coil, the image function can be recovered from the subsampled k -space data [25]. In general, the coil sensitivity functions are not known; they must be estimated from either initial reference measurements or from *autocalibration data* collected with each scan. In many applications, it is feasible to acquire a small amount of autocalibration data at the center

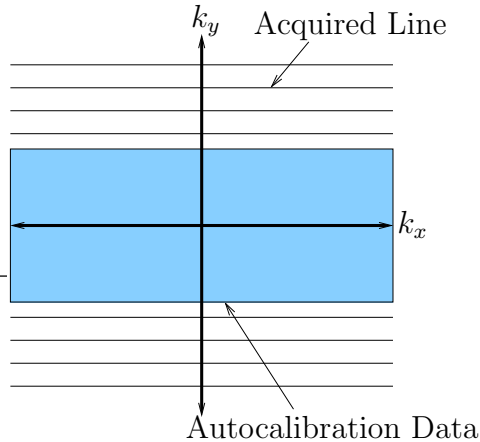


Figure 2.7 Figure illustrating the acquired data in k -space from a particular coil. The central rectangular region shows the autocalibration data, collected at the Nyquist rate, that can be used to estimate the coil sensitivity functions (or used in other autocalibrating PMRI reconstruction methods). The horizontal lines show acquired lines in k -space that are undersampled in the k_y dimension (relative to the Nyquist rate).

of k -space sampled at the Nyquist rate. This data can be used to form low-resolution unaliased images for each coil to estimate the sensitivity functions. The autocalibration data can also be used to *indirectly* estimate the sensitivity functions, with the goal of directly recovering the missing lines in k -space [23,24]. Figure 2.7 shows an illustration of the acquired data in k -space from a particular coil. The autocalibration data are shown in the shaded rectangular region, while the horizontal lines depict the phase encoded lines collected at a reduced density in the k_y dimension (relative to the Nyquist rate).

One approach to coil sensitivity estimation is to perform the estimation in image space; this is the approach taken in SENSE [25]. Aided by the sensitivity estimates, SENSE uses a linear algebraic formulation to recover the unaliased image at full FOV from the sensitivity-encoded aliased images. Another approach is to perform the sensitivity estimation in k -space, which is the approach used in SMASH [23] and GRAPPA [24]. AUTO-SMASH assumes that the sensitivity functions sum to a constant value over the object FOV; armed with this assumption, AUTO-SMASH estimates a single composite image at full FOV [23]. GRAPPA uses linear prediction to solve for the missing lines in k -space of *every* coil, producing full-FOV sensitivity-encoded images for each coil. An additional approach is the PILS technique, where the sensitivity functions are assumed to

be highly localized; in this technique, a common description for the sensitivity functions of each coil is assumed, and the goal is to estimate the positions of the coils [24, 27].

Both the image-based and Fourier-based approaches to sensitivity estimation rely on *sum-of-squares* (SOS) assumptions, where it is assumed that $\rho(\mathbf{r})$ is real-valued and the root-sum of the squared sensitivity functions equals a constant β , so that

$$\sqrt{\sum_i |\rho_i(\mathbf{r})|^2} = \rho(\mathbf{r}) \sqrt{\sum_i |s_i(\mathbf{r})|^2} \approx \beta \rho(\mathbf{r}). \quad (2.20)$$

For example, GRAPPA reconstructs $\rho_i(\mathbf{r})$, $i = 1, 2, \dots, P$, at full FOV, and then uses (2.20) to form an estimate of $\rho(\mathbf{r})$. In SENSE, the SOS assumption is used to obtain estimates of the sensitivity functions as follows:

$$\hat{s}_i(\mathbf{r}) = \frac{\rho_i(\mathbf{r})}{\sqrt{\sum_i |\rho_i(\mathbf{r})|^2}} \approx \beta^{-1} s_i(\mathbf{r}),$$

where $\rho_i(\mathbf{r})$ is obtained either through an initial pilot scan or from the autocalibration data. In brain imaging (i.e., circular coil geometry), the sensitivity functions tend to have small magnitudes towards the center of the image, making the constant sum assumption (and the corresponding SOS estimates) less accurate in this region. As a result, the use of the SOS estimates can produce aliasing artifacts at the center of the reconstructed image.

In Chapter 5, we propose a new technique for estimating the sensitivity functions that does not rely on the SOS assumption. Aided by these sensitivity estimates, SENSE is used to reconstruct the image function. In the next subsection, we provide a brief description of the SENSE technique.

2.2.3 PMRI reconstruction using SENSE

Let $\hat{\rho}_i^{(A)}[k_n, k_m]$ denote the k -space data from the i -th coil obtained using an acceleration factor of A :

$$\hat{\rho}_i^{(A)}[k_n, k_m] \stackrel{\text{def}}{=} \hat{\rho}_i(\Delta_n k_n, \Delta_m A k_m), \quad (2.21)$$

where $\hat{\rho}_i$ are the k -space data in (2.18), Δ_n and Δ_m are the Nyquist sampling intervals required to reconstruct the object at full FOV in the k_x and k_y dimensions, respectively,

$k_n = -N/2, -N/2 + 1, \dots, N/2 - 1$, and $k_m = -M/(2A), -M/(2A) + 1, \dots, M/(2A) - 1$. The data in (2.21) are subsampled by a factor of A , producing images aliased by a factor of A :

$$\begin{aligned}\rho_i^{(A)}[n, m'] &= DFT_{k_n, k_m}^{-1} \{ \hat{\rho}_i^{(A)}[k_n, k_m] \} \\ &= \sum_{l=0}^{A-1} \rho_i^{(1)}[n, m' + lA],\end{aligned}\quad (2.22)$$

where $n = 0, 1, \dots, N - 1$, $m' = 0, 1, \dots, M/A - 1$, and $\rho_i^{(1)}$ is the image formed using full k -space encoding (i.e., $A = 1$) [25], which from (2.19) can be modeled as

$$\rho_i^{(1)}[n, m] = s_i[n, m]\rho[n, m],\quad (2.23)$$

where $m = 0, 1, \dots, M - 1$. Using (2.23) in (2.22), we obtain

$$\rho_i^{(A)}[n, m'] = \sum_{l=0}^{A-1} s_i[n, m' + lA]\rho[n, m' + lA].\quad (2.24)$$

Given the sensitivity functions $s_i[n, m]$, (2.24) provides $(M/A)N$ known linear equations for each coil in terms of the MN unknown pixel values in $p[n, m]$. Using the images from all the coils, we have $(M/A)NP$ independent equations and MN unknowns, which allows $\rho[n, m]$ to be uniquely determined when $A \leq P$.

2.2.4 PMRI reconstruction using GRAPPA

In contrast to SENSE, GRAPPA does not require explicit estimates of the sensitivity functions to recover the image [24, 25]. Instead, GRAPPA reconstructs the fully encoded k -space data for each coil using the acquired subsampled data and a small number of autocalibration lines [24]. This provides unaliased spatially encoded images for each coil that can be combined using SOS to form a single composite image.

The assumption in GRAPPA is that each of the missing k -space lines can be expressed as a linear combination of the available lines from all the coils. This can be modeled as follows [24]:

$$\hat{\rho}_j(k_x, k_m + m\Delta_m) = \sum_{l=1}^P \sum_{b=0}^{N_b-1} n[j, b, l, m] \hat{\rho}_l(k_x, k_m + bA\Delta_m),\quad (2.25)$$

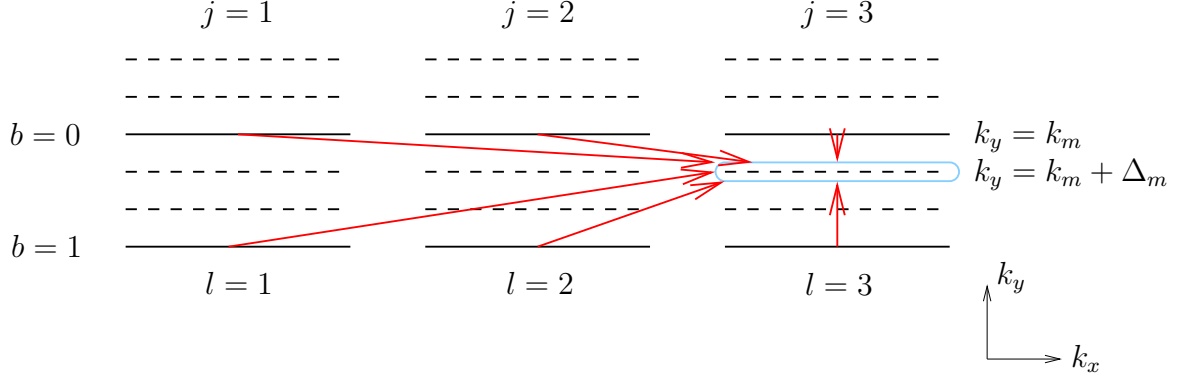


Figure 2.8 Graphical illustration of GRAPPA. The solid and dashed lines indicate the available and missing k -space lines, respectively. In this example, $A = 3$, and it is desired to reconstruct the circled line of the third coil $\hat{\rho}_3(k_x, k_m + \Delta_m)$.

where $\hat{\rho}_j(k_x, k_m + m\Delta_m)$ is the line to be reconstructed, $\hat{\rho}_l(k_x, k_m + bA\Delta_m)$ are the available lines, and $n[j, b, l, m]$ are a set of coefficients relating the available data to the missing data. Figure 2.8 illustrates the process of reconstructing one line in GRAPPA, where $A = 3$. Here, j denotes the coil of the reconstructed line, b is the index of the available lines, l is the coil index for the available lines, and m is an index of the missing line to be reconstructed ($m = 1$ in the figure). Only phase-encoding lines within a local neighborhood of the reconstructed line are used in the linear combination (2.25); N_b denotes the number of neighbors used.

To determine the coefficients in (2.25), the available k -space lines are fit to the autocalibration data. Given the coefficients, the unknown lines in k -space can be directly reconstructed using (2.25).

CHAPTER 3

SAR IMAGE AUTOFOCUS BY SHARPNESS OPTIMIZATION: A THEORETICAL STUDY

3.1 Introduction

Much of the current understanding of metric-based SAR autofocus techniques is based on intuition and results from processing data sets. Thus, it is of interest to obtain a clearer understanding of the performance of these autofocus methods. Such an understanding might enable the powerful restoration ability of these methods to achieve more widespread use. Sharpness metrics were first explored in 1974 by Muller and Buffington for the real-time correction of phase distortions in telescopic imaging systems [29]. Some recent work was done by Fienup et al. in justifying the use of particular metrics for SAR given prior assumptions on the underlying image model [15]. The goal of our work is to gain further insight into metric-based methods for SAR autofocus through studying a simple dominant point-targets image model. Such a model has been used to motivate existing autofocus approaches [1, 10, 14, 15]. Considering the intensity-squared metric, we derive expressions for the objective function as a function of the parameters of the proposed models and also the unknown phase errors. Our expressions, which describe the variation of the metric along the phase-error coordinate directions, are used to determine the conditions under which the perfectly focused SAR image models correspond to *stationary points* of the objective function (i.e., points of zero gradient) [30–32]; these are points where the optimization algorithms used in metric-based autofocus terminate.

This chapter includes research conducted jointly with David C. Munson Jr. and Minh N. Do [28].

Because the phase error is a one-dimensional function of the cross-range frequency coordinate, each range bin (i.e., column of the image) is defocused by the same blurring kernel; we denote this as the *multichannel defocusing model* of SAR autofocus [33, 34]. It has been observed that autofocus approaches generally require multiple columns of the defocused image to produce an accurate estimate of the phase error function; this is true of metric-based methods as well [14]. Thus, it is not the sharpness metric or image model alone that allows the image to be properly restored, but also the redundancy of the defocusing operation on each image column. Our key contribution is that we conclusively demonstrate how the assumption of the multichannel defocusing model is exploited in metric-based SAR autofocus methods. Our analysis shows that one-dimensional point-target models, such as a single column of the perfectly focused image, generally do not correspond to stationary points of the objective function. However, accurate estimation of the phase error is possible when the objective function is evaluated for multiple image columns; the (objective function) minima from multiple columns reinforce each other, or average, to form a stationary point at the perfectly focused phase estimate. It is through this averaging mechanism that metric-based methods implicitly use the multichannel assumption and correctly estimate the phase error.

We also demonstrate that near the perfectly focused image, the objective function can be well approximated by a sum of 1-D functions of each phase error component. Thus, we show that, locally, the multivariate objective function is a separable function of the phase perturbations. This finding allows fast optimization using a simultaneous coordinate descent approach, where a sequence of 1-D optimization problems is solved for each phase component simultaneously, and underlies the success of efficient monotonic algorithms for metric-based SAR autofocus [18].

The organization of this chapter is as follows. In Section 2, the image model and sharpness metric used in our analysis are defined, and we state the optimization problem for metric-based SAR autofocus methods. In Section 3, we derive expressions for the intensity-squared objective function using one-dimensional (single-column) image models. Section 4 extends the analysis to two-dimensional (multicolumn) images. Using a

stochastic image model where the parameters of the model are selected according to a particular distribution, we demonstrate that as multiple image columns are combined to form the objective function, the gradient at the perfectly focused phase estimate approaches zero, satisfying the stationary point condition. In Section 5, we show that the multivariate objective function is approximately a separable function of the phase perturbations locally about the perfectly focused solution. In Section 6, we present numerical experiments using actual SAR imagery to validate the analytical results and show that the analysis extends well to realistic situations.

3.2 Problem Setup

3.2.1 SAR image models

We utilize a *dominant point-targets* model for the SAR image. Such a model can be considered as a rough representation of SAR and ISAR images when there is strong return from isolated scatterers. This simple, yet analytically tractable model has been used to motivate existing autofocus approaches [1, 10, 14, 15]. We consider the *sparse* discrete signal $\mathbf{g}_s \in \mathbb{C}^{M \times N}$, where each column of \mathbf{g}_s , representing a fixed range coordinate n or a single *range bin*, contains P weighted impulses:

$$g_s[m, n] = \sum_{p=0}^{P-1} a_p[n] e^{j\theta_p[n]} \delta[m - m_p[n]], \quad (3.1)$$

where $\delta[m]$ is the discrete unit impulse signal. Each impulse represents a point target with magnitude $a_p[n]$, spatial-domain phase shift $\theta_p[n]$, and location $m = m_p[n]$. We assume that the number of dominant targets is much smaller than the number of resolution cells (pixels) per range bin: $P \ll M$.

3.2.2 Image sharpness metrics

Metric-based autofocus algorithms use image sharpness metrics to evaluate the degree of focus. Because of the point-like nature of the SAR image model, maximizing sharpness

is found to increase the image focus. The aim of these methods is to determine the image in the search space (2.13) with maximum sharpness, as measured by a particular metric.

The metrics we consider are *additive* in the sense that the value of the metric, or *cost*, is a sum of contributions from each pixel individually. We define $\varphi : \mathbb{R}^+ \rightarrow \mathbb{R}$ as a concave *cost function* operating on the intensity of each pixel $I[m, n] \stackrel{\text{def}}{=} |g[m, n]|^2$. In this paper, we study the *intensity-squared* cost function [13–15, 17, 29]

$$\varphi(I) = -I^2. \quad (3.2)$$

The *metric* $\mathcal{C} : \mathbb{C}^{M \times N} \rightarrow \mathbb{R}$ maps the image \mathbf{g} to a sharpness cost

$$\mathcal{C}(\mathbf{g}) = \sum_{n=0}^{N-1} \sum_{m=0}^{M-1} \varphi(|g[m, n]|^2). \quad (3.3)$$

Due to the concavity of φ , sharpening the image (increasing the variance of the pixel intensities about their mean) decreases the value of the cost \mathcal{C} [15]. Therefore, we wish to *minimize* the metric \mathcal{C} (maximize sharpness).

3.2.3 SAR autofocus as an optimization problem

The *objective function* for the defocused image $\tilde{\mathbf{g}}$, $f_{\tilde{\mathbf{g}}} : [-\pi, \pi)^M \rightarrow \mathbb{R}$, is defined as

$$f_{\tilde{\mathbf{g}}}(\boldsymbol{\phi}) = \mathcal{C}(\tilde{\mathbf{g}}_{\boldsymbol{\phi}}), \quad (3.4)$$

where $\tilde{\mathbf{g}}_{\boldsymbol{\phi}}[m, n] = DFT_k^{-1}\{\tilde{G}[k, m]e^{-j\phi[k]}\}$ is an image in the search space (2.13). In other words, $f_{\tilde{\mathbf{g}}}(\boldsymbol{\phi})$ is the metric evaluated in the space of images formed from $\tilde{\mathbf{g}}$ by applying a particular Fourier phase correction function $\boldsymbol{\phi}$.

Metric-based autofocus methods employ *optimization algorithms*, which act on $\boldsymbol{\phi}$ to determine a minimizer of $f_{\tilde{\mathbf{g}}}$. However, the optimization techniques used in these methods may determine *local minimizers* of $f_{\tilde{\mathbf{g}}}$ [30, 35]. Therefore, we are interested in the behavior of the objective function locally about the perfectly focused image. We introduce the function

$$f_{\mathbf{g}}(\boldsymbol{\phi}) = \mathcal{C}(\mathbf{g}_{\boldsymbol{\phi}}), \quad (3.5)$$

where $g_\phi[m, n] = DFT_k^{-1}\{G[k, m]e^{-j\phi[k]}\}$. The function f_g is the objective function where the *origin* $\boldsymbol{\phi} = \mathbf{0}$ is defined with respect to \mathbf{g} instead of $\tilde{\mathbf{g}}$: $f_g(\boldsymbol{\phi}) = f_{\tilde{\mathbf{g}}}(-\boldsymbol{\phi}_e + \boldsymbol{\phi})$.

The key in our analysis is to derive expressions for $f_g(\phi\mathbf{e}_k)$, where \mathbf{e}_k is the k -th element of the standard basis for \mathbb{R}^M and $\phi\mathbf{e}_k$ ($\phi \in [-\pi, \pi)$) is the k -th component of $\boldsymbol{\phi}$, using the model \mathbf{g}_s in (3.1); note that ϕ is a scalar and $\boldsymbol{\phi}$ (in boldface) is a vector. Such expressions describe the objective function along the phase-error coordinate directions $\{\mathbf{e}_k\}_{k=0}^{M-1}$. The expressions are used to determine the conditions under which \mathbf{g}_s corresponds to a *stationary point* of the objective function. Stationary points are places where the gradient-based optimization algorithms in metric-based SAR autofocus terminate; such points satisfy the *first-order necessary condition for optimality* [30, 32]. The stationary point condition requires zero gradient at the origin of the objective function [30]:

$$\nabla f_g(\mathbf{0}) = \mathbf{0}, \quad (3.6)$$

where

$$\nabla f_g(\boldsymbol{\phi}) \Big|_{\boldsymbol{\phi}=\mathbf{0}} = \left[\frac{\partial f_g(\phi\mathbf{e}_0)}{\partial \phi} \Big|_{\phi=0}, \dots, \frac{\partial f_g(\phi\mathbf{e}_{M-1})}{\partial \phi} \Big|_{\phi=0} \right]. \quad (3.7)$$

3.3 Analysis of Single-Column Image Models

3.3.1 Approximate expressions for the objective function

In this section, we analyze one column of the dominant point-targets model \mathbf{g}_s in (3.1), which represents a fixed range coordinate n (i.e., a single range bin):

$$g[m] = \sum_{p=1}^P a_p e^{j\theta_p} \delta[m - m_p]. \quad (3.8)$$

We first characterize the effect on the image of perturbing a single component $\phi\mathbf{e}_k$ of the Fourier phase of \mathbf{g} . Such a characterization is then used to derive an approximate expression for the squared image intensity as a function of $\phi\mathbf{e}_k$, which leads directly to expressions for $f_g(\phi\mathbf{e}_k)$.

The *perturbed image* $\mathbf{g}_{\phi\mathbf{e}_k}$ is defined as the image formed by perturbing the k -th component of the Fourier phase of \mathbf{g} by an amount ϕ (i.e., $\angle G[k] + \phi$):

$$g_{\phi\mathbf{e}_k}[m] \stackrel{\text{def}}{=} DFT_{k'}^{-1}\{DFT_{m'}\{g[m']\}e^{j\phi\delta[k'-k]}\}. \quad (3.9)$$

This may be alternatively expressed as

$$g_{\phi\mathbf{e}_k}[m] = g[m] + \varepsilon_{\phi\mathbf{e}_k}[m], \quad (3.10)$$

where

$$\varepsilon_{\phi\mathbf{e}_k}[m] = (e^{j\phi} - 1)s_k[m] \quad (3.11)$$

is the update to pixel m due to ϕ , and $s_k[m]$ is the *subband* image:

$$s_k[m] = \frac{1}{M}G[k]e^{j2\pi km/M}. \quad (3.12)$$

The $(e^{j\phi} - 1)$ term comes from subtracting out the k -th term in the Fourier sum where the phase has not been perturbed, and adding in a new term where the phase has been perturbed by $\phi\mathbf{e}_k$.

We derive an approximate expression for the squared intensity of the perturbed image:

$I_{\phi\mathbf{e}_k}^2[m] = |g_{\phi\mathbf{e}_k}[m]|^4$. Using (3.10),

$$\begin{aligned} I_{\phi\mathbf{e}_k}^2[m] &= |g[m] + \varepsilon_{\phi\mathbf{e}_k}[m]|^4 = ((g[m] + \varepsilon_{\phi\mathbf{e}_k}[m])(g^*[m] + \varepsilon_{\phi\mathbf{e}_k}^*[m]))^2 \\ &= |g[m]|^4 + 4\Re\{|g[m]|^2 g^*[m] \varepsilon_{\phi\mathbf{e}_k}[m]\} + 2|g[m]|^2 |\varepsilon_{\phi\mathbf{e}_k}[m]|^2 \\ &\quad + 4\Re\{|\varepsilon_{\phi\mathbf{e}_k}[m]|^2 g^*[m] \varepsilon_{\phi\mathbf{e}_k}[m]\} + 4(\Re\{g^*[m] \varepsilon_{\phi\mathbf{e}_k}[m]\})^2 + |\varepsilon_{\phi\mathbf{e}_k}[m]|^4, \end{aligned} \quad (3.13)$$

where \Re denotes the real part of the argument. We approximate (3.13) by retaining the first two terms; this is equivalent to the first-order Taylor series expansion of (3.13) about $\varepsilon_{\phi\mathbf{e}_k}[m] = 0$:

$$I_{\phi\mathbf{e}_k}^2[m] \approx I^2[m] + 4\Re\{I[m]g^*[m]\varepsilon_{\phi\mathbf{e}_k}[m]\}, \quad (3.14)$$

where $I[m] = |g[m]|^2$ and $I^2[m] = |g[m]|^4$. The benefit of using an approximation is that the expression is linear in the image update $\varepsilon_{\phi\mathbf{e}_k}[m]$, which will result in a simplified and intuitive expression for the objective function. To justify that (3.14) is an accurate

approximation, we show that $|\varepsilon_{\phi \mathbf{e}_k}[m]| \ll |g[m]|$ at pixels where a target is present (i.e., $m = m_p$). Using $|(e^{j\phi} - 1)| \leq |\phi| \leq \pi$, and $|G[k]| \leq \sum_m |g[m]| \leq P \|\mathbf{g}\|_\infty$ on (3.11) and (3.12), we have the upper bound

$$|\varepsilon_{\phi \mathbf{e}_k}[m]| \leq \frac{P}{M} |\phi| \|\mathbf{g}\|_\infty \quad (3.15)$$

for all m and k . Thus if

$$\frac{P}{M} |\phi| \ll 1, \quad (3.16)$$

then the approximation in (3.14) is accurate. Note that this is true for the sparse model (3.8) where $P \ll M$. As an example, let $P = 24$, $M = 1024$, and $|\phi| = \pi$. Then $\frac{P}{M} |\phi| \approx 0.074 \ll 1$. Since $|\varepsilon_{\phi \mathbf{e}_k}[m]|$ decreases with decreasing ϕ , the approximation (3.14) becomes especially good for small phase perturbations (e.g., $|\phi| \leq \frac{\pi}{4}$). Thus, the expression for the objective function will be highly accurate locally about the perfectly focused solution.

Using (3.11) and (3.14), the intensity-squared objective function evaluated for a single phase perturbation $\phi \mathbf{e}_k$ is expressed as

$$\begin{aligned} f_g(\phi \mathbf{e}_k) &= - \sum_{m=0}^{M-1} I_{\phi \mathbf{e}_k}^2[m] \\ &\approx - \sum_{m=0}^{M-1} I^2[m] - \Re \left\{ (e^{j\phi} - 1) z_k \right\}, \end{aligned} \quad (3.17)$$

where

$$z_k = 4 \sum_{m=0}^{M-1} I[m] g^*[m] s_k[m]. \quad (3.18)$$

Note that (3.17) can be rewritten as

$$f_g(\phi \mathbf{e}_k) \approx c_k - |z_k| \cos(\phi + \angle z_k), \quad (3.19)$$

where $c_k = - \sum_{m=0}^{M-1} I^2[m] + \Re\{z_k\}$ is a constant given the perfectly focused image.

The expression (3.19) reveals that the behavior of $f_g(\phi \mathbf{e}_k)$ for every k is described by a cosine function with an amplitude and phase shift dependent on the complex number z_k , which is a function of the perfectly focused image model. We note that expressions similar

to (3.19) have been derived independently in [17] and [18] using different approximations and assumptions.

Using (3.8), we define (3.18) explicitly in terms of the model parameters:

$$z_k = \frac{4}{M} \sum_{p=0}^{P-1} \sum_{l=0}^{P-1} a_l^3 a_p e^{j\psi_k[l,p]} \quad (3.20)$$

where

$$\psi_k[l, p] = \theta_p - \theta_l + \frac{2\pi}{M} k(m_l - m_p). \quad (3.21)$$

The contribution of the spatial-domain phases and the locations of the pair of targets at $m = m_l, m_p$ resides exclusively within the parameter $\psi_k[l, p]$.

The expression (3.20) shows that z_k is generally not real-valued, so $\angle z_k \neq 0$ in general. For the stationary point condition of $f_g(\phi \mathbf{e}_k)$ given in (3.19) to be satisfied, a necessary and sufficient condition is that $\angle z_k = 0$ for all k . The presence of the $\angle z_k$ *phase shift* causes the minima of $f_g(\phi \mathbf{e}_k)$ to be displaced from the origin, so that the perfectly focused image does not correspond to a stationary point.

3.3.2 Validation of the approximate expression

Figure 3.1(a) shows the magnitude of a three-target realization of the image model (i.e., $P = 3$) with $M = 128$. The plot in Figure 3.1(b) shows the behavior of the objective function along the coordinate direction \mathbf{e}_{18} (selected as a representative example) on the interval $[-\pi, \pi)$ for the model in Figure 3.1(a). The exact numerically evaluated metric is displayed as a solid curve, and the approximate expression in (3.19) is displayed as a dashed curve. The approximate expression is observed to be in excellent agreement with the exact expression, particularly for small ϕ . Similar agreement is found using other directions \mathbf{e}_k and other realizations of the model g .

In this example, the objective function in Figure 3.1(b) does not have a minimum at the origin (since the minimum of $f_g(\phi \mathbf{e}_{18})$ is not at $\phi = 0$), and applying the optimization to the perfectly focused image would produce an erroneous restoration. In general, metric-based methods cannot restore a single column of the SAR image. However, we

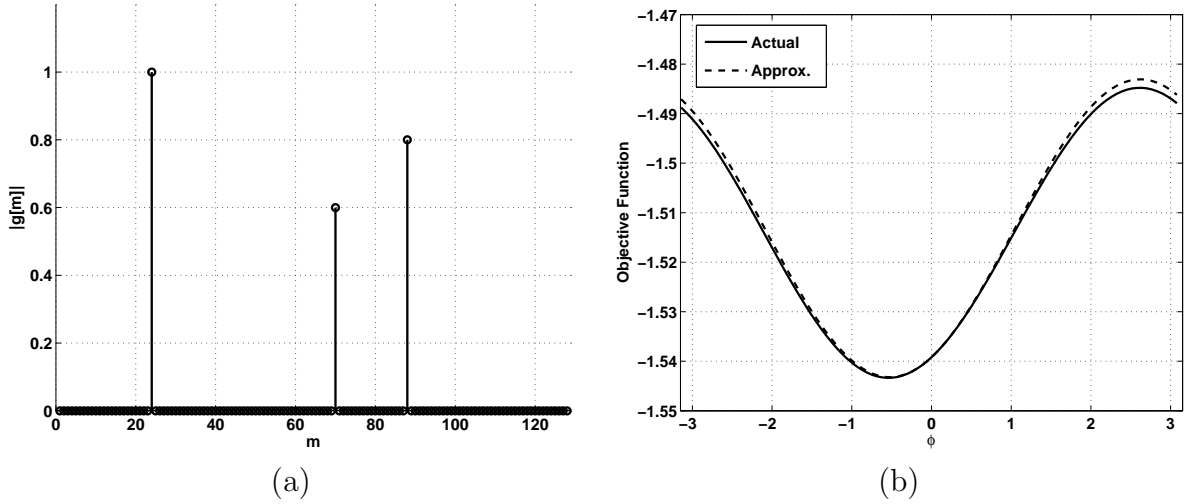


Figure 3.1 An approximate expression for the objective function using the intensity-squared cost: (a) perfectly focused range bin model, and (b) plots of $f_g(\phi \mathbf{e}_{18})$ versus $\phi \in [-\pi, \pi)$ for the model in (a), where the solid plot shows the exact numerically evaluated metric, and the dashed plot uses the approximate expression in (3.19).

will show that the image model in (3.1) with multiple image columns can be properly focused through these techniques. In the next section, we demonstrate that the combination of the objective functions arising from each column individually causes the origin of the objective function for the multicolumn image to approach a stationary point.

3.4 Analysis of Multicolumn Image Models

3.4.1 Asymptotic analysis

In the previous section, we determined expressions for the objective function considering only a single image column. Since the metrics we consider are additive, the objective function evaluated for a multicolumn image can be expressed as the sum of the objective functions evaluated for each image column individually:

$$f_g(\phi \mathbf{e}_k) = \sum_{n=0}^{N-1} f_{g^{[n]}}(\phi \mathbf{e}_k), \quad (3.22)$$

where $\mathbf{g}^{[n]}$ denotes the n -th column of \mathbf{g} . Our goal is to show that when a large number of columns of the point-targets model are incorporated, the origin of the objective function approaches a stationary point. To quantitatively demonstrate this, we employ a *stochastic* image model for \mathbf{g} by analogy with (3.1):

$$g[m, n] = \sum_{p=0}^{P-1} A_p[n] e^{j\Theta_p[n]} \delta[m - m_p[n]], \quad (3.23)$$

where $A_p[n]$ and $\Theta_p[n]$ are random variables characterizing the target magnitudes and spatial-domain phases, respectively. The following statistical assumptions are used in the analysis:

- The magnitudes $A_p[n]$ are *independent and identically distributed (i.i.d.)*, with a distribution on \mathbb{R}^+ having a finite variance.
- The spatial-domain phases $\Theta_p[n]$ are independent and uniformly distributed between $-\pi$ and π .
- The random variables $A_p[n]$ and $\Theta_p[n]$ are independent of each other.

The target locations $m_p[n]$ may be arbitrary, given that no two targets are assigned the same location: $m_p[n] \neq m_q[n]$ for all $p, q : p \neq q$. The random phase assumption is accurate for many scenarios where the surface roughness is on the scale of the radar wavelength [1, 36, 37]. In fact, the assumption has been shown to be important for SAR image reconstruction; similar to holographic imaging, random phase permits formation of high-resolution images from bandlimited, frequency-offset Fourier data [36].

Using the expression (3.17) in (3.22) yields

$$\begin{aligned} f_g(\phi \mathbf{e}_k) &\approx - \sum_{n=0}^{N-1} \sum_{m=0}^{M-1} I^2[m, n] - \Re \left\{ (e^{j\phi} - 1) \sum_{n=0}^{N-1} Z_k[n] \right\}, \\ &= C_k - \left| \sum_{n=0}^{N-1} Z_k[n] \right| \cos \left(\phi + \angle \sum_{n=0}^{N-1} Z_k[n] \right) \end{aligned} \quad (3.24)$$

where $Z_k[n]$ is the coefficient z_k in (3.21) evaluated for range coordinate n using the model (3.23):

$$Z_k[n] = \frac{4}{M} \sum_{p=0}^{P-1} \sum_{l=0}^{P-1} A_l^3[n] A_p[n] e^{j\Psi_k[l, p, n]}, \quad (3.25)$$

$$\Psi_k[l, p, n] = \Theta_p[n] - \Theta_l[n] + \frac{2\pi}{M}k(m_l[n] - m_p[n]), \quad (3.26)$$

and $C_k = -\sum_{m,n} I^2[m, n] + \Re\{\sum_n Z_k[n]\}$. Note that since $A_p[n]$ and $\Theta_p[n]$ are i.i.d. in n , $Z_k[n]$ is an i.i.d. sequence in n for every k .

Define

$$\Omega_k^{[N]} = \angle \sum_{n=0}^{N-1} Z_k[n] \quad (3.27)$$

to be the phase shift associated with the k -th coordinate direction. The *Strong Law of Large Numbers* will be used to show that, as N becomes large, the sum over $Z_k[n]$ converges to its expected value (scaled by N). We then will show that the expected value is real-valued, so that $\lim_{N \rightarrow \infty} \Omega_k^{[N]} = 0$ for all k , demonstrating that $\phi = \mathbf{0}$ is a stationary point of f_g . For fixed k , the Strong Law implies that with probability one [38]:

$$\frac{1}{N} \sum_{n=0}^{N-1} Z_k[n] \rightarrow E_{A,\Theta}[Z_k] \text{ as } N \rightarrow \infty, \quad (3.28)$$

where $E_{A,\Theta}$ is the expected value with respect to A and Θ . Due to the uniform distribution on the spatial-domain phases, from (3.26) we see that $e^{j\Psi_k[l,p,n]} = 1$ if $l = p$ and otherwise is uniformly distributed on the unit circle, so that

$$E_{\Theta}[e^{j\Psi_k[l,p,n]}] = \begin{cases} 1 & \text{for } l = p \\ 0 & \text{otherwise.} \end{cases} \quad (3.29)$$

As a result, only terms in (3.25) where $l = p$ contribute to the expectation:

$$\mu_Z \stackrel{\text{def}}{=} E_{A,\Theta}[Z_k] = \frac{4}{M} P E_A[A^4]. \quad (3.30)$$

Therefore, for large N we have

$$\sum_{n=0}^{N-1} Z_k[n] \approx N\mu_Z, \quad (3.31)$$

which due to (3.30) is positive and real-valued.

Using (3.31), the expression (3.24) for large N becomes

$$f_g(\phi \mathbf{e}_k) \approx C - N\mu_Z \cos(\phi), \quad (3.32)$$

where $C = -\sum_{n,m} I^2[m, n] - N\mu_Z$. Thus, we see that the stationary point condition is satisfied (i.e., $\left. \frac{\partial f_g(\phi \mathbf{e}_k)}{\partial \phi} \right|_{\phi=0} = 0$ for all k), and the metric is nondecreasing along each coordinate direction.

3.4.2 Quantitative analysis for a finite number of columns

Expressing the phase shift (3.27) in terms of the real and imaginary parts of $Z_k[n]$:

$$\Omega_k^{[N]} = \tan^{-1} \left[\frac{\sum_{n=0}^{N-1} \Im\{Z_k[n]\}}{\sum_{n=0}^{N-1} \Re\{Z_k[n]\}} \right], \quad (3.33)$$

where \Im specifies the imaginary part of the argument. We approximate (3.33) using two observations. First, $\sum_{n=0}^{N-1} \Re\{Z_k[n]\} \gg \sum_{n=0}^{N-1} \Im\{Z_k[n]\}$, which is based on (3.31) being purely real; this implies

$$\Omega_k^{[N]} \approx \frac{\sum_{n=0}^{N-1} \Im\{Z_k[n]\}}{\sum_{n=0}^{N-1} \Re\{Z_k[n]\}}. \quad (3.34)$$

Furthermore, it can be shown that the expected value of the denominator in (3.34) is much greater than its variance, so we make the approximation that only the variation in the numerator is significant, and approximate the denominator using its mean $\sum_{n=0}^{N-1} \Re\{Z_k[n]\} \approx N\mu_Z$:

$$\Omega_k^{[N]} \approx \sum_{n=0}^{N-1} \frac{\Im\{Z_k[n]\}}{N\mu_Z}. \quad (3.35)$$

To determine how quickly the phase shifts tend to zero, we examine the variance as a function of N . Using (3.35), it can be shown that

$$\sigma_{\Omega}^2[N] \stackrel{\text{def}}{=} \text{Var}[\Omega_k^{[N]}] \approx \left(\frac{\lambda P - 1}{2P} \right) \frac{1}{N}, \quad (3.36)$$

where

$$\lambda = \frac{E_A[A^6]E_A[A^2] - (E_A[A^4])^2}{(E_A[A^4])^2}. \quad (3.37)$$

Since (3.35) is a sum of i.i.d. random variables with finite variance, by the central limit theorem $\Omega_k^{[N]}$ approaches a normal distribution with mean zero and variance $\sigma_{\Omega}^2[N]$ [39]. The key is noting that as the number of columns increases, the variance of the phase shifts decreases as $1/N$. Thus, there is fast convergence to a stationary point with a relatively small number of columns.

3.4.3 Validation of analytical results

We consider the stochastic image model in (3.23) with $M = 64$ and $P = 9$, where the target magnitudes A_p are uniformly distributed on the interval $(0, 1]$ and the target locations are selected at random without replacement from the set of indices $m_p \in \{0, 1, \dots, M - 1\}$. One column of this model is shown in Figure 3.2(a). Figures 3.2(b)-(f) show an experiment demonstrating the reinforcement of metric minima as an increased number of columns are included in the stochastic model. Plots of the objective function along each coordinate direction $f_g(\phi \mathbf{e}_k)$, $k = 0, 1, \dots, M - 1$, (where, for comparison, the plots have been scaled to unity and the constant offset has been removed) are shown superimposed in Figure 3.2(b) for a single column of the stochastic model ($N = 1$). The metric minima are observed to be distributed with a large variance about $\phi = 0$. Figure 3.2(c) shows plots of the objective function for $N = 3$; here, the metric minima are distributed more closely about the origin. Further plots for $N = 10$, $N = 64$, and $N = 256$ are shown in Figures 3.2(d), (e), and (f), respectively. These figures reveal that as more image columns are introduced, the contributions of the phase shifts $\angle Z_k[n]$ associated with each column average out, producing a stationary point at the origin.

To examine how the deviations of the metric minima from the origin decrease with an increasing number of columns, we examine the squared ℓ_2 -norm of the phase shifts as a function of N : $\|\boldsymbol{\Omega}^{[N]}\|_2^2$, where $\boldsymbol{\Omega}^{[N]}$ is a vector of the phase shifts from every coordinate direction $k = 0, 1, \dots, M - 1$. Figure 3.3 shows a plot (in log scale) of $\|\boldsymbol{\Omega}^{[N]}\|_2^2$ for the stochastic model considered in the experiment of Figures 3.2(a)-(f); this plot is displayed using cross markers. It can be shown that $\|\boldsymbol{\Omega}^{[N]}\|_2^2 \rightarrow M\sigma_\Omega^2[N]$ as N increases. A plot of $M\sigma_\Omega^2[N] \sim \frac{1}{N}$ is shown in the dashed curve of Figure 3.3 for comparison. The plots reveal that the deviations from $\phi = 0$ decrease sharply in the regime of small N . We can infer from this that the averaging effect takes place for a relatively small number of range bins containing dominant point targets; this provides justification for why metric-based methods work well for many practical SAR images.

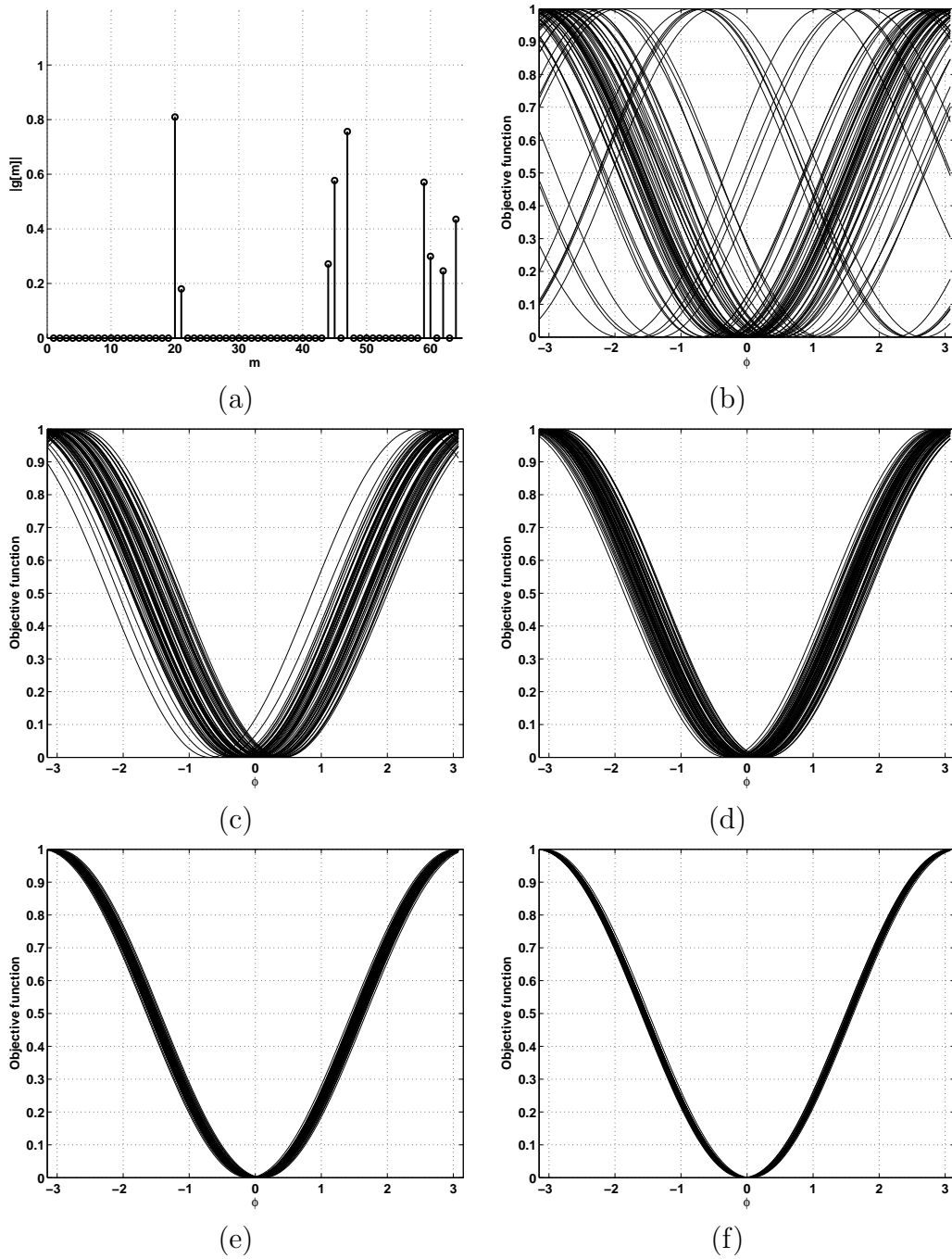


Figure 3.2 Demonstration of the reinforcement of metric minima as an increased number of columns are included in the stochastic model. (a) One column of the stochastic model ($P = 9$, $M = 64$). (b)-(f): Normalized plots of the objective function along each coordinate direction $f_g(\phi \mathbf{e}_k)$, $k = 0, 1, \dots, M - 1$ (shown superimposed), where (b) $N = 1$, (c) $N = 3$, (d) $N = 10$, (e) $N = 64$, and (f) $N = 256$.

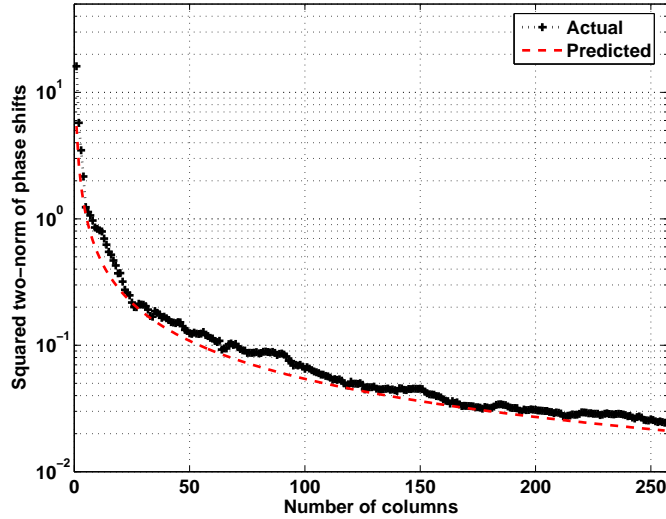


Figure 3.3 Log-scale plot showing the squared ℓ_2 -norm of the phase shifts (i.e., deviations from $\phi = 0$) as a function of the number of columns N (plot with cross markers). The behavior as a function of N is found to be proportional to $\frac{1}{N}$ (displayed in the dashed curve).

In summary so far, we have demonstrated that, in general, a single column of the dominant point-targets model does not correspond to a stationary point. However, when the metric is evaluated on a large number of image columns, the metric minima along each \mathbf{e}_k due to the phase shifts $\angle Z_k[n]$ reinforce each other to form a minimum at $\phi = 0$. This averaging mechanism produces a stationary point at the origin, allowing the perfectly focused image to be properly restored. This observation is the key to understanding why metric-based approaches are successful.

3.5 Separable Approximation for the Multivariate Objective Function

We observe that locally about the origin, the objective function is approximately a *separable* function of the phase perturbations. That is, within a radius of the origin (e.g., $\|\phi\|_2 < \mathcal{V}$, $\mathcal{V} \in \mathbb{R}$), the objective function is essentially a sum of terms that depend upon each phase component $\phi \mathbf{e}_k$ individually. To help formalize this finding, we derive

an approximate expression for the multivariate objective function $f_g(\boldsymbol{\phi})$ that is separable in $\boldsymbol{\phi}\mathbf{e}_k$, and we show that this approximation becomes more accurate as $\|\boldsymbol{\phi}\|_2$ decreases. This approximation provides a local characterization of the second-order properties of the objective function.

Similar to our derivation of (3.14), we approximate the perturbed intensity as a function of the *vector* of phase perturbations $\boldsymbol{\phi}$ using a first-order Taylor approximation. Analogous to (3.10), we write the phase-perturbed image as

$$g_\phi[m, n] = g[m, n] + \varepsilon_\phi[m, n], \quad (3.38)$$

where the image update can be expressed using (3.11) and (3.12) as

$$\varepsilon_\phi[m, n] = \sum_{k=0}^{M-1} \varepsilon_{\phi_k \mathbf{e}_k}[m, n] = \frac{1}{M} \sum_{k=0}^{M-1} (e^{j\phi_k} - 1)G[k, n]e^{j2\pi km/M}, \quad (3.39)$$

ϕ_k is the k -th component of $\boldsymbol{\phi}$, and $\varepsilon_{\phi_k \mathbf{e}_k}[m, n]$ is defined in (3.11) (for fixed n). Using (3.38), and taking steps similar to those leading to (3.14) yields the approximation

$$I_\phi^2[m, n] \approx I^2[m, n] + 4 \sum_{k=0}^{M-1} \Re\{I[m, n]g^*[m, n]\varepsilon_{\phi_k \mathbf{e}_k}[m, n]\}. \quad (3.40)$$

The approximation in (3.40) is accurate when $|\varepsilon_\phi[m, n]|$ is small compared to $|g[m, n]|$. Analogous to (3.15), $|\varepsilon_\phi[m, n]|$ can be bounded from above as follows. Let g be the model described by (3.1). Employing steps similar to those used to derive (3.15), from (3.39) we have $|\varepsilon_\phi[m, n]| \leq \frac{1}{M} \sum_{k=1}^{M-1} |\phi_k| |G[k, n]| \leq \frac{1}{M} \|\boldsymbol{\phi}\|_2 \|\mathbf{G}^{[n]}\|_2$, where the last inequality is a result of Cauchy-Schwarz and the superscript $[n]$ denotes the n -th column. Using $\|\mathbf{G}^{[n]}\|_2 = \sqrt{M} \|\mathbf{g}^{[n]}\|_2 \leq \sqrt{MP} \|\mathbf{g}\|_\infty$ we obtain

$$|\varepsilon_\phi[m, n]| \leq \sqrt{\frac{P}{M}} \|\boldsymbol{\phi}\|_2 \|\mathbf{g}\|_\infty, \quad (3.41)$$

for all m and n . Thus if

$$\sqrt{\frac{P}{M}} \|\boldsymbol{\phi}\|_2 \ll 1, \quad (3.42)$$

then the approximation (3.40) is accurate. Note that this is true for sparse images ($P \ll M$) and small phase perturbations.

Using the approximation (3.40), we have

$$\begin{aligned}
f_g(\boldsymbol{\phi}) &= - \sum_{n=0}^{N-1} \sum_{m=0}^{M-1} I_{\boldsymbol{\phi}}^2[m, n] \\
&\approx - \sum_{n=0}^{N-1} \sum_{m=0}^{M-1} I^2[m, n] - \sum_{k=0}^{M-1} \Re \left\{ (e^{j\phi_k} - 1) \sum_{n=0}^{N-1} z_k[n] \right\} \\
&= \sum_{k=0}^{M-1} f_g(\phi_k \mathbf{e}_k) + \gamma.
\end{aligned} \tag{3.43}$$

where $z_k[n]$ is defined in (3.20) for (fixed n) and $\gamma = (M - 1) \sum_{n=0}^{N-1} \sum_{m=0}^{M-1} I^2[m, n]$.

A consequence of (3.43) is that when the phase errors are small enough, we can optimize the multivariate objective function $f_{\tilde{g}}(\boldsymbol{\phi})$ by optimizing each phase component in $\boldsymbol{\phi}$ independently. This observation underlies the success of efficient monotonic iterative optimization algorithms for metric-based SAR autofocus [17, 18], where the phase components are optimized simultaneously and independently at each iteration.

3.6 Experimental Results

To demonstrate how our analysis extends to actual SAR imagery, we performed numerical simulations using actual SAR images. We first consider the perfectly focused 600×600 pixel SAR image in Figure 3.4(a), which is formed from a given defocused image by applying an I^2 -minimization autofocus routine [18]. Figure 3.4(b) shows normalized plots of the objective function using the image in (a) for each coordinate direction. As predicted by theory, the plots of the objective function for the perfectly focused image are described by cosine functions, with minima at $\phi = 0$ (note that since the all of the plots lie on top of each other, they resemble a single plot). To show that a single column of the image does not correspond to a stationary point, we evaluate plots of the objective function for column 491 (selected as a representative example), which are displayed in Figure 3.4(c). The objective function minima for the single column exhibit large variation about the origin. Figure 3.4(b) reveals that the effects of these minima are averaged

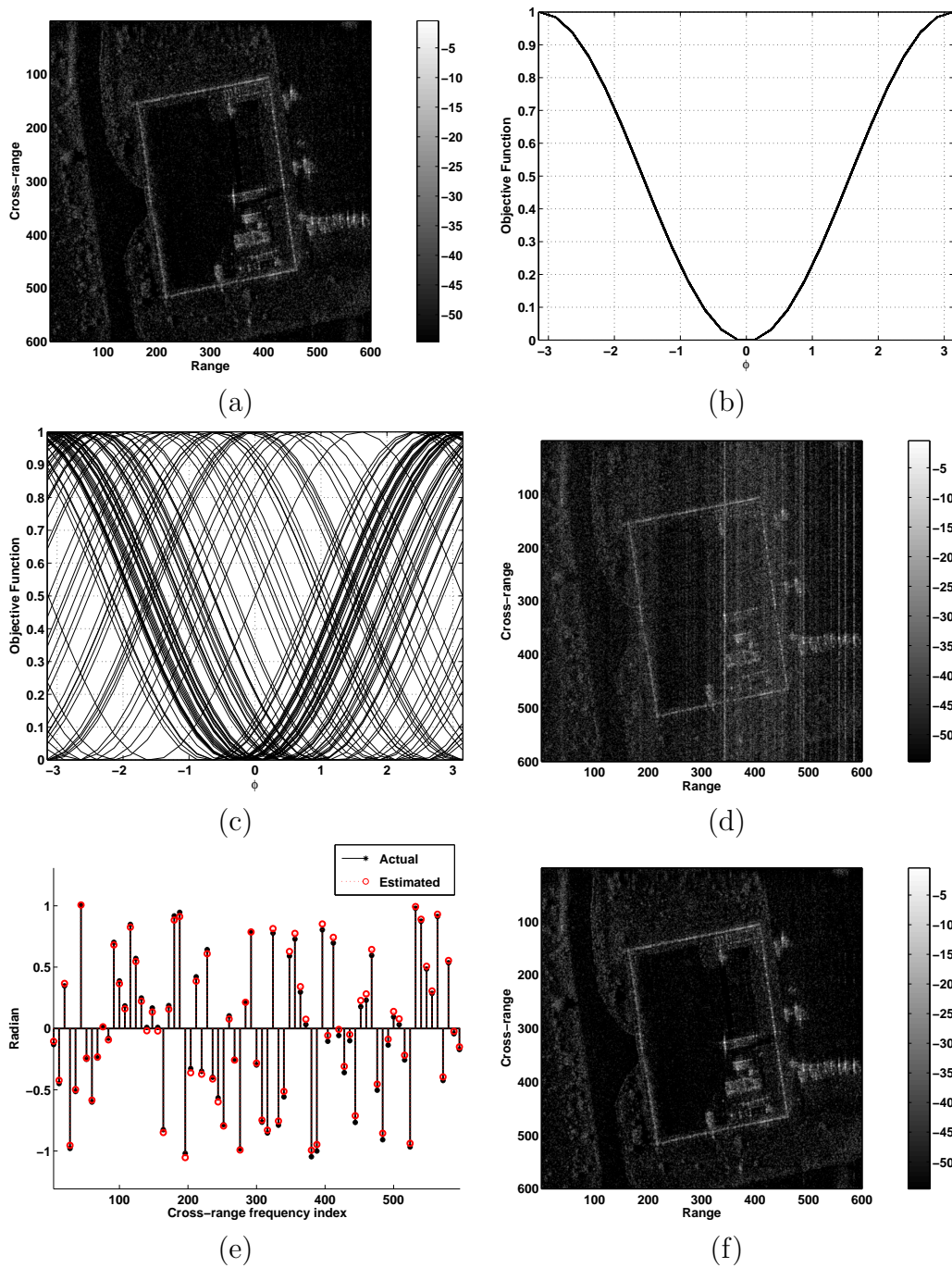


Figure 3.4 Experiment with an actual SAR image. (a) Intensity of perfectly focused SAR image (displayed in dB), (b) plots of the objective function ($k = 0, 1, \dots, 600$) for the image in (a), (c) plots of the objective function for column 491 ($k = 3, 11, 19, \dots, 595$), (d) defocused image where a small white phase error has been applied to (a), (e) applied phase error $\phi_e[k]$ (star markers) and phase estimate from simultaneous 1-D searches (circle markers) ($k = 3, 11, 19, \dots, 595$), and (f) image restored by applying the phase estimate in (e).

out when the contributions of all the columns are taken into account, as demonstrated in our analysis.

We have demonstrated that locally about the origin, the objective function can be approximated as a separable function of the phase perturbations. To show this using actual data, we apply a small random phase error, with independent components uniformly distributed between $-\frac{\pi}{3}$ and $\frac{\pi}{3}$, to the perfectly focused image in Figure 3.4(a). The resulting defocused image is displayed in Figure 3.4(d). Figure 3.4(e) shows a plot of the phase shifts Ω_k for the *defocused* image (displayed in circle markers), determined by numerically performing 1-D searches along each coordinate direction, superimposed on a plot of the applied phase errors $\phi_e[k]$ (displayed in star markers) for $k = 3, 11, 19, \dots, 595$. We see that these plots are in agreement, demonstrating that the effect of applying small phase perturbations to the perfectly focused image is to shift the objective function minima by an amount equal to the phase errors. Thus, in the local regime, the phase error can be determined by performing M simultaneous one-dimensional searches along each coordinate direction (i.e., *simultaneous coordinate descent*). Figure 3.4(f) shows the restored image formed in this manner.

The image in Figure 3.4(a) consists of point-like features (e.g., corner reflections) against a low-return background, and thus the model in (3.1) is a good approximation to this actual image. To determine how the analysis extends to actual SAR images not well-described by the dominant point-targets model, we consider the perfectly focused terrain image of size 2027 by 2335 in Figure 3.5(a). As in the previous experiment, the perfectly focused image is formed from a defocused image by applying I^2 -minimization autofocus. Figure 3.5(b) shows normalized plots of the objective function using the image in (a) for the subset of coordinate directions $k = 95, 191, 287, \dots, 2015$. As in the experiment of Figure 3.4, the metric minima for each coordinate direction are located at $\phi = 0$. Figure 3.5(c) shows plots of the objective function for a single column (column 680) for the same subset of coordinate directions. As expected, the figure reveals that the stationary point condition is not satisfied for the single image column.

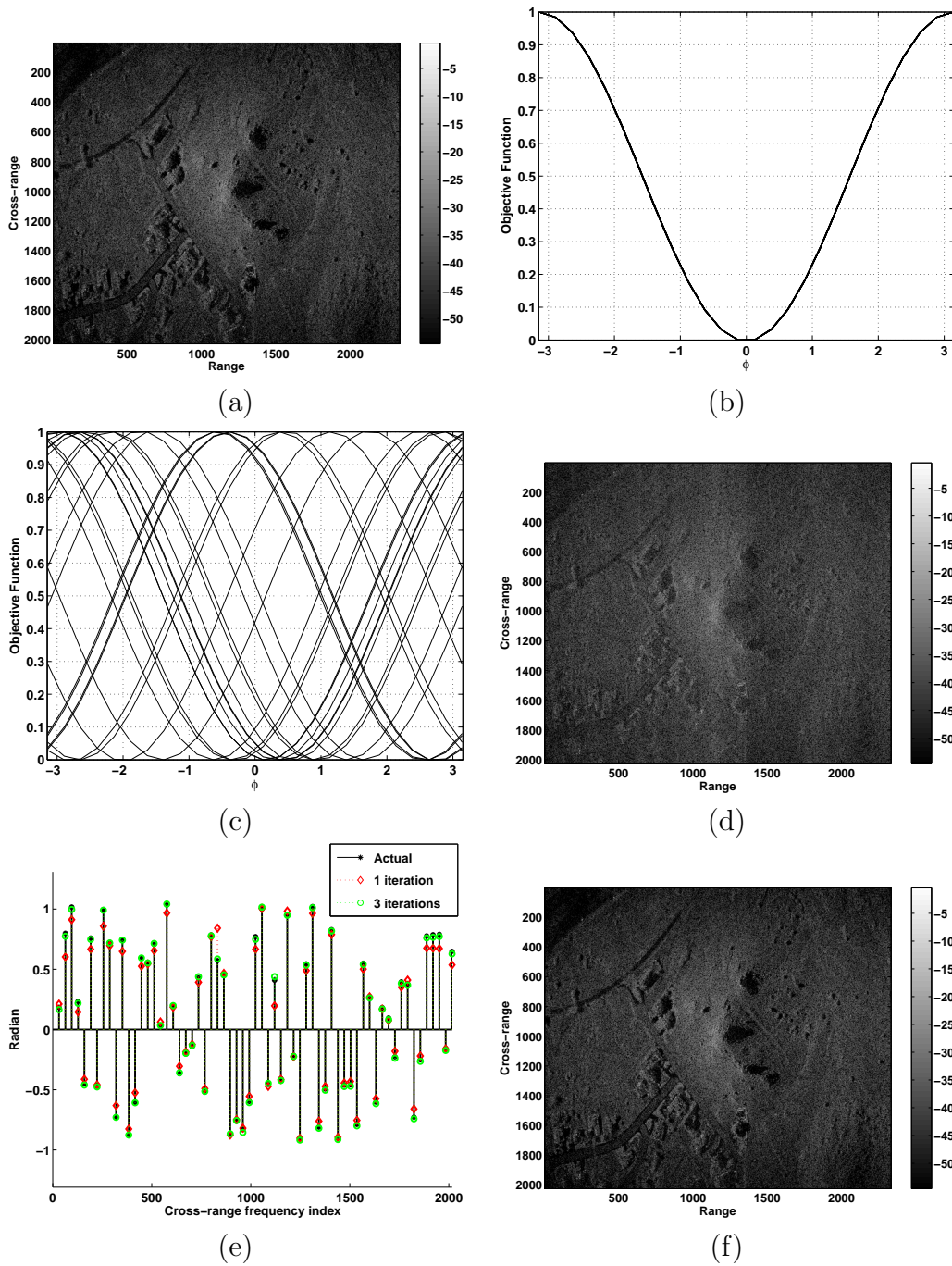


Figure 3.5 Experiment with an actual SAR image. (a) Intensity of perfectly focused SAR image (displayed in dB), (b) plots of the objective function ($k = 95, 191, 287, \dots, 2015$) for the image in (a), (c) plots of the objective function for column 680 ($k = 95, 191, 287, \dots, 2015$), (d) defocused image, (e) applied phase error $\phi_e[k]$ (star markers), and phase estimate obtained after one iteration of simultaneous coordinate descent (diamond markers) and three iterations (circle markers) for $k = 31, 63, \dots, 2015$, and (f) image restored after three iterations of simultaneous coordinate descent.

From the analysis in (3.41), the separable approximation (3.43) is expected to hold well when the phase perturbations are small and the SAR image is sparse with a small number of point targets per range bin. To determine how well the separable approximation holds for the image in Figure 3.5(a), we apply a small random phase error with independent components uniformly distributed between $-\frac{\pi}{3}$ and $\frac{\pi}{3}$. The resulting defocused image is shown in Figure 3.5(d). As in the experiment using the previous image, we applied a single iteration of simultaneous coordinate descent (i.e., M independent 1-D searches) to the defocused image to determine an estimate of the phase error. The phase estimate is displayed in diamond markers in Figure 3.5(e), plotted with the actual phase error in star markers for $k = 31, 63, \dots, 2015$. We observe that the phase estimate is not as accurate as the estimate produced in the experiment in Figure 3.4(e). This is expected, since the image in Figure 3.5(a) is not sparse like the previous image, and the separable approximation should hold less well. The plot denoted by circle markers in Figure 3.5(e) shows the result of applying three iterations of simultaneous coordinate descent; here, the phase error is recovered with a high degree of accuracy. We note that although the sparsity assumption holds weakly for the image in Figure 3.5(a), a rough estimate of the phase error is produced after a single iteration. However, when the applied phase errors are outside of the range $[-\frac{\pi}{3}, \frac{\pi}{3})$, we have observed through experiments that the phase estimate obtained through a single iteration is not correct. This suggests that within a neighborhood of the local optimum, simultaneous coordinate descent can converge very quickly to the true phase estimate using a small number of iterations, even when the actual SAR image is poorly approximated by the ideal model (3.1). The simultaneous coordinate descent can be performed efficiently in an iterative fashion using the framework in [18].

CHAPTER 4

MCA: A MULTICHANNEL APPROACH TO SAR AUTOFOCUS

4.1 Introduction

In this chapter, we present a new approach to SAR autofocus, termed the *Multi-Channel Autofocus* (MCA) algorithm, where a linear algebraic formulation is used to recover the perfectly focused image from the given defocused data. In contrast to previous SAR autofocus approaches, our technique does not invoke specific prior assumptions about the characteristics of the SAR scene, such as the suitability of sharpness metrics or knowledge of dominant point scatterers. While the restoration results obtained using previous approaches are often outstanding, the techniques sometimes fail to produce correct restorations. The restorations tend to be inaccurate when the underlying scene is poorly described by the assumed image model.

From the defocusing relationship in (2.11), we see that there is a multichannel nature to the SAR autofocus problem. Figure 4.1 presents this analogy: the columns $\mathbf{g}^{[n]}$ of the perfectly focused image \mathbf{g} can be viewed as a bank of parallel filters that are excited by a common input signal, which is the blurring kernel \mathbf{b} . Thus, there is a similarity to *blind multichannel deconvolution* (BMD) problems in that both the channel responses (i.e., perfectly focused image columns) and input (i.e., blurring kernel) are unknown, and it is desired to reconstruct the channel responses given only the output signals (i.e., defocused image columns) [41]. However, there are two main differences between the

This chapter includes research conducted jointly with David C. Munson Jr. and Minh N. Do [40].

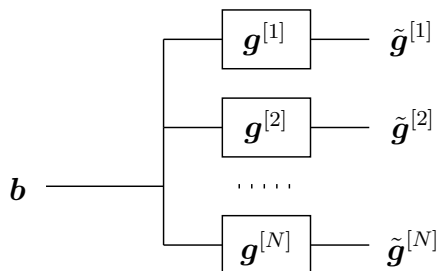


Figure 4.1 Diagram illustrating the multichannel nature of the autofocus problem. Here, \mathbf{b} is the blurring kernel, $\{\mathbf{g}^{[n]}\}$ are the perfectly focused image columns, and $\{\tilde{\mathbf{g}}^{[n]}\}$ are the defocused columns.

SAR autofocus problem considered here and the setup assumed in the BMD literature. First, the filtering operation in the SAR autofocus problem is described by *circular* convolution, as opposed to standard discrete-time convolution. Second, the channel responses $\mathbf{g}^{[n]}$, $n = 0, 1, \dots, N - 1$, in the autofocus problem are not short-support FIR filters, but instead have support over the entire signal length. Subspace-based techniques for directly solving for the channel responses have been proposed for the general BMD problem; here, under mild conditions on the channel responses and input, the unknown channel responses are determined exactly (to within a scaling constant) as the solution of a system of linear equations [42, 43]. It is of interest to apply a similar linear algebraic formulation to the SAR autofocus problem, so that the implicit multichannel relationship can be captured explicitly.

In [34], we presented initial results in applying existing subspace-based BMD techniques to the SAR autofocus problem. However, a more efficient and robust approach is to consider the *dual* problem of directly solving for a common focusing operator \mathbf{f} (i.e., the inverse of the blurring kernel \mathbf{b}), as opposed to solving for all of the channel responses $\mathbf{g}^{[n]}$, $n = 0, 1, \dots, N - 1$ [33]. To accomplish this, we explicitly characterize the multichannel condition of the SAR autofocus problem by constructing a low-dimensional subspace where the perfectly focused image resides. The subspace characterization provides a linear framework through which the focusing operator can be directly determined. To determine a unique solution, we assume that a small portion of the perfectly focused

image is zero-valued, or corresponds to a region of low return. This constrains the problem sufficiently so that the focusing operator can be obtained as the solution of a known linear system of equations; thus, the solution is determined in a noniterative fashion. We refer to this linear algebraic approach as the *MultiChannel Autofocus* (MCA) algorithm. In practice, the constraint on the underlying image may be enforced approximately by acquiring Fourier-domain data that are sufficiently oversampled in the cross-range dimension, so that the coverage of the image extends beyond the brightly illuminated portion of the scene determined by the antenna pattern [1].

Existing SAR autofocus methods implicitly have relied upon the multichannel condition to properly restore images [28]. In the MCA approach, we have systematically exploited the multichannel condition using an elegant subspace framework. While the success of existing autofocus approaches requires accurate prior assumptions about the underlying scene, such as the suitability of sharpness metrics or knowledge of point scatterers, MCA does not require prior assumptions about the scene characteristics. The MCA approach is found to be computationally efficient, and robust in the presence of noise and deviations from the image support assumption. In addition, the performance of the proposed technique does not depend on the nature of the phase error; in previous SAR autofocus techniques that do not explicitly exploit the linear structure of the problem, the performance sometimes suffers considerably when the phase errors are large and rapidly varying. MCA is simply expressed in a vector-space framework, allowing sharpness metric optimization to be easily incorporated as a regularization term, and enabling SAR autofocus to be cast into a more unified paradigm with other image restoration problems.

The organization of the chapter is as follows. Section 2 presents the SAR autofocus problem statement and establishes the notation used in this paper. In Section 3, a linear algebraic framework is derived for the problem, and the MCA image restoration procedure is formulated. An analysis of the MCA technique, and its computationally efficient implementation, are presented in Section 4. Section 5 addresses incorporation of sharpness metric optimization within the MCA restoration framework as a regulariza-

tion procedure. In Section 6, the application of MCA in practical scenarios is discussed. Section 7 presents simulation results using synthetic and actual SAR images. The performance of the proposed technique is compared with that of conventional autofocus algorithms; MCA is found to offer restoration quality on par with, or often superior to, the best existing autofocus approaches.

4.2 Problem Setup

4.2.1 Notation

We introduce vector notation for discrete signals. The column vector $\mathbf{b} \in \mathbb{C}^M$ is composed of the values of $b[m]$, $m = 0, 1, \dots, M - 1$. Column n of $g[m, n]$, representing a particular range coordinate of a SAR image, is denoted by the vector $\mathbf{g}^{[n]} \in \mathbb{C}^M$. We define $\mathbf{vec}\{\mathbf{g}\} \in \mathbb{C}^{MN}$ to be the vector composed of the concatenated columns $\mathbf{g}^{[n]}$, $n = 0, 1, \dots, N - 1$. The notation $\{\mathbf{A}\}_\Omega$ refers to the matrix formed from a subset of the rows of \mathbf{A} , where Ω is a set of row indices. Lastly, $\mathbf{C}\{\mathbf{b}\} \in \mathbb{C}^{M \times M}$ is a circulant matrix formed with the vector \mathbf{b} :

$$\mathbf{C}\{\mathbf{b}\} = \begin{bmatrix} b[0] & b[M-1] & \dots & b[1] \\ b[1] & b[0] & \dots & b[2] \\ \vdots & \vdots & \ddots & \vdots \\ b[M-1] & b[M-2] & \dots & b[0] \end{bmatrix}. \quad (4.1)$$

4.2.2 Problem description and characterization of the solution space

The aim of *SAR autofocus* is to restore the perfectly focused image \mathbf{g} given the defocused image $\tilde{\mathbf{g}}$ and assumptions about the characteristics of the underlying scene. Using (2.9) and (2.11), the defocusing relationship in the spatial-domain is expressed as

$$\tilde{\mathbf{g}} = \underbrace{\mathbf{F}^H \mathbf{D}(e^{j\phi_e}) \mathbf{F}}_{\mathbf{C}\{\mathbf{b}\}} \mathbf{g}, \quad (4.2)$$

where $\mathbf{F} \in \mathbb{C}^{M \times M}$ is the 1-D DFT unitary matrix with entries $F_{k,m} = \frac{1}{\sqrt{M}} e^{-j2\pi km/M}$, \mathbf{F}^H is the Hermitian of \mathbf{F} and represents the inverse DFT, $\mathbf{D}(e^{j\phi_e}) \in \mathbb{C}^{M \times M}$ is a diagonal matrix with the entries $e^{j\phi_e[k]}$ on the diagonal, and $\mathbf{C}\{\mathbf{b}\} \in \mathbb{C}^{M \times M}$ is a circulant matrix formed with the blurring kernel \mathbf{b} , where $b[m] = DFT_k^{-1}\{e^{j\phi_e[k]}\}$. Thus, the defocusing effect can be described as the multiplication of the perfectly focused image by a circulant matrix with eigenvalues equal to the unknown phase errors. Likewise, we define the *solution space* to be the set of all images formed from $\tilde{\mathbf{g}}$ with different ϕ :

$$\hat{\mathbf{g}}(\phi) = \underbrace{\mathbf{F}^H \mathbf{D}(e^{-j\phi}) \mathbf{F}}_{\mathbf{C}\{\mathbf{f}_A\}} \tilde{\mathbf{g}}, \quad (4.3)$$

where \mathbf{f}_A is an *all-pass* correction filter. Note that $\hat{\mathbf{g}}(\phi_e) = \mathbf{g}$.

Autofocus algorithms typically solve for the *phase error estimate* $\hat{\phi}$ directly, and apply this to the corrupt imaging data \tilde{G} to restore the image:

$$\hat{g}[m, n] = DFT_k^{-1}\{\tilde{G}[k, n] e^{-j\hat{\phi}[k]}\}. \quad (4.4)$$

Most SAR autofocus methods are iterative, evaluating some measure of quality in the spatial domain and then perturbing the estimate of the Fourier phase error function in a manner that increases the image focus. In this paper, we present a noniterative approach where a focusing operator \mathbf{f} is directly determined to restore the image; given \mathbf{f} , it is straightforward to obtain $\hat{\phi} = \phi_e$. Underlying the approach is a linear subspace characterization for the problem, which allows the focusing operator to be computed using a linear algebraic formulation. This is addressed in the next section.

4.3 MCA Restoration Framework

4.3.1 Explicit multichannel condition

Our goal is to create a *subspace* for the perfectly focused image \mathbf{g} , spanned by a basis constructed from the given defocused image $\tilde{\mathbf{g}}$. To accomplish this, we generalize the

relationship in (4.3) to include *all* correction filters $\mathbf{f} \in \mathbb{C}^M$, that is, not just the subset of allpass correction filters \mathbf{f}_A . As a result, for a given defocused image $\tilde{\mathbf{g}}$, we obtain an M -dimensional subspace where the perfectly focused image \mathbf{g} lives:

$$\hat{\mathbf{g}}(\mathbf{f}) = \mathbf{C}\{\mathbf{f}\}\tilde{\mathbf{g}}, \quad (4.5)$$

where $\hat{\mathbf{g}}(\mathbf{f})$ denotes the restoration formed by applying \mathbf{f} . This subspace characterization explicitly captures the *multichannel condition* of SAR autofocus: the assumption that each column of the image is defocused by the same blurring kernel.

To produce a basis expansion for the subspace in terms of $\tilde{\mathbf{g}}$, we select the standard basis $\{\mathbf{e}_k\}_{k=0}^{M-1}$ for \mathbb{C}^M , i.e., $\mathbf{e}_k[m] = 1$ if $m = k$ and 0 otherwise, and express the correction filter as

$$\mathbf{f} = \sum_{k=0}^{M-1} f_k \mathbf{e}_k. \quad (4.6)$$

Note that at this point we do not enforce the allpass condition; the advantage of generalizing to all $\mathbf{f} \in \mathbb{C}^M$ is to create a linear framework. Using the linearity property of circular convolution, we have

$$\mathbf{C}\{\mathbf{f}\} = \sum_{k=0}^{M-1} f_k \mathbf{C}\{\mathbf{e}_k\}.$$

From this, any image $\hat{\mathbf{g}}$ in the subspace can be expressed in terms of a basis expansion as

$$\hat{\mathbf{g}}(\mathbf{f}) = \sum_{k=0}^{M-1} f_k \varphi^{[k]}(\tilde{\mathbf{g}}), \quad (4.7)$$

where

$$\varphi^{[k]}(\tilde{\mathbf{g}}) = \mathbf{C}\{\mathbf{e}_k\}\tilde{\mathbf{g}} \quad (4.8)$$

are known basis functions (since $\tilde{\mathbf{g}}$ is given) for the M -dimensional subspace containing the unknown perfectly focused image \mathbf{g} . In matrix form, we can write (4.7) as

$$\mathbf{vec}\{\hat{\mathbf{g}}(\mathbf{f})\} = \mathbf{\Phi}(\tilde{\mathbf{g}})\mathbf{f}, \quad (4.9)$$

where

$$\mathbf{\Phi}(\tilde{\mathbf{g}}) \stackrel{\text{def}}{=} [\mathbf{vec}\{\varphi^{[0]}(\tilde{\mathbf{g}})\}, \mathbf{vec}\{\varphi^{[1]}(\tilde{\mathbf{g}})\}, \dots, \mathbf{vec}\{\varphi^{[M-1]}(\tilde{\mathbf{g}})\}] \quad (4.10)$$

is referred to as the *basis matrix*.

4.3.2 MCA direct solution approach

To formulate the MCA approach, we express the unknown perfectly focused image in terms of the basis expansion in (4.7):

$$\mathbf{vec}\{\mathbf{g}\} = \Phi(\tilde{\mathbf{g}})\mathbf{f}^*, \quad (4.11)$$

where \mathbf{f}^* is the true correction filter satisfying $\hat{\mathbf{g}}(\mathbf{f}^*) = \mathbf{g}$. Here, the matrix $\Phi(\tilde{\mathbf{g}})$ is known, but \mathbf{g} and \mathbf{f}^* are unknown. By imposing an image support constraint on the perfectly focused image \mathbf{g} , the linear system in (4.11) can be constrained sufficiently so that the unknown correction filter \mathbf{f}^* can be directly solved for. Specifically, we assume that \mathbf{g} is approximately zero-valued over a particular set of *low-return* pixels Ω :

$$g[m, n] = \begin{cases} \xi[m, n] & \text{for } m, n \in \Omega \\ g'[m, n] & \text{for } m, n \notin \Omega, \end{cases} \quad (4.12)$$

where $\xi[m, n]$ are low-return pixels ($|\xi[m, n]| \approx 0$) and $g'[m, n]$ are unknown nonzero pixels. We define $\bar{\Omega}$ to be the set of nonzero pixels (i.e., the complement of Ω), and we say that these pixels correspond to the *region of support* (ROS). In practice, the desired image support condition can be achieved by exploiting the spatially limited illumination of the antenna beam, or by using prior knowledge of low-return regions in the SAR image. We will elaborate more on the practical application of the image support assumption in Section 6.

Enforcing spatially limited constraint (4.12) directly into multichannel framework, (4.11) becomes

$$\begin{bmatrix} \boldsymbol{\xi} \\ \mathbf{vec}\{\mathbf{g}'\} \end{bmatrix} = \begin{bmatrix} \{\Phi(\tilde{\mathbf{g}})\}_{\Omega} \\ \{\Phi(\tilde{\mathbf{g}})\}_{\bar{\Omega}} \end{bmatrix} \mathbf{f}^*, \quad (4.13)$$

where $\boldsymbol{\xi} = \{\mathbf{vec}\{\mathbf{g}\}\}_{\Omega}$ is a vector of the low-return *constraints*, $\{\Phi(\tilde{\mathbf{g}})\}_{\Omega}$ are the rows of $\Phi(\tilde{\mathbf{g}})$ that correspond to the low-return constraints, and $\{\Phi(\tilde{\mathbf{g}})\}_{\bar{\Omega}}$ are the rows of $\Phi(\tilde{\mathbf{g}})$ that correspond to the unknown pixel values of \mathbf{g} within the ROS. Given that $\boldsymbol{\xi}$ has dimension $M - 1$ or greater (i.e., there are at least $M - 1$ zero constraints), when $\boldsymbol{\xi} = \mathbf{0}$

the correction filter \mathbf{f}^* can be uniquely determined to within a scaling constant by solving for \mathbf{f} in

$$\{\Phi(\tilde{\mathbf{g}})\}_{\Omega}\mathbf{f} = \mathbf{0}. \quad (4.14)$$

We denote this direct linear solution method for determining the correction filter as the *MultiChannel Autofocus* (MCA) approach, and define

$$\Phi_{\Omega}(\tilde{\mathbf{g}}) \stackrel{\text{def}}{=} \{\Phi(\tilde{\mathbf{g}})\}_{\Omega}$$

to be the *MCA matrix* formed using the constraint set Ω .

The approach assumes that $\Phi_{\Omega}(\tilde{\mathbf{g}})$ is a rank $M - 1$ matrix; in Section 4, we state the necessary conditions for which this is satisfied. The solution $\hat{\mathbf{f}}$ to (4.14) can be obtained by determining the unique vector spanning the nullspace of $\Phi_{\Omega}(\tilde{\mathbf{g}})$ as

$$\hat{\mathbf{f}} = \text{Null}(\Phi_{\Omega}(\tilde{\mathbf{g}})) = \alpha\mathbf{f}^*, \quad (4.15)$$

where α is an arbitrary complex constant. To eliminate the magnitude scaling α , we use the Fourier phase of $\hat{\mathbf{f}}$ to correct the defocused image according to (4.4):

$$\hat{\phi}[k] = -\angle\left(DFT_m\{\hat{f}[m]\}\right). \quad (4.16)$$

In other words, we enforce the allpass condition of $\hat{\mathbf{f}}$ to determine a unique solution from (4.15).

4.3.3 Restoration using the SVD

When $|\xi[m, n]| \neq 0$ in (4.12), or when the defocused image is contaminated by additive noise, the MCA matrix has full column rank. In this case, we cannot obtain $\hat{\mathbf{f}}$ as the null vector of $\Phi_{\Omega}(\tilde{\mathbf{g}})$. However, by performing the singular value decomposition (SVD) of $\Phi_{\Omega}(\tilde{\mathbf{g}})$, a unique vector that produces the minimum gain solution (in the ℓ_2 -sense) can be determined. We express the SVD as

$$\Phi_{\Omega}(\tilde{\mathbf{g}}) = \tilde{\mathbf{U}}\tilde{\Sigma}\tilde{\mathbf{V}}^H, \quad (4.17)$$

where $\tilde{\Sigma} = \text{diag}(\sigma_1, \sigma_2, \dots, \sigma_M)$ is a diagonal matrix of the singular values satisfying $\sigma_1 \geq \sigma_2 \geq \dots \geq \sigma_M \geq 0$. Since \mathbf{f} is an allpass filter we have $\|\mathbf{f}\|_2 = 1$. Although we can no longer assume the pixels in the low-return region to be exactly zero, it is reasonable to require the low-return region to have minimum energy subject to $\|\mathbf{f}\|_2 = 1$. A solution $\hat{\mathbf{f}}$ satisfying

$$\hat{\mathbf{f}} = \arg \min_{\|\mathbf{f}\|_2=1} \|\Phi_{\Omega}(\tilde{\mathbf{g}})\mathbf{f}\|_2 \quad (4.18)$$

is given by $\hat{\mathbf{f}} = \tilde{\mathbf{V}}^{[M]}$, which is the right singular vector corresponding to the smallest singular value of $\Phi_{\Omega}(\tilde{\mathbf{g}})$ [44].

4.4 Performance Analysis

4.4.1 General properties of $\Phi_{\Omega}(\tilde{\mathbf{g}})$

A key observation underlying the success of the MCA approach is that the circulant blurring matrix $\mathbf{C}\{\mathbf{b}\}$ is unitary. This result is arrived at using (4.2), where all the eigenvalues of $\mathbf{C}\{\mathbf{b}\}$ are observed to have unit magnitude, and the fact that the DFT matrix \mathbf{F} is unitary, as follows:

$$\mathbf{C}\{\mathbf{b}\}\mathbf{C}^H\{\mathbf{b}\} = \mathbf{F}^H \mathbf{D}(e^{j\phi_e}) \mathbf{F} \mathbf{F}^H \mathbf{D}(e^{-j\phi_e}) \mathbf{F} = \mathbf{I}. \quad (4.19)$$

We observe that the basis matrix $\Phi(\tilde{\mathbf{g}})$ has a special structure by rewriting (4.5) for a single column as

$$\hat{\mathbf{g}}^{[n]}(\mathbf{f}) = \mathbf{f} \otimes_M \tilde{\mathbf{g}}^{[n]} = \mathbf{C}\{\tilde{\mathbf{g}}^{[n]}\}\mathbf{f}. \quad (4.20)$$

Comparing with (4.9), where the left side of the equation is formed by stacking the column vectors $\hat{\mathbf{g}}^{[n]}(\mathbf{f})$, and using (4.20), we have

$$\Phi(\tilde{\mathbf{g}}) = \begin{bmatrix} \mathbf{C}\{\tilde{\mathbf{g}}^{[0]}\} \\ \mathbf{C}\{\tilde{\mathbf{g}}^{[1]}\} \\ \vdots \\ \mathbf{C}\{\tilde{\mathbf{g}}^{[M-1]}\} \end{bmatrix}. \quad (4.21)$$

Analogous to (4.10), we define $\Phi(\mathbf{g})$ to be the basis matrix formed by the perfectly focused image \mathbf{g} , i.e., $\Phi(\mathbf{g})$ is formed by using \mathbf{g} instead of $\tilde{\mathbf{g}}$ in (4.10). Likewise, $\Phi_\Omega(\mathbf{g}) = \{\Phi(\mathbf{g})\}_\Omega$ is the MCA matrix formed from the perfectly focused image. From the unitary property of $\mathbf{C}\{\mathbf{b}\}$, we establish the following result.

Proposition 1 (Equivalence of singular values) *Suppose that $\tilde{\mathbf{g}} = \mathbf{C}\{\mathbf{b}\}\mathbf{g}$. Then, $\Phi_\Omega(\tilde{\mathbf{g}}) = \Phi_\Omega(\mathbf{g})\mathbf{C}\{\mathbf{b}\}$ and the singular values of $\Phi_\Omega(\mathbf{g})$ and $\Phi_\Omega(\tilde{\mathbf{g}})$ are identical.*

Proof: From the assumption, $\tilde{\mathbf{g}}^{[n]} = \mathbf{b} \otimes_M \mathbf{g}^{[n]}$. Therefore, $\mathbf{C}\{\tilde{\mathbf{g}}^{[n]}\} = \mathbf{C}\{\mathbf{g}^{[n]}\}\mathbf{C}\{\mathbf{b}\}$, and from (4.21)

$$\Phi(\tilde{\mathbf{g}}) = \begin{bmatrix} \mathbf{C}\{\mathbf{g}^{[0]}\}\mathbf{C}\{\mathbf{b}\} \\ \mathbf{C}\{\mathbf{g}^{[1]}\}\mathbf{C}\{\mathbf{b}\} \\ \vdots \\ \mathbf{C}\{\mathbf{g}^{[M-1]}\}\mathbf{C}\{\mathbf{b}\} \end{bmatrix} = \Phi(\mathbf{g})\mathbf{C}\{\mathbf{b}\}. \quad (4.22)$$

Note that (4.22) implies that $\{\Phi(\tilde{\mathbf{g}})\}_\Omega = \{\Phi(\mathbf{g})\}_\Omega\mathbf{C}\{\mathbf{b}\}$. As a result,

$$\Phi_\Omega(\tilde{\mathbf{g}})\Phi_\Omega^H(\tilde{\mathbf{g}}) = \Phi_\Omega(\mathbf{g})\mathbf{C}\{\mathbf{b}\}\mathbf{C}^H\{\mathbf{b}\}\Phi_\Omega^H(\mathbf{g}) = \Phi_\Omega(\mathbf{g})\Phi_\Omega^H(\mathbf{g}),$$

and thus $\Phi_\Omega(\mathbf{g})$ and $\Phi_\Omega(\tilde{\mathbf{g}})$ have the same singular values. \square

Thus, from Proposition 1, we can write the SVD of the MCA matrices for \mathbf{g} and $\tilde{\mathbf{g}}$ as $\Phi_\Omega(\mathbf{g}) = \mathbf{U}\Sigma\mathbf{V}^H$ and $\Phi_\Omega(\tilde{\mathbf{g}}) = \tilde{\mathbf{U}}\Sigma\tilde{\mathbf{V}}^H$, respectively. The following result demonstrates that the MCA restoration obtained through $\Phi_\Omega(\tilde{\mathbf{g}})$ and $\tilde{\mathbf{g}}$ is the same as the restoration obtained using $\Phi_\Omega(\mathbf{g})$ and \mathbf{g} .

Proposition 2 (Equivalence of restorations) *Suppose that $\Phi_\Omega(\mathbf{g})$ (or equivalently $\Phi_\Omega(\tilde{\mathbf{g}})$) has a distinct smallest singular value. Then applying the MCA correction filters $\mathbf{V}^{[M]}$ and $\tilde{\mathbf{V}}^{[M]}$ to \mathbf{g} and $\tilde{\mathbf{g}}$, respectively, produces the same restoration in absolute values; i.e.,*

$$\left| \mathbf{C}\{\tilde{\mathbf{V}}^{[M]}\}\tilde{\mathbf{g}} \right| = \left| \mathbf{C}\{\mathbf{V}^{[M]}\}\mathbf{g} \right|. \quad (4.23)$$

Proof: Expressing $\Phi_{\Omega}(\tilde{\mathbf{g}}) = \Phi_{\Omega}(\mathbf{g})\mathbf{C}\{\mathbf{b}\}$ in terms of the SVD of $\Phi_{\Omega}(\mathbf{g})$ and $\Phi_{\Omega}(\tilde{\mathbf{g}})$, we have

$$\Phi_{\Omega}(\tilde{\mathbf{g}}) = \tilde{\mathbf{U}}\Sigma\tilde{\mathbf{V}}^H = \mathbf{U}\Sigma\mathbf{V}^H\mathbf{C}\{\mathbf{b}\}. \quad (4.24)$$

Because of the assumption in the proposition, the right singular vector corresponding to the smallest singular value of $\Phi_{\Omega}(\tilde{\mathbf{g}})$ is uniquely determined to within a constant scalar factor β of absolute value one [44]:

$$\tilde{\mathbf{V}}^{[M]H} = \beta\mathbf{V}^{[M]H}\mathbf{C}\{\mathbf{b}\}, \quad (4.25)$$

where $|\beta| = 1$. Taking the transpose of both sides of (4.25) produces $\tilde{\mathbf{V}}^{[M]} = \beta\mathbf{C}^H\{\mathbf{b}\}\mathbf{V}^{[M]}$. Using the unitary property of $\mathbf{C}\{\mathbf{b}\}$,

$$\mathbf{V}^{[M]} = \beta^{-1}\mathbf{C}\{\mathbf{b}\}\tilde{\mathbf{V}}^{[M]}. \quad (4.26)$$

We then have

$$\begin{aligned} \mathbf{C}\{\mathbf{V}^{[M]}\}\mathbf{g} &= \beta^{-1}\mathbf{C}\{\mathbf{b}\}\mathbf{C}\{\tilde{\mathbf{V}}^{[M]}\}\mathbf{g} \\ &= \beta^{-1}\mathbf{C}\{\tilde{\mathbf{V}}^{[M]}\}\mathbf{C}\{\mathbf{b}\}\mathbf{g} \\ &= \beta^{-1}\mathbf{C}\{\tilde{\mathbf{V}}^{[M]}\}\tilde{\mathbf{g}}, \end{aligned}$$

and thus $\mathbf{C}\{\mathbf{V}^{[M]}\}\mathbf{g}$ and $\mathbf{C}\{\tilde{\mathbf{V}}^{[M]}\}\tilde{\mathbf{g}}$ have the same absolute value since $|\beta^{-1}| = 1$. \square

Proposition 2 is useful for two reasons. First, it demonstrates that applying MCA to the perfectly focused image or any defocused image described by (4.2) produces the same restored image (in SAR, we are only interested in displaying the image magnitude). In other words, the restoration formed using the MCA approach does not depend on the phase error function; the MCA restoration depends only on \mathbf{g} and the selection of low-return constraints Ω (i.e., the pixels in \mathbf{g} we are assuming to be low-return). This finding is significant because existing autofocus techniques tend to perform less well when the phase errors are large and rapidly varying [1, 16]. We note that while the MCA restoration is the same under any phase error function, this result does not imply anything about the quality of the restoration. Second, Proposition 2 shows that it is sufficient to examine the perfectly focused image to determine the conditions under which unique restorations are possible using MCA.

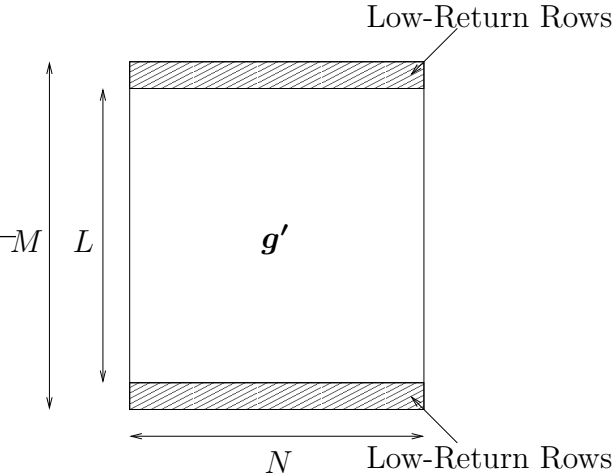


Figure 4.2 Illustration of the spatially limited image support assumption in the special case where there are low-return rows in the perfectly focused image.

4.4.2 Special case: Low-return rows

A case of particular interest is where Ω corresponds to a set of low-return rows. The consideration of row constraints matches a practical case of interest where the attenuation due to the antenna pattern is used to satisfy the low-return pixel assumption (this is addressed in Section 6). In this case, $\Phi_{\Omega}(\mathbf{g})$ has a special structure that can be exploited for efficient computation. This form also allows the necessary conditions for a unique correction filter to be precisely determined.

Figure 4.2 shows an illustration of the special case, where there are L rows within the ROS, and the top and bottom rows are low-return. We define the set $\mathcal{L} = \{l_1, l_2, \dots, l_R\}$ to be the set of low-return row indices, where $R = M - L$ is the number of low-return rows and $0 \leq l_j \leq M - 1$, such that

$$g[m, n] = \begin{cases} \xi[m, n] & \text{for } m \in \mathcal{L} \\ g'[m, n] & \text{for } m \notin \mathcal{L}. \end{cases} \quad (4.27)$$

To explicitly construct the MCA matrix in this case, we first use (4.5) to express

$$\mathbf{g}^T = \tilde{\mathbf{g}}^T \mathbf{C}^T \{\mathbf{f}^*\}, \quad (4.28)$$

where T denotes transpose. We consider the transposed images because this allows us to represent the low-return rows in \mathbf{g} as column vectors, which leads to an expression of

the form (4.14) where $\Phi_\Omega(\tilde{\mathbf{g}})$ is explicitly defined. Note that

$$\mathbf{C}^T\{\mathbf{f}\} = [\mathbf{f}_F, \mathbf{C}\{\mathbf{e}_1\}\mathbf{f}_F, \dots, \mathbf{C}\{\mathbf{e}_{M-1}\}\mathbf{f}_F], \quad (4.29)$$

where $\mathbf{C}\{\mathbf{e}_l\}$ is the l -component circulant shift matrix, and

$$f_F[m] = f[\langle -m \rangle_M], \quad (4.30)$$

$m = 0, 1, \dots, M - 1$, is a flipped version of the true correction filter ($\langle n \rangle_M$ denotes n modulo M). Using (4.28) and (4.29), we express the l -th row of \mathbf{g} as

$$(\mathbf{g}^T)^{[l]} = \tilde{\mathbf{g}}^T \mathbf{C}\{\mathbf{e}_l\} \mathbf{f}_F^*. \quad (4.31)$$

Note that multiplication with the matrix $\mathbf{C}\{\mathbf{e}_l\}$ in the expression above results in an l -component left circulant shift along each row of $\tilde{\mathbf{g}}^T$.

The relationship in (4.31) is informative because it shows how the MCA matrix $\Phi_\Omega(\tilde{\mathbf{g}})$ can be constructed given the image support constraint in (4.27). For the low-return rows satisfying $(\mathbf{g}^T)^{[l_j]} \approx \mathbf{0}$, we have the relation

$$(\mathbf{g}^T)^{[l_j]} = \tilde{\mathbf{g}}^T \mathbf{C}\{\mathbf{e}_{l_j}\} \mathbf{f}_F^* \approx 0 \quad (4.32)$$

for $j = 1, 2, \dots, R$. Enforcing (4.32) for all of the low-return rows simultaneously produces

$$\mathbf{0} \approx \underbrace{\begin{bmatrix} \tilde{\mathbf{g}}^T \mathbf{C}\{\mathbf{e}_{l_1}\} \\ \tilde{\mathbf{g}}^T \mathbf{C}\{\mathbf{e}_{l_2}\} \\ \vdots \\ \tilde{\mathbf{g}}^T \mathbf{C}\{\mathbf{e}_{l_R}\} \end{bmatrix}}_{\Phi_{\mathcal{L}}(\tilde{\mathbf{g}})} \mathbf{f}_F^*, \quad (4.33)$$

where (with abuse of notation) $\Phi_{\mathcal{L}}(\tilde{\mathbf{g}}) \in \mathbb{C}^{NR \times M}$ is the MCA matrix for the row constraint set \mathcal{L} . In this special case, $\Phi_{\mathcal{L}}$ plays the same role as Φ_Ω for the general case. Thus, we see that in this case the MCA matrix is formed by stacking shifted versions of the transposed defocused image, where the shifts correspond to the locations of the low-return rows in the perfectly focused image. Determining the null vector (or minimum

right singular vector) of $\Phi_{\mathcal{L}}(\tilde{\mathbf{g}})$ as defined in (4.33) produces a flipped version of the correction filter; the correction filter \mathbf{f} can be obtained by appropriately shifting the elements of \mathbf{f}_F according to (4.30). The reason for considering the flipped form in (4.33) is that it provides a special structure for efficiently computing \mathbf{f} , as we will demonstrate in the next subsection.

To determine necessary conditions for a unique and correct solution of the MCA equation (4.14), we restrict our analysis to the model in (4.27) where the low-return rows are identically zero: $\xi[m, n] = 0$. From Propositions 1 and 2, the conditions for a unique solution to (4.14) can be determined using $\Phi_{\mathcal{L}}(\mathbf{g})$ in place of $\Phi_{\mathcal{L}}(\tilde{\mathbf{g}})$. This in turn is equivalent to requiring $\Phi_{\mathcal{L}}(\mathbf{g})$ to be a rank $M - 1$ matrix.

Proposition 3 (Necessary condition for unique and correct solution) *Consider the image model $g[m, n] = 0$ for $m \in \mathcal{L}$ and $g[m, n] = g'[m, n]$ for $m \notin \mathcal{L}$. Then a necessary condition for MCA to produce a unique and correct solution to the autofocus problem is*

$$\text{rank}(\mathbf{g}') \geq \frac{M - 1}{R}. \quad (4.34)$$

Proof: First notice that

$$\begin{aligned} \text{rank}(\tilde{\mathbf{g}}^T \mathbf{C}\{\mathbf{e}_{l_j}\}) &= \text{rank}(\tilde{\mathbf{g}}) = \text{rank}(\mathbf{C}\{\mathbf{b}\}\mathbf{g}) \\ &= \text{rank}(\mathbf{g}) = \text{rank}(\mathbf{g}'), \end{aligned}$$

because $\mathbf{C}\{\mathbf{e}_{l_j}\}$ and $\mathbf{C}\{\mathbf{b}\}$ are unitary matrices, and the zero-row assumption of the image \mathbf{g} . Then from (4.33) we have

$$\text{rank}(\Phi_{\mathcal{L}}(\tilde{\mathbf{g}})) \leq R \text{rank}(\mathbf{g}').$$

Therefore, a necessary condition for $\text{rank}(\Phi_{\mathcal{L}}(\tilde{\mathbf{g}})) = M - 1$ is $\text{rank}(\mathbf{g}') \geq (M - 1)/R$. Furthermore, notice that the filter $\mathbf{f}_{Id} \stackrel{\text{def}}{=} [1, 0, \dots, 0]^T$ is always a solution to (4.14) for \mathbf{g} as defined in the proposition statement: $\Phi_{\mathcal{L}}(\mathbf{g})\mathbf{f}_{Id} = \mathbf{0}$. This is because applying \mathbf{f}_{Id} to \mathbf{g} returns the same image \mathbf{g} , where all the pixels in the low-return region are zero

by assumption. Thus, the unique solution for (4.14) is also the correct solution to the autofocus problem. \square

Noting that $M = R + L$, and using condition (4.34), we derive the minimum number of zero-return rows R required to achieve a unique solution as a function of the rank of \mathbf{g}' :

$$R \geq \frac{L - 1}{\text{rank}(\mathbf{g}') - 1}. \quad (4.35)$$

The condition $\text{rank}(\mathbf{g}') = \min(L, N)$ usually holds, with the exception of degenerate cases where the rows or columns of \mathbf{g}' are linearly dependent. Since $\text{rank}(\mathbf{g}') \leq \min(L, N)$, (4.35) implies

$$R \geq \frac{L - 1}{\min(L, N) - 1}. \quad (4.36)$$

The condition in (4.36) provides a rule for determining the minimum R (the minimum number of low-return rows required) as a function of the dimensions of the ROS in the general case where $\xi[n, m] \neq 0$.

4.4.3 Efficient restoration procedure

Forming the MCA matrix according to (4.33) and performing its full SVD can be computationally expensive in terms of both memory and CPU time when there are many low-return rows, since the dimensions of $\Phi_{\mathcal{L}}(\tilde{\mathbf{g}})$ are NR rows by M columns. As an example, for a 1000×1000 pixel image with 100 low-return rows, $\Phi_{\mathcal{L}}(\tilde{\mathbf{g}})$ is a $100\,000 \times 1000$ matrix; in this case, it is not practical to construct and invert such a large matrix.

Due to the structure of $\Phi_{\mathcal{L}}(\tilde{\mathbf{g}})$, it is possible to efficiently compute the minimum right singular vector solution in (4.18). Note that the right singular vectors of $\Phi_{\mathcal{L}}(\tilde{\mathbf{g}})$ can be determined by solving for the eigenvectors of

$$\mathbf{B}_{\mathcal{L}}(\tilde{\mathbf{g}}) = \Phi_{\mathcal{L}}^H(\tilde{\mathbf{g}})\Phi_{\mathcal{L}}(\tilde{\mathbf{g}}). \quad (4.37)$$

Without exploiting the structure of the MCA matrix, forming $\mathbf{B}_{\mathcal{L}}(\tilde{\mathbf{g}}) \in \mathbb{C}^{M \times M}$ and computing its eigenvectors requires $O(NRM^2)$ operations. Using (4.33), the matrix

product (4.37) can be expressed as

$$\mathbf{B}_{\mathcal{L}}(\tilde{\mathbf{g}}) = \sum_{j=1}^R \mathbf{C}^T\{\mathbf{e}_{l_j}\} \tilde{\mathbf{g}}^* \tilde{\mathbf{g}}^T \mathbf{C}\{\mathbf{e}_{l_j}\}, \quad (4.38)$$

where $\tilde{\mathbf{g}}^* = (\tilde{\mathbf{g}}^T)^H$ (i.e., all of the entries of $\tilde{\mathbf{g}}$ are conjugated). Let $\mathbf{H}(\tilde{\mathbf{g}}) \stackrel{\text{def}}{=} \tilde{\mathbf{g}}^* \tilde{\mathbf{g}}^T$. The effect of $\mathbf{C}^T\{\mathbf{e}_{l_j}\}$ in (4.38) is to circularly shift $\mathbf{H}(\tilde{\mathbf{g}})$ up by l_j pixels along each column, while $\mathbf{C}\{\mathbf{e}_{l_j}\}$ circularly shifts $\mathbf{H}(\tilde{\mathbf{g}})$ to the left by l_j pixels along each row. Thus, $\mathbf{H}(\tilde{\mathbf{g}})$ can be computed once initially, and then $\mathbf{B}_{\mathcal{L}}(\tilde{\mathbf{g}})$ can be formed by adding shifted versions of $\mathbf{H}(\tilde{\mathbf{g}})$, which requires only $O(NM^2)$ operations. Thus, the computation has been reduced by a factor of R . In addition, the memory requirements have also been reduced by R times (assuming $M \approx N$), since only $\mathbf{H}(\tilde{\mathbf{g}}) \in \mathbb{C}^{M \times M}$ needs to be stored, as opposed to $\Phi_{\mathcal{L}}^H(\tilde{\mathbf{g}}) \in \mathbb{C}^{NR \times M}$. As a result, the total cost of constructing $\mathbf{B}_{\mathcal{L}}(\tilde{\mathbf{g}})$ and performing its eigendecomposition is $O(NM^2)$ (when $M \leq N$).

4.5 Application of Sharpness Metric Optimization to MCA

4.5.1 Bringing metrics to the MCA framework

The vector-space framework of the MCA approach allows sharpness metric optimization to be incorporated as a regularization procedure. The use of sharpness metrics can improve the solution when multiple singular values of $\Phi_{\Omega}(\tilde{\mathbf{g}})$ are close to zero. Such a condition can occur if the perfectly focused SAR image is very sparse (effectively low rank). In addition, metric optimization is beneficial in cases where the low-return assumption $|\xi[m, n]| \approx 0$ holds weakly, or where additive noise with large variance is present. In these nonideal scenarios, we show how the MCA framework provides an approximate reduced-dimension solution subspace, where the optimization may be performed over a small set of parameters.

Suppose that instead of knowing that the image pixels in the low-return region are exactly zero, we can assume only that

$$\|\{\mathbf{vec}\{\mathbf{g}\}\}_\Omega\|_2^2 \leq c \quad (4.39)$$

for some specific constant c . Then, the MCA condition becomes

$$\|\Phi_\Omega(\tilde{\mathbf{g}})\mathbf{f}\|_2^2 \leq c\|\mathbf{f}\|_2^2. \quad (4.40)$$

Note that the true correction filter \mathbf{f}^* must satisfy (4.40).

The goal of using sharpness optimization is to determine the best \mathbf{f} (in the sense of producing an image with maximum sharpness) satisfying (4.40). We now derive a reduced-dimension subspace for performing the optimization where (4.40) holds for all \mathbf{f} in the subspace. To accomplish this, we first determine σ_{M-K+1} , which we define as the largest singular value of $\Phi_\Omega(\tilde{\mathbf{g}})$ satisfying $\sigma_k^2 \leq c$. Then we express \mathbf{f} in terms of the basis formed from the right singular vectors of $\Phi_\Omega(\tilde{\mathbf{g}})$ corresponding to the K smallest singular values, i.e.,

$$\mathbf{f} = \sum_{k=M-K+1}^M v_k \tilde{\mathbf{V}}^{[k]}, \quad (4.41)$$

where v_k is a basis coefficient corresponding to the basis vector $\tilde{\mathbf{V}}^{[k]}$. To demonstrate that every element of the K -dimensional subspace in (4.41) satisfies (4.40), we define $S_K^* = \text{span}\{\tilde{\mathbf{V}}^{[M-K+1]}, \tilde{\mathbf{V}}^{[M-K+2]}, \dots, \tilde{\mathbf{V}}^{[M]}\}$, and note that [45]

$$\begin{aligned} \max_{\substack{\|\mathbf{f}\|_2=1 \\ \mathbf{f} \in S_K^*}} \|\Phi_\Omega(\tilde{\mathbf{g}})\mathbf{f}\|_2^2 &= \max_{\substack{\|\mathbf{f}\|_2=1 \\ \mathbf{f} \in S_K^*}} \|\tilde{\mathbf{U}}\Sigma\tilde{\mathbf{V}}^H\mathbf{f}\|_2^2 \\ &= \max_{\substack{\|\mathbf{v}\|_2=1 \\ v_1=v_2=\dots=v_{M-K}=0}} \|\Sigma\mathbf{v}\|_2^2 \\ &= \max_{\|\mathbf{v}\|_2=1} \sum_{k=M-K+1}^M \sigma_k^2 |v_k|^2 = \sigma_{M-K+1}^2 \leq c, \end{aligned} \quad (4.42)$$

where $\mathbf{v} \stackrel{\text{def}}{=} \tilde{\mathbf{V}}^H \mathbf{f}$. In the second equality, the unitary property of $\tilde{\mathbf{V}}$ is used to obtain $\|\mathbf{f}\|_2 = \|\mathbf{v}\|_2$, and also $\mathbf{f} = \tilde{\mathbf{V}}\mathbf{v}$, from which it is observed that $\mathbf{f} \in S_K^*$ implies $v_1 = v_2 = \dots = v_{M-K} = 0$. We note that the subspace S_K^* does not contain all \mathbf{f} satisfying (4.40).

However, it provides an optimal K -dimensional subspace in the following sense: for any subspace S_K where $\dim(S_K) = K$, we have [44]

$$\max_{\substack{\|\mathbf{f}\|_2=1 \\ \mathbf{f} \in S_K}} \|\Phi_\Omega(\tilde{\mathbf{g}})\mathbf{f}\|_2^2 \geq \max_{\substack{\|\mathbf{f}\|_2=1 \\ \mathbf{f} \in S_K^*}} \|\Phi_\Omega(\tilde{\mathbf{g}})\mathbf{f}\|_2^2 = \sigma_{M-K+1}^2. \quad (4.43)$$

Thus, S_K^* is the best K -dimensional subspace in the sense that every element is feasible (i.e., satisfies (4.40)), and among all K -dimensional subspaces S_K^* minimizes the maximum energy in the low-return region.

Substituting the basis expansion (4.41) for \mathbf{f} into (4.5) allows \mathbf{g} to be expressed in terms of an approximate reduced-dimension basis:

$$\mathbf{g}_d = \sum_{k=1}^K d_k \boldsymbol{\psi}^{[k]}, \quad (4.44)$$

where

$$\boldsymbol{\psi}^{[k]} = \mathbf{C}\{\tilde{\mathbf{V}}^{[M-K+k]}\}\tilde{\mathbf{g}}, \quad (4.45)$$

$d_k = v_{M-K+k}$, and \mathbf{g}_d is the image parameterized by the basis coefficients $\mathbf{d} = [d_1, d_2, \dots, d_K]^T$. To obtain the best $\hat{\mathbf{g}}$ that satisfies the data consistency condition, we optimize a particular sharpness metric over the coefficients \mathbf{d} , where the number of coefficients $K \ll M$.

4.5.2 Performing the metric optimization

We define the metric objective function $\mathcal{C} : \mathbb{C}^K \rightarrow \mathbb{R}$ as the mapping from the basis coefficients $\mathbf{d} = [d_1, d_2, \dots, d_K]^T$ to a sharpness cost

$$\mathcal{C}(\mathbf{d}) = \sum_{m=0}^{M-1} \sum_{n=0}^{N-1} S(\bar{I}_d[m, n]), \quad (4.46)$$

where $I_d[m, n] = |g_d[m, n]|^2$ is the intensity of each pixel, $\bar{I}_d[m, n] = I_d[m, n]/\gamma_{g_d}$ is the normalized intensity with $\gamma_{g_d} = \|\mathbf{g}_d\|_2^2$, and $S : \mathbb{R}^+ \rightarrow \mathbb{R}$ is an image sharpness metric operating on the normalized intensity of each pixel. An example of a commonly used sharpness metric in SAR is the image entropy: $S_H(\bar{I}_d[m, n]) \stackrel{\text{def}}{=} -\bar{I}_d[m, n] \ln \bar{I}_d[m, n]$

[15, 18]. A gradient-based search can be used to determine a local minimizer of $\mathcal{C}(\mathbf{d})$ [32]. The k -th element of the gradient $\nabla_{\mathbf{d}}\mathcal{C}(\mathbf{d})$ is determined using

$$\frac{\partial \mathcal{C}(\mathbf{d})}{\partial d_k} = \sum_{m,n} \frac{\partial S(\bar{I}_{\mathbf{d}}[m, n])}{\partial \bar{I}_{\mathbf{d}}[m, n]} \left(\frac{2}{\gamma_{\mathbf{g}_{\mathbf{d}}}} g_{\mathbf{d}}[m, n] \psi^{*[k]}[m, n] - \frac{2}{\gamma_{\mathbf{g}_{\mathbf{d}}}^2} I_{\mathbf{d}}[m, n] \sum_{m', n'} g_{\mathbf{d}}[m', n'] \psi^{*[k]}[m', n'] \right), \quad (4.47)$$

where $*$ denotes the complex conjugate. Note that (4.47) can be applied to a variety of sharpness metrics. Considering the entropy example, the derivative of the sharpness metric is $\partial S_H(\bar{I}_{\mathbf{d}}[m, n]) / \partial \bar{I}_{\mathbf{d}}[m, n] = -(1 + \ln \bar{I}_{\mathbf{d}}[m, n])$.

4.6 SAR Data Acquisition and Processing

In this section, we discuss the application of the MCA technique in practical scenarios. One way of satisfying the image support assumption used in MCA is to exploit the SAR antenna pattern. In spotlight-mode SAR, the area of terrain that can be imaged depends on the *antenna footprint*, i.e., the illuminated portion of the scene corresponding to the projection of the antenna main-beam onto the ground plane [1]. There is low return from features outside of the antenna footprint. The fact the SAR image is essentially spatially limited, due to the profile of the antenna beam pattern, suggests that the proposed autofocus technique can be applied in spotlight-mode SAR imaging given that the SAR data are sampled at a sufficiently high rate [1–3].

The amount of area represented in a SAR image, the image *field of view* (FOV), is determined by how densely the analog Fourier transform is sampled. As the density of the sampling is increased, the FOV of the image increases. For a spatially-limited scene, there is a critical sampling density at which the image coverage is equal to the support of the scene (determined by the width of the antenna footprint). If the Fourier transform is sampled above the critical rate, the FOV of the image extends beyond the finite support of the scene, and the result resembles a zero-padded or zero-extended image. Our goal is to select the Fourier domain sampling density such that the FOV of the SAR image

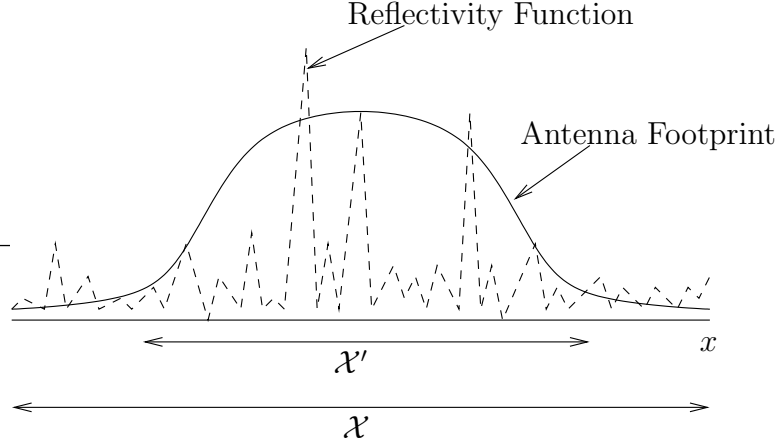


Figure 4.3 The antenna pattern shown superimposed on the scene reflectivity function for a single range (y) coordinate. The finite beamwidth of the antenna causes the terrain to be illuminated only within a spatially limited window; the return outside the window is near zero.

extends beyond the brightly illuminated portion of the scene. In doing so, we cause the perfectly focused digital image to be (effectively) spatially limited, allowing the use of the proposed autofocus approach.

Figure 4.3 shows an illustration of the antenna pattern along the x -axis. A length \mathcal{X}' region of the scene is brightly illuminated in the x dimension. To use the MCA approach to autofocus, we need the image coverage \mathcal{X} to be greater than the illuminated region \mathcal{X}' . To model the antenna pattern, we consider the case of an unweighted, uniformly radiating antenna aperture. Under this scenario, both the transmit and receive patterns are described by a sinc function [46–48]. Thus, the antenna footprint determined by the combined transmit-receive pattern is modeled as [1, 46]

$$w(x) = \text{sinc}^2(W_x^{-1}x), \quad (4.48)$$

where

$$W_x = \frac{\lambda_0 R_0}{D}, \quad (4.49)$$

$\text{sinc}(x) \stackrel{\text{def}}{=} (\sin \pi x)/(\pi x)$, x is the cross-range coordinate, λ_0 is the wavelength of the radar, R_0 is the range from the radar platform to the center of the scene, and D is the length of the antenna aperture. Near the nulls of the antenna pattern at $x = \pm W_x$, the

attenuation will be very large, producing low-return rows in the perfectly focused SAR image consistent with (4.27).

Using the model in (4.48), the Fourier-domain sampling density should be large enough so that the FOV of the SAR image is equal to or greater than the width of the mainlobe of the sinc window: $\mathcal{X} \geq 2W_x$. In spotlight-mode SAR, the Fourier-domain sampling density in the cross-range dimension is determined by the pulse repetition frequency (PRF) of the radar. For a radar platform moving with constant velocity, increasing the PRF decreases the angular interval between pulses (i.e., the angular increment between successive look angles), thus increasing the cross-range Fourier-domain sampling density and FOV [1,2]. Alternatively, keeping the PRF constant and decreasing the platform velocity also increases the cross-range Fourier-domain sampling density; such is the case in airborne SAR when the aircraft is flying into a headwind. In many cases, the platform velocity and PRF are such that the image FOV is approximately equal to the mainlobe width of (4.48); in these cases, the final images are usually cropped to half the mainlobe width of the sinc window [1], because it is realized that the edge of the processed image will suffer from some amount of aliasing. Our framework suggests that the additional information from the discarded portions of the image can be used for SAR image autofocus.

Another instance where the image support assumption can be exploited is when prior knowledge of low-return features in the SAR image is available. Examples of such features include smooth bodies of water, roads, and shadowy regions [15]. If the image defocusing is not very severe, then low-return regions can be estimated using the defocused image. Inverse SAR (ISAR) provides a further application for MCA. In ISAR images, pixels outside of the support of the imaged object (e.g., aircraft, satellites) correspond to a region of *zero* return [15]. Thus, given an estimate of the object support, MCA can be applied.

4.7 Experimental Results

Figure 4.4 presents an experiment using an actual SAR image.¹ To form a ground truth, perfectly focused image, an entropy-minimization autofocus routine [18] was applied to the given SAR image. Figure 4.4(a) shows the resulting image, where the sinc-squared window in Figure 4.4(b) has been applied to each column to simulate the antenna footprint resulting from an unweighted antenna aperture. The cross-range FOV equals 95% of the mainlobe width of the squared-sinc function; i.e., the image is cropped within the nulls of the antenna footprint, so that there is very large (but not infinite) attenuation at the edges of the image. Figure 4.4(c) shows a defocused image produced by applying a white phase error function (i.e., independent phase components uniformly distributed between $-\pi$ and π) to the perfectly focused image in Figure 4.4(a). We applied MCA to the defocused image assuming the top and bottom rows of the perfectly focused image to be low-return. The MCA restoration is displayed in Figure 4.4(d). The restored image is observed to be in good agreement with the ground truth image. To quantitatively assess the performance of autofocus techniques, we use the restoration quality metric SNR_{out} (i.e., *output signal-to-noise ratio*), which is defined as [49]

$$\text{SNR}_{out} = 20 \log_{10} \frac{\|\mathbf{vec}\{\mathbf{g}\}\|_2}{\|(|\mathbf{vec}\{\mathbf{g}\}| - |\mathbf{vec}\{\hat{\mathbf{g}}\}|)\|_2};$$

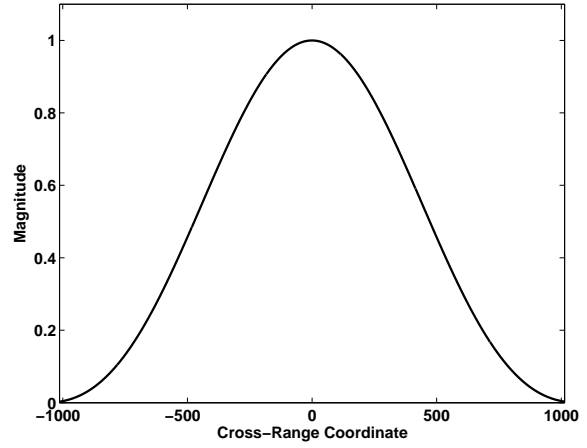
here, the “noise” in SNR_{out} refers to the error in the magnitude of the reconstructed image $\hat{\mathbf{g}}$ relative to the perfectly focused image \mathbf{g} , and should not be confused with additive noise (which is considered later). For the restoration in Figure 4.4(d), $\text{SNR}_{out} = 10.52$ dB.

To evaluate the robustness of MCA with respect to the low-return assumption, we performed a series of experiments using the idealized window function in Figure 4.5(a). The window has a flat response over most of the image; the tapering at the edges of the window is described by a quarter-period of a sine function. In each experiment, the *gain* at the edges of the window (i.e., the inverse of the attenuation) is increased such that the pixel magnitudes in the low-return region (corresponding to the top and bottom rows)

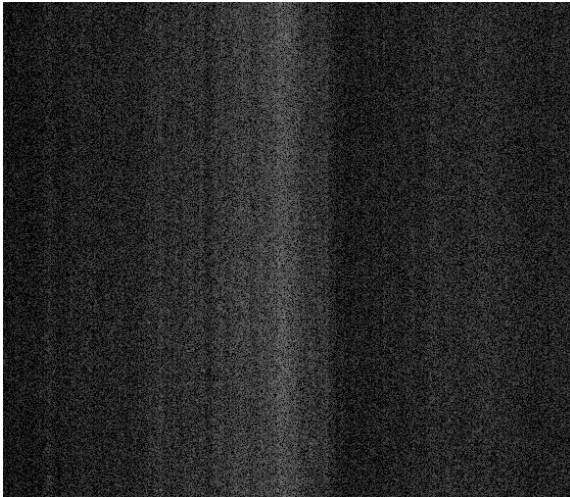
¹The actual SAR image was provided by Dr. Charles Jakowatz of Sandia National Laboratories.



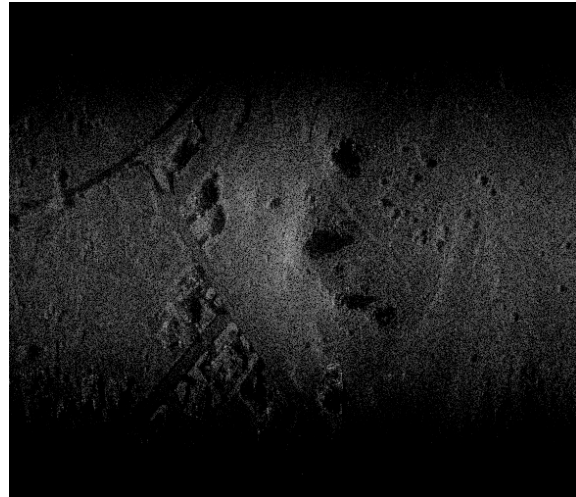
(a)



(b)



(c)



(d)

Figure 4.4 Actual 2335×2027 pixel SAR image: (a) perfectly focused image, where the simulated sinc-squared antenna footprint in (b) has been applied to each column, (c) defocused image produced by applying a white phase error function, and (d) MCA restoration ($\text{SNR}_{out} = 10.52$ dB).

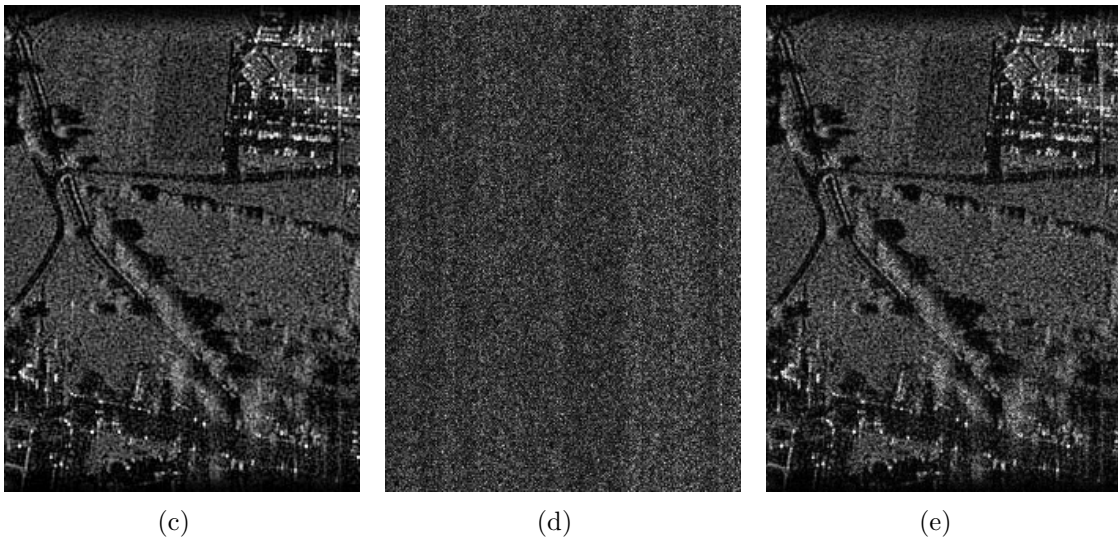
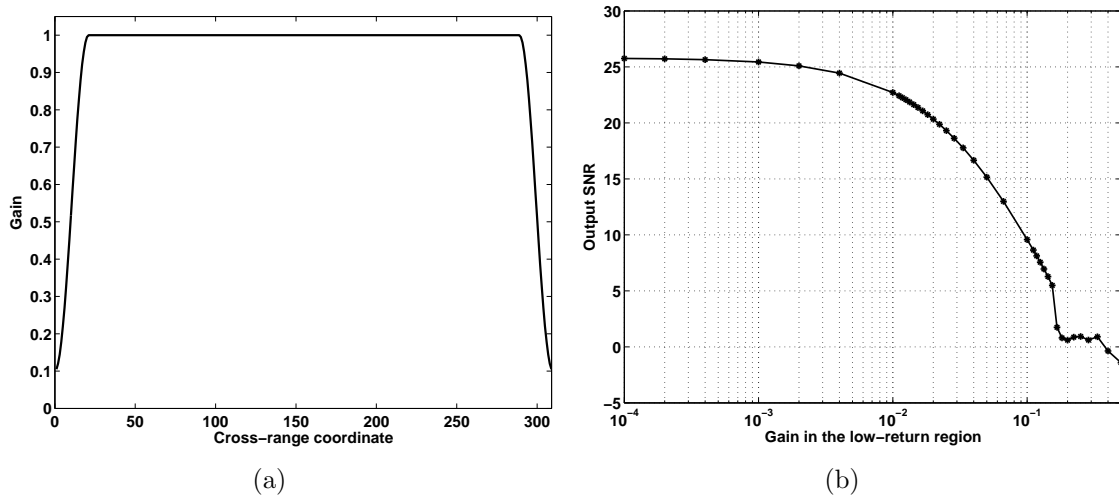


Figure 4.5 Experiments evaluating the robustness of MCA as a function of the attenuation in the low-return region: (a) window function applied to each column of the SAR image, where the gain at the edges of the window (corresponding to the low-return region) is varied with each experiment (a gain of 0.1 is shown); (b) plot of the quality metric SNR_{out} for the MCA restoration (measured with respect to the perfectly focused image) versus the window gain in the low-return region; (c) simulated perfectly focused 309×226 pixel image, where the window in (a) has been applied; (d) defocused image produced by applying a white phase error function; and (e) MCA restoration ($\text{SNR}_{out} = 9.583$ dB).

become larger. In Figure 4.5(a), a window gain of 0.1 is shown. For each value of the window gain, a defocused image is formed and the MCA restoration is produced.

Figure 4.5(b) shows a plot of the restoration quality metric SNR_{out} versus the gain at the edges of the window, where the top two rows and bottom two rows are assumed to be low-return. The simulated SAR image in Figure 4.5(c) was used as the ground truth, perfectly focused image in this set of experiments; here, a processed SAR image² is used as a model for the image magnitude, while the phase of each pixel is selected at random (uniformly distributed between $-\pi$ and π and uncorrelated) to simulate the complex reflectivity associated with high frequency SAR images of terrain [36]. The plot in Figure 4.5(b) demonstrates that the restoration quality decreases monotonically as a function of increasing window gain. We observe that for values of SNR_{out} less than 3 dB, the restored images do not resemble the perfectly focused image; this transition occurs when gain in the low-return region increases above 0.14. For gain values less than or equal to 0.14, the restorations are faithful representations of the perfectly focused image. Thus, we see that MCA is robust over a large range of attenuation values, even when there is significant deviation from the ideal zero-magnitude pixel assumption. As an example, the MCA restoration in Figure 4.5(e) corresponds to an experiment where the window gain is 0.1. Figures 4.5(c) and (d) show the perfectly focused and defocused images, respectively, associated with this restoration. The image in Figure 4.5(e) is almost perfectly restored, with $\text{SNR}_{out} = 9.583$ dB.

In Figure 4.6, the performance of MCA is compared with existing autofocus approaches. Figure 4.6(a) shows a perfectly focused simulated SAR image, constructed in the same manner as Figure 4.5, where the window function in Figure 4.5(b) has been applied (the window gain is 1×10^{-4} in this experiment). A defocused image formed by applying a quadratic phase error function (i.e., the phase error function varies as a quadratic function of the cross-range frequencies) is displayed in Figure 4.6(b); such a function is used to model phase errors due to platform motion [1]. The defocused image has been contaminated with additive white complex-Gaussian noise in the range-compressed do-

²The processed SAR images in this paper were provided by Sandia National Laboratories.

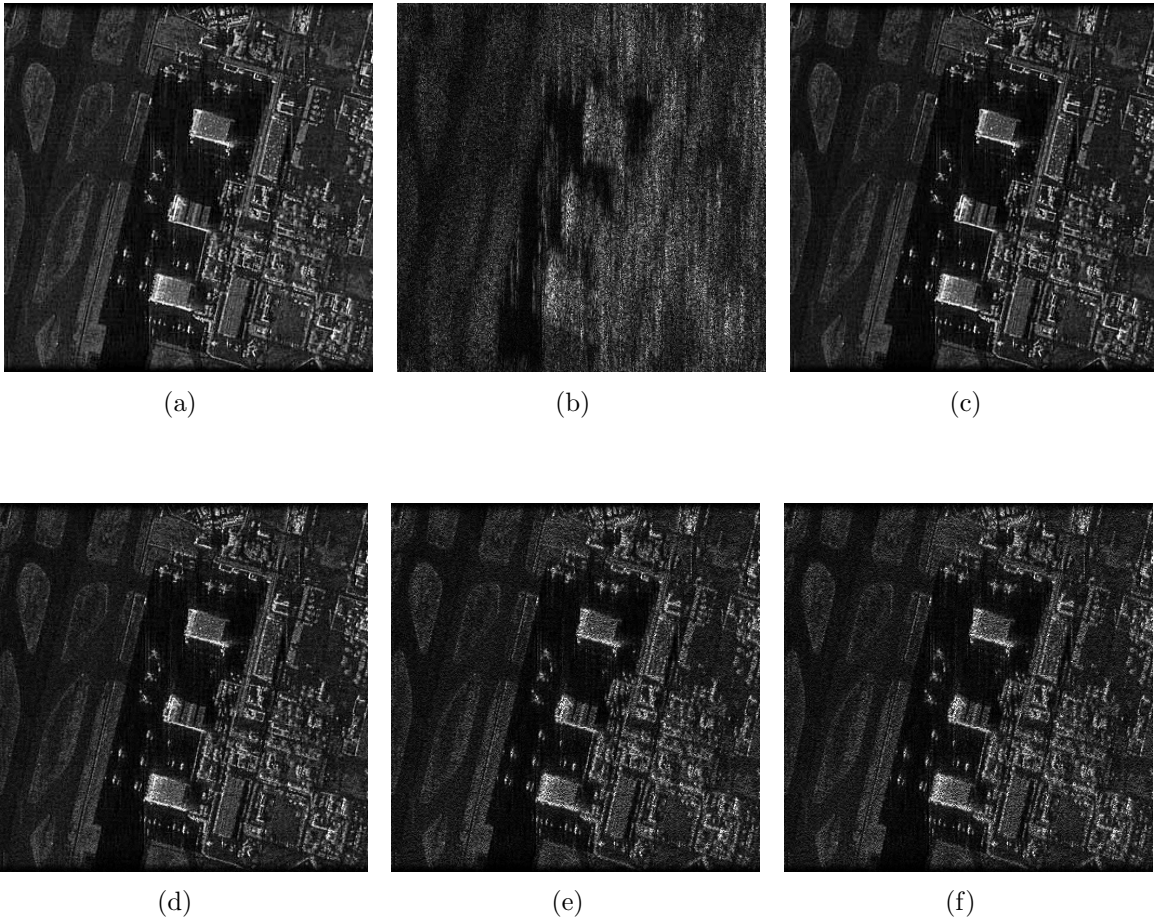


Figure 4.6 Comparison of MCA with existing autofocus approaches: (a) simulated 341×341 pixel perfectly focused image, where the window function in Figure 4.5(b) has been applied; (b) noisy defocused image produced by applying a quadratic phase error, where the input SNR is 40 dB (measured in the range-compressed domain); (c) MCA restoration ($\text{SNR}_{out} = 25.25$ dB); (d) PGA restoration ($\text{SNR}_{out} = 9.64$ dB); (e) entropy-based restoration ($\text{SNR}_{out} = 3.60$ dB); and (f) restoration using the intensity-squared sharpness metric ($\text{SNR}_{out} = 3.41$ dB).

main such that the *input signal-to-noise ratio* (input SNR) is 40 dB; here, the input SNR is defined to be the average per-pulse SNR: $\text{SNR} = 20 \log_{10} \{1/M \sum_k \max_n \tilde{G}[k, n]/\sigma_p\}$, where σ_p is the noise standard deviation. Figure 4.6(c) shows the MCA restoration formed assuming the top two and bottom two rows to be low-return; the image is observed to be well-restored, with $\text{SNR}_{out} = 25.25$ dB. To facilitate a meaningful comparison with the perfectly focused image, the restorations are produced by applying the phase error estimate to the *noiseless* defocused image; in other words, the phase estimate is determined in the presence of noise, but SNR_{out} is computed with the noise removed. A restoration produced using PGA is displayed in Figure 4.6(d) ($\text{SNR}_{out} = 9.64$ dB) [1]. Figures 4.6(e) and (f) show the result of applying a metric-based autofocus technique [18] using the entropy sharpness metric ($\text{SNR}_{out} = 3.60$ dB) and the intensity-squared sharpness metric ($\text{SNR}_{out} = 3.41$ dB), respectively. Of the four autofocus approaches, MCA is found to produce the highest quality restoration in terms of both qualitative comparison and the quality metric SNR_{out} . In particular, the metric-based restorations, while macroscopically similar to the MCA and PGA restorations, have much lower SNR; this is due to the metric-based techniques incorrectly accentuating some of the point scatterers.

Figure 4.7 presents the results of a Monte Carlo simulation comparing the performance of MCA with existing autofocus approaches under varying levels of additive noise. Ten trials were conducted at each input SNR level, where in each trial a noisy defocused image (using a deterministic quadratic phase error function) was formed using different randomly generated noise realizations with the same statistics. Four autofocus approaches (MCA, PGA, entropy-minimization, and intensity-squared minimization) were applied to each defocused image, and the quality metric SNR_{out} was evaluated on the resulting restorations. Plots of the average SNR_{out} (over the ten trials) versus the input SNR are displayed in Figure 4.7 for the four autofocus methods. The plot shows that at high input SNR ($\text{SNR} \geq 20$ dB), MCA provides the best restoration performance. At very low SNR, metric-based methods produce the highest SNR_{out} ; however, this performance is observed to level out around 3.5 dB due to the limitation of the sharpness criterion (several point scatterers are artificially accentuated). PGA provides the best

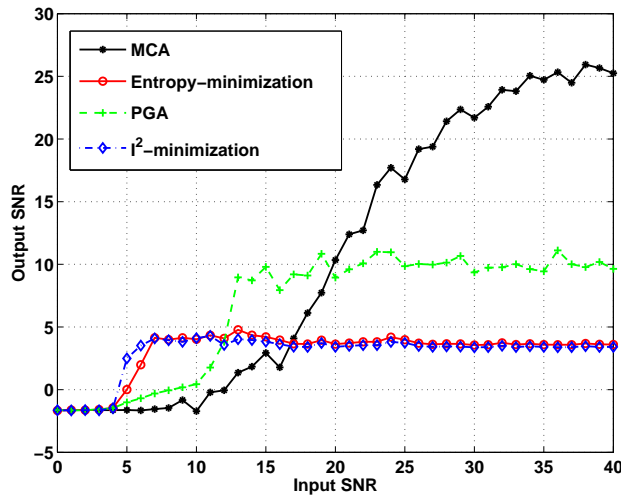


Figure 4.7 Plots of the restoration quality metric SNR_{out} versus the input SNR for MCA, PGA, entropy-minimization autofocus, and intensity-squared minimization autofocus. In this experiment, we performed a Monte Carlo simulation where MCA was applied to noisy versions of the defocused image in Figure 4.6(b); ten different white complex-Gaussian noise realizations were used for each experiment at a particular input SNR.

performance in the intermediate range of low SNR starting around 13 dB. Likewise, we observe that the MCA restorations start to resemble the perfectly focused image at 13 dB. PGA also approaches a constant SNR_{out} value at high input SNR; the limitation in PGA is the inability to extract completely isolated point scatterers free of surrounding clutter.

On average, the MCA restorations in the experiment of Figure 4.7 required 3.85 s of computation time, where the algorithm was implemented using MATLAB on an Intel Pentium 4 CPU (2.66 GHz). In comparison, PGA, the intensity-squared approach, and the entropy approach had average run-times of 5.34 s, 18.1 s, and 87.6 s, respectively. Thus, MCA is observed to be computationally efficient in comparison with existing SAR autofocus methods.

Figure 4.8 presents an experiment using a sinc-squared antenna pattern, where a significant amount of additive noise has been applied to the defocused image. The perfectly focused and defocused images are displayed in Figures 4.8(a) and (b), respectively,

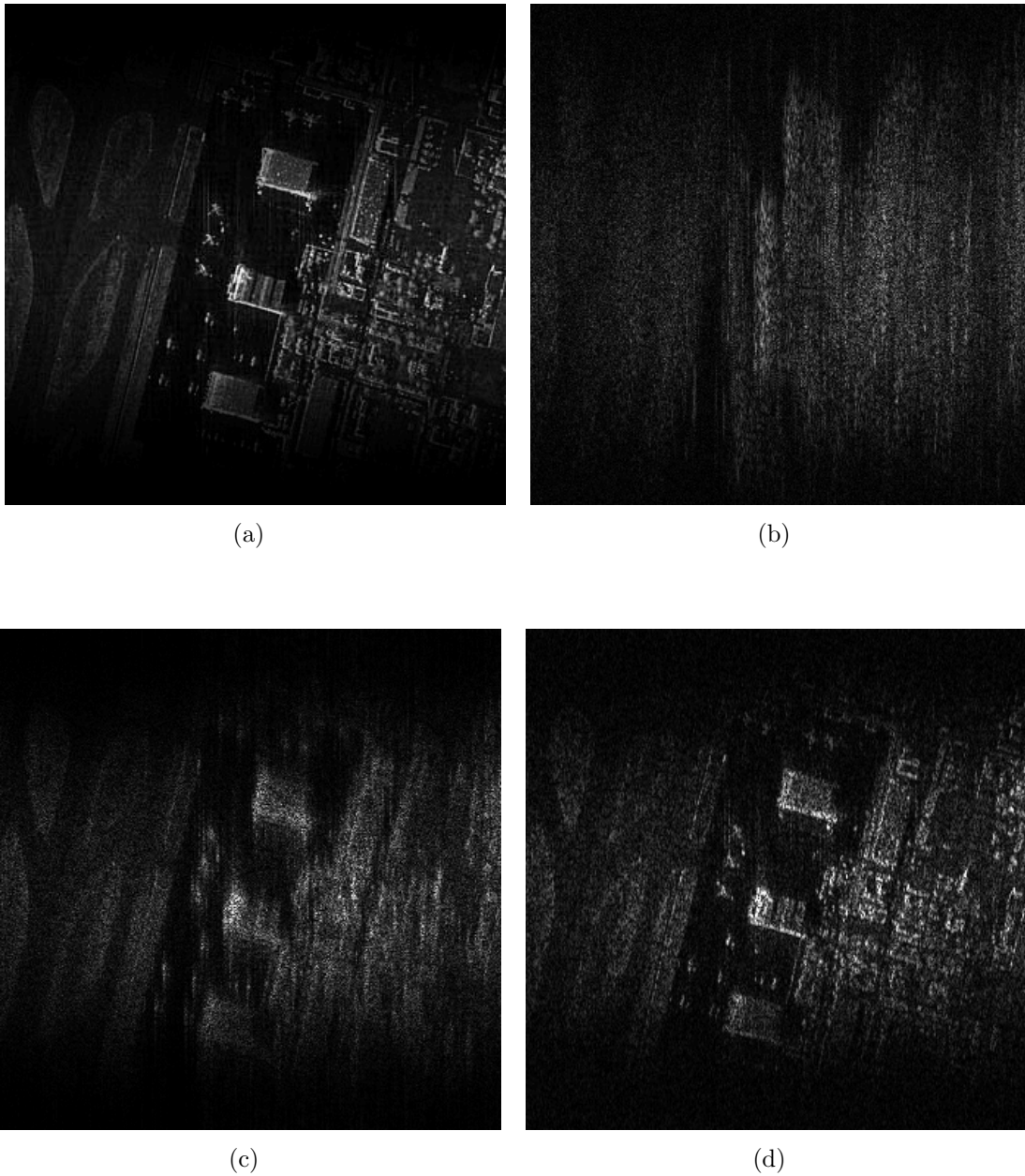


Figure 4.8 Experiment using entropy optimization as a regularization procedure to improve the MCA restoration when the input SNR is low. The optimization is performed over a space of 15 basis functions determined by the smallest singular values of the MCA matrix. (a) Perfectly focused image where a sinc-squared window is applied, (b) noisy defocused image with range-compressed domain SNR of 19 dB produced using a quadratic phase error, (c) MCA restoration, and (d) regularized MCA restoration using the entropy metric.

where the input SNR of the defocused image is 19 dB. Due to the gradual tapering of the sinc-squared antenna pattern, the smallest singular values of the MCA matrix are distributed closely together. As a result, the problem becomes poorly conditioned in the sense that small perturbations to the defocused image can produce large perturbations to the least-squares solution of (4.18). In such cases, regularization can be used to improve the solution, as described in Section 4.5. Figure 4.8(c) shows the MCA restoration where a large number of low-return constraints (45 low-return rows at the top and bottom of the image) are enforced to improve the solution in the presence of noise. In this restoration, much of the defocusing has been corrected, revealing the structure of the underlying image. However, residual blurring remains. Figure 4.8(d) shows the result of applying the regularization procedure in Section 5. Here, we form a subspace of 15 basis functions using the minimum right singular vectors of the MCA matrix where the data consistency relation (3.24) is satisfied. The optimal basis coefficients, corresponding to a unique solution within this subspace, are determined by minimizing the entropy metric. The regularized restoration is shown in Figure 4.8(d). The incorporation of the entropy-based sharpness optimization is found to significantly improve the quality of the restoration, producing a result that agrees well with the perfectly focused image. Thus, by exploiting the linear algebraic structure of the SAR autofocus problem and the low-return constraints in the perfectly focused image, the dimension of the optimization space in metric-based methods can be greatly reduced (from 341 to 15 parameters in this example).

CHAPTER 5

MULTICHANNEL ESTIMATION OF COIL SENSITIVITIES IN PARALLEL MRI

5.1 Introduction

In this chapter, we propose a new approach to the coil sensitivity estimation problem in PMRI that does not rely on the SOS assumptions used in existing methods. As discussed in Chapter 2, these assumptions tend to be violated towards the center of the image, thus leading to errors in the sensitivity estimates that can produce aliasing artifacts and poor contrast at the image center. Since our approach does not make use of SOS, it avoids these potential problems.

In our approach, we exploit the multichannel nature of the coil sensitivity estimation problem, where the sensitivity-encoded images are related to the common image function through a bank of parallel channel responses (i.e., the unknown sensitivity functions), as shown in Figure 5.1. Here, the output signals $\{\rho_i[n, m]\}$ are known, but the common input $\rho[n, m]$ and channel responses $\{s_i[n, m]\}$ are both unknown. Thus, the coil sensitivity estimation problem has a similar flavor to the more general problem of blind multichannel deconvolution (BMD). For the BMD problem, subspace-based techniques such as EVAM have been proposed that determine the unknown FIR coefficients of the channels using a linear algebraic framework [42, 43].

A distinction between our problem and the BMD problem is that the filtering operation considered here is described by multiplication in the spatial domain: $\rho_i[n, m] =$

This chapter includes research conducted jointly with Mathews Jacob and Minh N. Do [50].

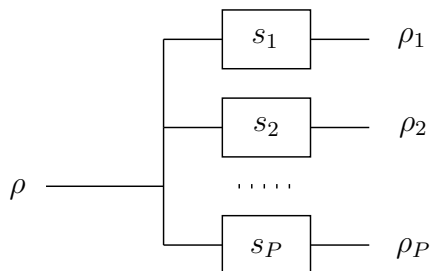


Figure 5.1 Diagram illustrating the multichannel nature of the coil sensitivity problem. Here, $\rho[n, m]$ is the image function, $\{s_i[n, m]\}$ are the coil sensitivity functions, and $\{\rho_i[n, m]\}$ are the sensitivity-encoded images, where $\rho_i[n, m] = \rho[n, m]s_i[n, m]$ (i.e., the filtering operation is described by multiplication in the spatial domain).

$\rho[n, m]s_i[n, m]$. It is possible to pose the sensitivity estimation problem as the convolution of a small number of coefficients in the Fourier domain (i.e., $\hat{\rho}_i[k_n, k_m] = \hat{\rho}[k_n, k_m] * \hat{s}_i[k_n, k_m]$). However, the sensitivity functions are discontinuous at the edges of the image field-of-view; this is because the receiver sensitivity decays as a function of increasing distance from the coil. Thus, a low-order Fourier basis generally provides a poor representation of these functions. Therefore, instead of using EVAM directly, we propose a novel EVAM-like technique for estimating the coil sensitivity functions. To deal with the spatial-domain multiplication, we represent the unknown sensitivity functions using a polynomial basis expansion. This allows the polynomial coefficients of the coil sensitivity functions to be determined through a linear algebraic formulation similar to EVAM. Due to the physical properties of the coils, the sensitivity functions are smooth and can be well approximated by low-order polynomials. The polynomial expansion also provides the benefit of regularizing the sensitivity estimates in the presence of noise. Aided by the sensitivity estimates, SENSE is used to reconstruct the image function.

Our approach is applicable both to cases where (a) pilot scans are available and (b) autocalibration data are collected at the center of k -space with each scan. In the later case, the sensitivity estimation is performed using low-resolution images formed from the autocalibration data. In addition, the proposed technique is noniterative, in contrast to [51], and has a computationally efficient form. We present experimental

results using actual and simulated PMRI data to assess the performance of the proposed approach. The results show that the sensitivity estimates from our approach can produce superior image restorations using SENSE in comparison to the standard SOS estimates. The performance of our method is evaluated using different acceleration factors and autocalibration data sizes.

5.2 Problem Formulation

The goal of the sensitivity estimation problem is to determine the sensitivity functions $s_i[n, m]$ ($1 \leq i \leq P$), where P is the number of coils, given the sensitivity-encoded images $\rho_i[n, m]$ obtained either from initial pilot scans or from autocalibration data collected at the center of k -space. By analogy with (2.19), we use the following multichannel model:

$$\rho_i[n, m] = \rho[n, m]s_i[n, m], \quad (5.1)$$

where $n = 0, 1, \dots, N-1$ and $m = 0, 1, \dots, M-1$ are spatial-domain coordinates for the x and y dimensions, respectively. In the autocalibrating case, the data are zero-padded prior to performing an inverse Fourier transform:

$$\hat{\rho}_i[k_n, k_m] \stackrel{\text{def}}{=} \begin{cases} \hat{\rho}_i(\Delta_n k_n, \Delta_m k_m) & \text{for } \frac{-N'}{2} \leq k_n \leq \frac{N'}{2} - 1 \text{ and } \frac{-M'}{2} \leq k_m \leq \frac{M'}{2} - 1 \\ 0 & \text{otherwise,} \end{cases} \quad (5.2)$$

where $\hat{\rho}_i$ are the k -space data in (2.18); Δ_n and Δ_m are the Nyquist sampling intervals required to reconstruct the object at full FOV in the k_x and k_y dimensions, respectively; $k_n = -N/2, -N/2 + 1, \dots, N/2 - 1$; $k_m = -M/2, -M/2 + 1, \dots, M/2 - 1$; and N', M' are the dimensions of the autocalibration data satisfying $N' \leq N$ and $M' \leq M$. Low-resolution images for estimating the sensitivity functions are then obtained from (5.2) using

$$\rho_i[n, m] = DFT_{k_n, k_m}^{-1} \{ \hat{\rho}_i[k_n, k_m] \}.$$

The sensitivity functions are usually smooth functions in space, i.e., they exhibit slow spatial variation [25]. As a result, the sensitivities can be modeled using a low-order basis

expansion:

$$s_i[n, m] = \sum_{k=1}^K c_i[k] \varphi_k[n, m], \quad (5.3)$$

where $\varphi_k[n, m]$ are basis functions spanning a space of smooth functions, $c_i[k]$ are coefficients associated with the i -th coil and k -th basis function, and K is the number of basis functions. As an example, the sensitivity functions are often represented by a basis of low-order polynomial functions [25, 51]:

$$s_i[n, m] = \sum_{q=0}^{R-1} \sum_{r=0}^{R-1} c_i[q, r] \varphi_{(q,r)}[n, m], \quad (5.4)$$

where

$$\varphi_{(q,r)}[n, m] \stackrel{\text{def}}{=} n^q m^r \quad (5.5)$$

and R is the polynomial order in each dimension. Given the basis expansion, the goal is to solve for the basis coefficients rather than determining the sensitivity functions directly. SENSE uses (5.4) as a noise reduction step given the SOS sensitivity estimates. In [51], (5.4) is used in an iterative nonlinear approach where the basis coefficients and $\rho[n, m]$ are jointly estimated.

In our approach, we use the basis characterization in (5.3) to incorporate the prior knowledge of the smoothness of the sensitivity functions so that a unique solution for the sensitivity functions can be determined. Without incorporating prior knowledge, there are PNM unknowns due to the sensitivity functions, and NM unknown pixels in $\rho[n, m]$. The sensitivity-encoded images provide PNM known nonlinear constraints using (5.1), and thus there are more unknown parameters than known parameters (i.e., $(P + 1)NM > PNM$). However, using the expansion in (5.3), the number of unknown parameters due to the sensitivity functions is reduced to PK , where $K \ll NM$. As a result, the number of unknowns becomes $PK + NM < PNM$. In the next section, we formulate the proposed technique, where (5.3) and the multichannel relationship in (5.1) provide a linear framework for directly solving for the basis coefficients.

5.3 Reconstruction Framework

5.3.1 Subspace-based framework

Consider the pair of coils $i, j \in \{1, 2, \dots, P\}$. We define

$$\mathcal{U} \stackrel{\text{def}}{=} \left\{ u_i : u_i[n, m] = \sum_{k=1}^K d_i[k] \varphi_k[n, m] \right\} \quad (5.6)$$

to be the space of all functions formed from the basis functions $\{\varphi_k[n, m]\}_{k=1}^K$, and consider the *consistency relationship*

$$\rho_j[n, m] u_i[n, m] - \rho_i[n, m] u_j[n, m] = 0. \quad (5.7)$$

Under condition (5.1), equation (5.7) is equivalent to

$$\rho[n, m] (s_j[n, m] u_i[n, m] - s_i[n, m] u_j[n, m]) = 0. \quad (5.8)$$

Note that by (5.8), the consistency relationship is satisfied for $u_i = \alpha s_i$ and $u_j = \alpha s_j$, where α is a scalar constant. Therefore, with given $\{\rho_i, \rho_j\}$, if (5.7) has a unique solution for $\{u_i, u_j\}$ to within a scalar constant, then the coil sensitivities $\{s_i, s_j\}$ can be obtained as the solution to (5.7).

At pixels where the image function is nonzero, i.e., over the support of the object, the term within parentheses in (5.8) must be equal to zero:

$$s_j[n, m] u_i[n, m] - s_i[n, m] u_j[n, m] = 0 \text{ for all } (n, m) : \rho[n, m] \neq 0. \quad (5.9)$$

Expressing $s_i[n, m]$ and $u_i[n, m]$ using (5.3) and (5.6) in (5.9) produces

$$\sum_{k=1}^K \sum_{k'=1}^K (c_j[k] d_i[k'] - c_i[k] d_j[k']) \phi_{k,k'}[n, m] = 0 \text{ for all } (n, m) : \rho[n, m] \neq 0., \quad (5.10)$$

where

$$\phi_{k,k'}[n, m] = \varphi_k[n, m] \varphi_{k'}[n, m]. \quad (5.11)$$

Since $\phi_{k,k'}[n, m] = \phi_{k',k}[n, m]$, (5.10) can be rewritten as

$$\sum_{k=1}^K \sum_{k'=k}^K f_{\mathbf{c}, \mathbf{d}}[k, k'] \phi_{k,k'}[n, m] = 0 \text{ for all } (n, m) : \rho[n, m] \neq 0, \quad (5.12)$$

where

$$f_{\mathbf{c},\mathbf{d}}[k, k'] = \begin{cases} c_j[k]d_i[k'] + c_j[k']d_i[k] - c_i[k]d_j[k'] - c_i[k']d_j[k] & \text{for } k \neq k' \\ c_j[k]d_i[k] - c_i[k]d_j[k] & \text{for } k = k', \end{cases} \quad (5.13)$$

$\mathbf{c} = [c_i[1], \dots, c_i[K] | c_j[1], \dots, c_j[K]]^T$, and $\mathbf{d} = [d_i[1], \dots, d_i[K] | d_j[1], \dots, d_j[K]]^T$. A solution for $d_i[k]$ satisfying (5.12) is given by

$$d_i[k] = \alpha c_i[k], \quad (5.14)$$

where α is a multiplicative constant common to both i and j ; note that this solution provides the desired coefficients. In the next subsection, we study the uniqueness of solutions to (5.12).

5.3.2 Uniqueness of solutions

5.3.2.1 General basis expansion

In the following proposition, we state a necessary condition for a unique solution to (5.12) (where the solution is unique to within a multiplicative constant common to all coils). This condition holds for the general basis expansion in (5.3).

Proposition 4 (Necessary condition for a unique solution) *Let*

$$\Omega \stackrel{\text{def}}{=} \{\phi_{k,k'}[n, m] : 1 \leq k \leq K, k \leq k' \leq K\},$$

where $\phi_{k,k'}[n, m] = \varphi_k[n, m]\varphi_{k'}[n, m]$. Suppose that $s_i \in \mathcal{U}$ and $s_j \in \mathcal{U}$. A necessary condition for obtaining a unique solution for $u_i \in \mathcal{U}$ and $u_j \in \mathcal{U}$ in (5.7) is that Ω contains at least $2K - 1$ linearly independent functions.

Proof: The analysis in Section 5.3.1 shows that under the assumption $s_i \in \mathcal{U}$ and $s_j \in \mathcal{U}$, (5.7) has a unique solution for $u_i \in \mathcal{U}$ and $u_j \in \mathcal{U}$ to within a scalar constant if and only if (5.12) has a unique solution for \mathbf{d} to within a scalar constant. Suppose all of the functions $\phi_{k,k'}[n, m] \in \Omega$ are linearly independent. Then each of the coefficients $f_{\mathbf{c},\mathbf{d}}[k, k']$ must be zero to satisfy (5.12). However, in general some of the $\phi_{k,k'}[n, m] \in \Omega$ may be

linearly dependent. In this case, the linearly dependent functions can be expressed in terms of the linearly independent functions, so that (5.12) is expressed only in terms of linearly independent functions. Let v index all pairs of (k, k') . Then (5.12) can be written as (for all $(n, m) : \rho[n, m] \neq 0$)

$$\sum_v f_{\mathbf{c}, \mathbf{d}}[v] \phi_v[n, m] = 0.$$

Define $\Omega_{\mathcal{L}} \subset \Omega$ to be a subset of linearly independent functions so that if $\phi_v \in \Omega$ and $\phi_v \notin \Omega_{\mathcal{L}}$, then $\phi_v \in \text{span}(\Omega_{\mathcal{L}})$, and define $\mathcal{L} = \{v : \phi_v \in \Omega_{\mathcal{L}}\}$. This allows (5.12) to be partitioned as

$$\sum_{v \in \mathcal{L}} f_{\mathbf{c}, \mathbf{d}}[v] \phi_v[n, m] + \sum_{w \notin \mathcal{L}} f_{\mathbf{c}, \mathbf{d}}[w] \phi_w[n, m] = 0. \quad (5.15)$$

The linearly dependent functions can be expressed in terms of the functions in \mathcal{L} as follows:

$$\phi_w[n, m] = \sum_{v \in \mathcal{L}} a_v[w] \phi_v[n, m] \text{ for all } w \notin \mathcal{L} \quad (5.16)$$

for some set of coefficients $a_v[w]$. Substituting (5.16) into (5.15) produces

$$\sum_{v \in \mathcal{L}} \underbrace{\left(f_{\mathbf{c}, \mathbf{d}}[v] + \sum_{w \notin \mathcal{L}} a_v[w] f_{\mathbf{c}, \mathbf{d}}[w] \right)}_{\hat{f}_{\mathbf{c}, \mathbf{d}}[v]} \phi_v[n, m] = 0. \quad (5.17)$$

The new expansion coefficients $\hat{f}_{\mathbf{c}, \mathbf{d}}[v]$ associated with the set of linearly independent functions are linear functions of \mathbf{d} :

$$\begin{aligned} \hat{f}_{\mathbf{c}, \mathbf{d}}[k, k'] &= f_{\mathbf{c}, \mathbf{d}}[k, k'] + \sum_{(l, l') \notin \mathcal{L}} a_{k, k'}[l, l'] f_{\mathbf{c}, \mathbf{d}}[l, l'] \\ &\stackrel{\text{def}}{=} \{\mathbf{M}(\mathbf{c})\}_{(k, k')} \mathbf{d}, \end{aligned} \quad (5.18)$$

where we have reexpressed $v \in \mathcal{L}$ and $w \notin \mathcal{L}$ in (5.17) using the ordered pairs (k, k') and (l, l') , respectively, and $\{\mathbf{M}(\mathbf{c})\}_{(k, k')}$ is a $1 \times 2K$ vector function of \mathbf{c} .

For (5.17) to be satisfied, all of the coefficients $\hat{f}_{\mathbf{c}, \mathbf{d}}[k, k']$ in (5.18) must be equal to zero. Setting each of these coefficients to zero produces a system of linear equations in

terms of \mathbf{d} :

$$\mathbf{M}(\mathbf{c})\mathbf{d} = \mathbf{0}, \quad (5.19)$$

where $\mathbf{M}(\mathbf{c})$ is a matrix formed from the row vectors $\{\mathbf{M}(\mathbf{c})\}_{(k,k')}$ in (5.18). Because there are $2K$ unknowns in \mathbf{d} , a unique solution for \mathbf{d} exists only if there are at least $2K - 1$ linearly independent functions in Ω , i.e., $\mathbf{M}(\mathbf{c})$ must have at least $2K - 1$ rows. Only $2K - 1$ functions are required because the solution is ambiguous to within a multiplicative scaling constant common to all the coils, thus taking away a degree of freedom. Note that if all of the functions in Ω are linearly independent, then there are $K(K + 1)/2 \geq 2K - 1$ constraints, i.e., the necessary condition is always satisfied. \square

5.3.2.2 Special case: Polynomial basis expansion

Proposition 4 provides only a necessary condition because the rank of $\mathbf{M}(\mathbf{c})$ in (5.19) must be taken into account to guarantee a unique solution. Sufficient conditions for a unique solution can be determined for the special case of the polynomial basis expansion in (5.5). As mentioned in Section 2, the polynomial basis expansion is often used in practice to model the sensitivity functions.

Analogous to (5.6), we define

$$u_i[n, m] \stackrel{\text{def}}{=} \sum_{q=0}^{R-1} \sum_{r=0}^{R-1} d_i[q, r] n^q m^r. \quad (5.20)$$

Our goal is to demonstrate that the necessary and sufficient conditions for a unique solution are satisfied for the polynomial basis. First, we express the product $s_j[n, m]u_i[n, m]$ in (5.9) using (5.4), (5.5), and (5.20):

$$s_j[n, m]u_i[n, m] = \sum_{q=0}^{R-1} \sum_{q'=0}^{R-1} \sum_{r=0}^{R-1} \sum_{r'=0}^{R-1} c_j[q, r] d_i[q', r'] n^{q+q'} m^{r+r'}. \quad (5.21)$$

Using the change of variables $t \stackrel{\text{def}}{=} q + q'$ and $z \stackrel{\text{def}}{=} r + r'$ produces

$$s_j[n, m]u_i[n, m] = \sum_{q=0}^{R-1} \sum_{t=q}^{R+q-1} \sum_{r=0}^{R-1} \sum_{z=r}^{R+r-1} c_j[q, r] d_i[t - q, z - r] n^t m^z.$$

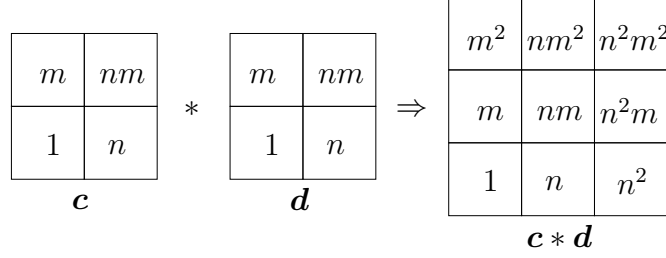


Figure 5.2 Illustration of the convolution of polynomial basis coefficients associated with two coils for the case where $R = 2$.

By definition, the coefficients $c_j[q, r]$ and $d_i[q, r]$ are zero outside the range $0 \leq q \leq r \leq R - 1$. This allows the summation indices to be modified as follows:

$$s_j[n, m]u_i[n, m] = \sum_{t=0}^{2R-2} \sum_{z=0}^{2R-2} \underbrace{\left(\sum_{q=0}^{R-1} \sum_{r=0}^{R-1} c_j[q, r] d_i[t - q, z - r] \right)}_{c_j[t, z] * d_i[t, z]} n^t m^z, \quad (5.22)$$

where $*$ denotes 2-D convolution in t and z . Thus, under the polynomial basis expansion, the multiplication of the functions in (5.9) can be viewed in terms of the 2-D convolution of the polynomial coefficients. Figure 5.2 illustrates the convolution of the polynomial basis coefficients for the case where $R = 2$.

Using (5.22), the relationship (5.9) can be expressed as (for all $(n, m) : \rho[n, m] \neq 0$)

$$\sum_{q=0}^{2R-2} \sum_{r=0}^{2R-2} \underbrace{(c_j[q, r] * d_i[q, r] - c_i[q, r] * d_j[q, r])}_{\hat{f}_{\mathbf{c}, \mathbf{d}}[q, r]} n^q m^r = 0, \quad (5.23)$$

where, analogous to (5.17), the functions $\phi_{(q,r)}[n, m] \stackrel{\text{def}}{=} n^q m^r$ are linearly independent. Thus, for (5.23) to be satisfied,

$$\hat{f}_{\mathbf{c}, \mathbf{d}}[q, r] = c_j[q, r] * d_i[q, r] - c_i[q, r] * d_j[q, r] = 0 \text{ for } 0 \leq q \leq r \leq 2R - 2. \quad (5.24)$$

Note that in (5.23) there are $(2R - 1)^2$ linearly independent functions, and the number of basis functions in (5.4) is $K = R^2$. Proposition 4 requires at least $2K - 1 = 2R^2 - 1$ linearly independent functions for a unique solution. Thus, since $(2R - 1)^2 \geq 2R^2 - 1$, the necessary condition for a unique solution is satisfied by the polynomial basis.

We note that (5.24) is equivalent to the condition in BMD methods such as EVAM that determine unknown FIR channel responses using a subspace framework [42, 43]. In these methods, a unique solution to \mathbf{d} in (5.24) can be guaranteed given an additional *coprime assumption*. Suppose that the z -transforms of $c_i[q, r]$ ($c_i(z_q, z_r)$, $1 \leq i \leq P$), are coprime, i.e., they share no common factors except for a scalar constant. Then, since $c_i[q, r]$ and $d_i[q, r]$ are assumed to have the same support, it can be shown that (Proposition 4 in [43]) all solutions to (5.24) have the form

$$d_i[q, r] = \alpha c_i[q, r], \quad (5.25)$$

where α is a scalar constant common to all coils. Thus, under the coprime assumption, there is a unique solution to within a scalar constant that is also the correct solution.

In the next subsection, we show how the unique solution in (5.25) is determined given the sensitivity-encoded images $\rho_i[n, m]$.

5.3.3 Estimation of coil sensitivities

To derive the procedure for computing the coefficients associated with the unknown sensitivity functions, we first consider the pair of coils i and j . Using (5.6) and (5.7), we obtain the relationship

$$\sum_{k=1}^K d_i[k] \psi_{j,k}[n, m] - \sum_{k=1}^K d_j[k] \psi_{i,k}[n, m] = 0, \quad (5.26)$$

where

$$\psi_{i,k}[n, m] \stackrel{\text{def}}{=} \rho_i[n, m] \varphi_k[n, m] \quad (5.27)$$

are known functions formed from the acquired sensitivity-encoded images and the polynomial basis functions (k is used to index the pair (q, r) , where $K = R^2$). Writing (5.26) in matrix form produces

$$\mathbf{A} \mathbf{d} = \mathbf{0}, \quad (5.28)$$

where

$$\mathbf{A} = [\Psi_j | -\Psi_i], \quad (5.29)$$

$$\mathbf{\Psi}_i \stackrel{\text{def}}{=} [\boldsymbol{\psi}_{i,1}, \boldsymbol{\psi}_{i,2}, \dots, \boldsymbol{\psi}_{i,K}], \quad (5.30)$$

and $\boldsymbol{\psi}_{i,k} = \mathbf{vec}\{\psi_{i,k}[n, m]\}$ is a vectorized version of $\psi_{i,k}[n, m]$. In this two-channel case, \mathbf{A} is an $NM \times 2K$ matrix, and by (5.25) the unique solution to (5.28) gives the coefficients of the unknown sensitivity functions:

$$\hat{\mathbf{d}} = \text{Null}\{\mathbf{A}\} = \alpha \mathbf{c}. \quad (5.31)$$

In practice, the sensitivity functions may not be perfectly modeled by the assumed basis expansion, and additive noise may be present. Thus, \mathbf{A} generally has full column rank, and we use the least-squares solution given by the minimum right singular vector of \mathbf{A} :

$$\hat{\mathbf{d}} = \arg \min_{\|\mathbf{d}\|_2=1} \|\mathbf{A}\mathbf{d}\|_2. \quad (5.32)$$

When there are more than two channels, \mathbf{A} is constructed so that (5.26) is evaluated for every pair of channel responses simultaneously, similar to the block matrix structure used in the BMD techniques in [42] and [43]. The following recursive definition is used to form \mathbf{A} when there are P channels (the notation in the following three equations is adapted directly from [43]):

$$\mathbf{A}_{P-1} \stackrel{\text{def}}{=} [\mathbf{\Psi}_P | -\mathbf{\Psi}_{P-1}], \quad (5.33)$$

$$\mathbf{A}_t \stackrel{\text{def}}{=} \left[\begin{array}{c|ccc} \mathbf{\Psi}_{t+1} & -\mathbf{\Psi}_t & & \\ \mathbf{\Psi}_{t+2} & & -\mathbf{\Psi}_t & \\ \vdots & & & \ddots \\ \mathbf{\Psi}_P & & & -\mathbf{\Psi}_t \\ \hline \mathbf{0} & & \mathbf{A}_{t+1} & \end{array} \right] \quad \text{for } 1 \leq t \leq P-2, \quad (5.34)$$

and

$$\mathbf{A} \stackrel{\text{def}}{=} \mathbf{A}_1. \quad (5.35)$$

The matrix \mathbf{A} in (5.35) has dimensions $NMP(P-1)/2 \times PK$. In this general case, \mathbf{d} in (5.28) has the form

$$\mathbf{d} = [\mathbf{d}_1^T, \mathbf{d}_2^T, \dots, \mathbf{d}_P^T]^T, \quad (5.36)$$

where $\mathbf{d}_i \stackrel{\text{def}}{=} [d_i[1], d_i[2], \dots, d_i[K]]^T$.

5.3.4 Efficient estimation procedure

The computational expense of forming \mathbf{A} in (5.35) and performing its eigendecomposition is prohibitively large, both in terms of memory and CPU time. Note that the minimum right singular vector of \mathbf{A} satisfying (5.32) can be determined by computing the minimum eigenvector of the $PK \times PK$ matrix:

$$\mathbf{B} \stackrel{\text{def}}{=} \mathbf{A}^H \mathbf{A}. \quad (5.37)$$

Due to the structure of \mathbf{A} , the matrix \mathbf{B} can be determined directly in a very efficient manner without explicitly constructing \mathbf{A} . First, we form the matrices $\Psi_i \in \mathbb{C}^{NM \times K}$ in (5.30) for $i = 1, 2, \dots, P$. Given these matrices, \mathbf{B} can be partitioned into $K \times K$ blocks $\mathbf{C}_{j,i}$ [43]:

$$\mathbf{C}_{j,i} = \begin{cases} \sum_{l \neq i} \Psi_l^H \Psi_l & i = j \\ -\Psi_j^H \Psi_i & i \neq j, \end{cases} \quad (5.38)$$

where $i, j = 1, 2, \dots, P$, such that

$$\mathbf{B} = \begin{bmatrix} \mathbf{C}_{1,1} & \mathbf{C}_{1,2} & \dots & \mathbf{C}_{1,P} \\ \mathbf{C}_{2,1} & \mathbf{C}_{2,2} & \dots & \mathbf{C}_{2,P} \\ \vdots & \vdots & \ddots & \vdots \\ \mathbf{C}_{P,1} & \mathbf{C}_{P,2} & \dots & \mathbf{C}_{P,P} \end{bmatrix}. \quad (5.39)$$

Since $PK \ll NM$,¹ the total computational complexity of constructing \mathbf{B} and computing its eigenvectors is $O(P^2 K^2 NM)$ (the complexity of constructing \mathbf{B} is $O(P^2 K^2 NM)$ and the complexity of a full eigendecomposition is $O(P^3 K^3)$). Note that in the forementioned efficient procedure, both the memory requirements and computational complexity have been reduced by a factor of P^2 .

¹In a typical experiment, $P = 8$, $K = 9$, and $M = N = 128$. Therefore we have $PK = 72$ and $NM = 16384$, satisfying the assumption $PK \ll NM$.

5.3.5 Constructing the basis functions

In this work, we use the polynomial basis functions in (5.5). In practice, we find that the sensitivity functions often can be represented accurately using polynomials up to order $R = 3$ or $R = 4$.

To improve the conditioning of \mathbf{A} , we orthonormalize the basis functions over the support of the object. This involves first applying a binary mask to each of the basis functions, where pixels outside of the object support are set to zero, and then applying Gram-Schmidt to the (vectorized) masked basis functions. The mask is produced by forming a composite image using SOS; here, the maximum absolute value of the SOS image is determined, and pixels in the SOS image with magnitudes less than a small percentage of the maximum value are set to zero in the mask. Figure 5.3(a) shows the polynomial basis function $\varphi_{(2,1)}[n, m] = n^2m$ prior to orthonormalization and masking. A binary mask formed using SOS is displayed in Figure 5.3(b). Figure 5.3(c) shows the result of applying the mask to the basis function in Figure 5.3(a). The orthonormalized version of the masked basis function in Figure 5.3(c) is shown in Figure 5.3(d).

In practice, the solution to (5.32) can be very sensitive to noise outside of the object. This is due to the basis functions in (5.5) having large values at the edges of the image, causing small noise values in $\rho_i[n, m]$ to be amplified in the product (5.27). Therefore, the masking process prevents noise outside of the object from being amplified, reducing the perturbation to the desired solution. More importantly, applying a mask *prior* to orthonormalization makes the basis functions orthonormal over the support of the object. Without the masking-and-orthonormalization sequence, the basis functions are approximately linearly dependent; this is due to the higher-order basis functions being well approximated by combinations of the lower-order basis functions over the object support.

Figure 5.4 presents a simulation demonstrating the importance of orthonormalizing the basis functions over the support of the object. In Figure 5.4(a), the 2-D basis functions are vectorized (i.e., column-by-column concatenation) and stored as the columns of a

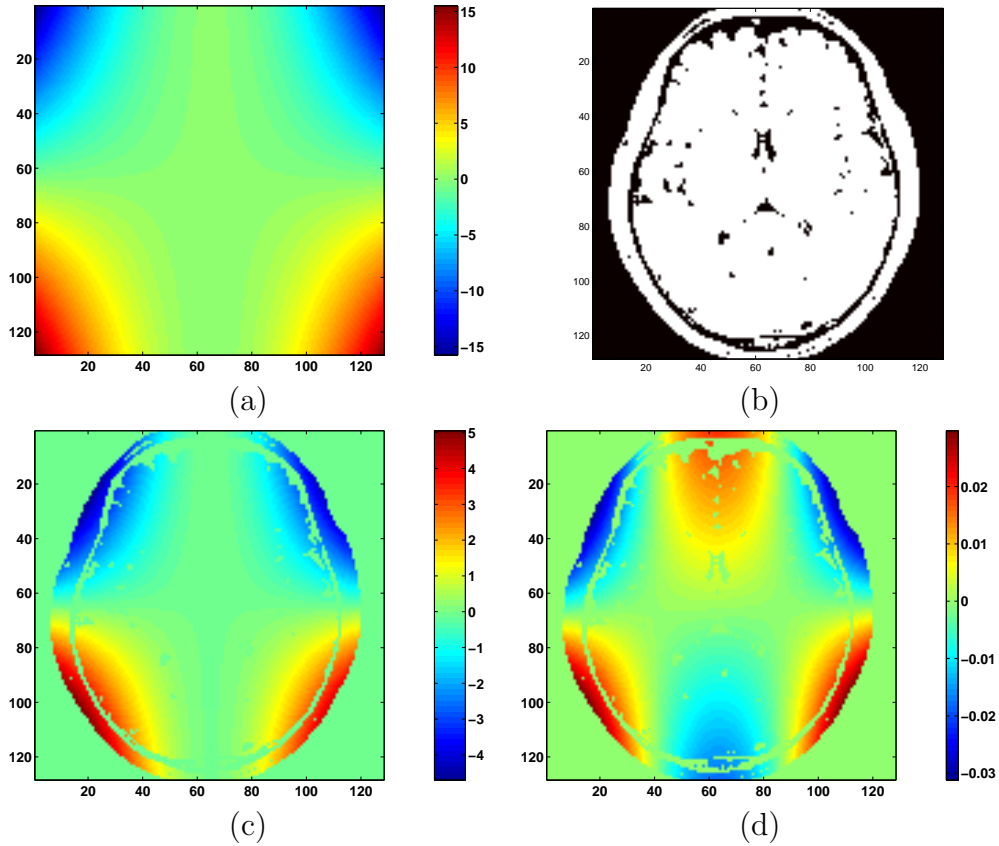


Figure 5.3 Example of a particular polynomial basis function: (a) basis function $\varphi_{(2,1)}[n, m] = n^2m$, (b) binary mask that is one within the object support and zero otherwise, (c) masked version of the basis function in (a), and (d) basis function after performing orthonormalization.

$NM \times R^2$ matrix. The plot shows the singular values of this matrix for the case where (i) the orthonormalization step is applied prior to masking (circular markers), and (ii) the orthonormalization is applied after masking (star markers). In case (i), masking the basis functions causes them to no longer be orthonormal; this is significant because by (5.27), case (i) is essentially the same as not performing the masking step (since $\rho_i[n, m] \approx 0$ at pixels where the mask is zero). Figure 5.4(b) shows the singular values of the matrix \mathbf{A} formed using a set of simulated PMRI data² and the basis functions in case (i) (circular

²The data sets used in our experiments were produced by Dr. Fa-Hsuan Lin of Harvard University, and are available online at www.nmr.mgh.harvard.edu/~fhlin/tool_sense.htm. We acknowledge Dr. Fa-Hsuan Lin for permission to use the data in our experiments.

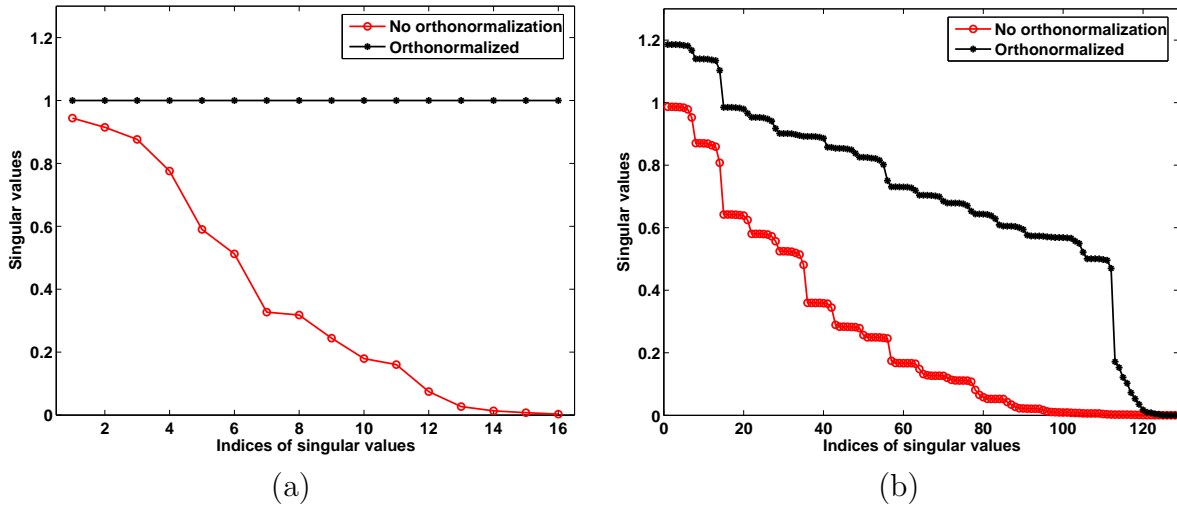


Figure 5.4 Illustration of the importance of the masking-and-orthonormalization sequence in constructing the basis functions: (a) singular values of the matrix of vectorized basis functions for the case where (i) orthonormalization has been performed prior to masking (circular markers) and (ii) orthonormalization is applied *after* masking (star markers), and (b) singular values of the matrix \mathbf{A} using the basis functions for the previous case in (a) (circular markers) and the later case (star markers). In the later case, the conditioning of \mathbf{A} is improved; i.e., there are fewer singular values close to zero.

markers) and case (ii) (star markers). In case (ii), the conditioning of \mathbf{A} is improved, i.e., there are fewer singular values close to zero. In practice, we find that the proposed technique can produce incorrect solutions if the masking and orthonormalization sequence in case (ii) is not performed.

5.3.6 Validation of assumptions in the proposed technique

In the proposed technique, there are two assumptions that require validation. The first assumption is that the sensitivity functions are accurately represented by a polynomial basis using a small number of basis functions. The second assumption is that the EVAM-like linear algebraic formulation in (5.28) is sufficiently well conditioned to produce correct restorations when the mathematical model for the problem is not exact.

To address the first assumption, we use a set of simulated PMRI data where the coil sensitivity functions for an eight-coil head array (simulated using Biot-Savart’s law)

are given [52]. For a particular polynomial order R , we project the actual sensitivity functions onto the basis of polynomial functions up to order R :

$$\hat{s}_i^{(R)}[n, m] = \mathcal{P}_R\{s_i[n, m]\}, \quad (5.40)$$

where \mathcal{P}_R denotes the projection onto the span of (orthonormalized) basis functions $\varphi_{(q,r)}[n, m]$ in (5.5) where $0 \leq q \leq r \leq R-1$, and $\hat{s}_i^{(R)}[n, m]$ is the resulting approximation to the sensitivity function. Note that (5.40) provides the best possible estimate of the sensitivity functions for fixed R . Figure 5.5 shows plots of the relative error between the actual sensitivity functions and their R -th order approximation as a function of R . Here, the relative error is defined as

$$\frac{\|\mathbf{vec}\{s_i\} - \mathbf{vec}\{\hat{s}_i^{(R)}\}\|_2}{\|\mathbf{vec}\{s_i\}\|_2}. \quad (5.41)$$

The figure shows that the relative error is small when polynomials up to order $R = 3$ or greater are used, and that the error is close to zero for $R \geq 5$. Note that plots for all eight coils are displayed in Figure 5.5; the plots from coils (1, 3, 5, 7) and (2, 4, 6, 8) appear superimposed (the two sets of coils correspond to receivers at the sides and corners of the square FOV, respectively).

To test the robustness of the linear algebraic formulation in (5.28), we performed a series of Monte Carlo simulations applying different levels of additive noise to the sensitivity-encoded images. For simplicity, we consider a case where the image function is constant over the entire FOV, so that $\rho[n, m] = 1$ and $\rho_i[n, m] = s_i[n, m]$. In addition, we force the sensitivity functions to reside in the span of the selected basis, so that $\rho_i[n, m] = \mathcal{P}_R\{s_i[n, m]\}$. The reason for doing this is to control the perturbation to the data, precluding errors due to deviations from the model (5.4); in other words, the additive noise is the only source of perturbation in this experiment. The goal of the experiments is to evaluate the reconstruction performance using the noisy images:

$$\tilde{\rho}_i[n, m] \stackrel{\text{def}}{=} \mathcal{P}_R\{s_i[n, m]\} + \xi_\sigma[n, m], \quad (5.42)$$

where the elements of $\xi_\sigma[n, m]$ are uncorrelated and selected from a zero-mean complex-Gaussian distribution with variance σ^2 . We define the *input signal-to-noise ratio* (input

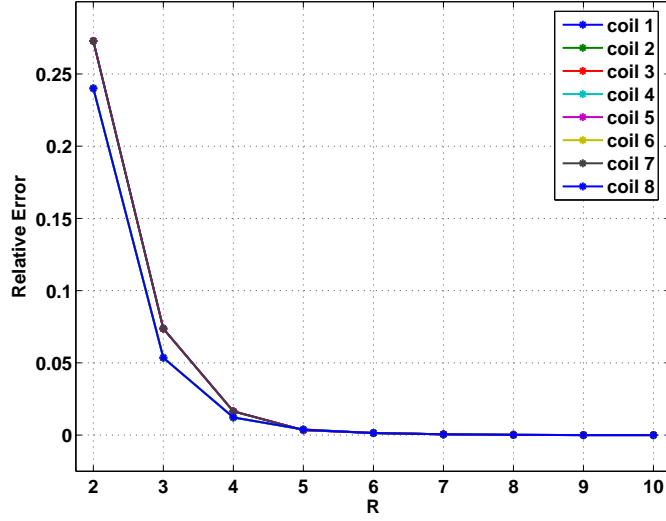


Figure 5.5 Plots of the relative error (defined in (5.41)) between the actual sensitivity functions and their R -th order approximation in (5.40) as a function of R for each coil.

SNR) as a measure of the noise level in images of (5.42) as follows:

$$\text{SNR} \stackrel{\text{def}}{=} 20 \log_{10} \frac{\|\text{vec}\{\mathcal{P}_R\{\mathbf{s}_i\}\}\|_2}{\sqrt{NM}\sigma}. \quad (5.43)$$

Five trials were conducted at each input SNR level, where in each trial the noisy images in (5.42) were formed using different randomly-generated noise realizations with the same statistics. The proposed technique was then applied to the noisy images, producing estimates of the sensitivity functions. The following restoration quality metric, denoted SNR_{out} (i.e., *output signal-to-noise ratio*), was evaluated for the sensitivity estimates [49]:

$$\text{SNR}_{out} \stackrel{\text{def}}{=} 20 \log_{10} \frac{\|\text{vec}\{\mathbf{S}\}\|_2}{\|(|\text{vec}\{\mathbf{S}\}| - |\text{vec}\{\hat{\mathbf{S}}\})\|_2}, \quad (5.44)$$

where

$$\mathbf{S} = [\text{vec}\{\mathcal{P}_R\{\mathbf{s}_1\}\}, \text{vec}\{\mathcal{P}_R\{\mathbf{s}_2\}\}, \dots, \text{vec}\{\mathcal{P}_R\{\mathbf{s}_P\}\}],$$

and

$$\hat{\mathbf{S}} = [\text{vec}\{\hat{\mathbf{s}}_1\}, \text{vec}\{\hat{\mathbf{s}}_2\}, \dots, \text{vec}\{\hat{\mathbf{s}}_P\}]$$

is a matrix of the sensitivity estimates $\hat{s}_i[n, m]$ produced using our technique. Note that in (5.44), the “noise” refers to the absolute error between the estimated and actual

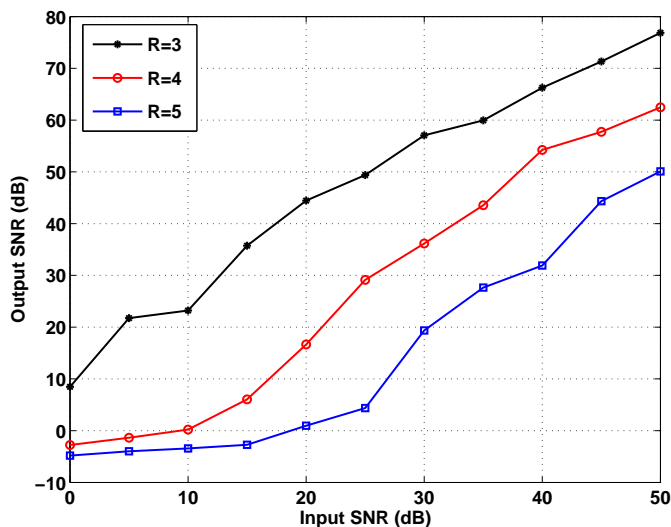


Figure 5.6 Plots of the restoration quality metric SNR_{out} in (5.44) as a function of input signal-to-noise ratio (defined in (5.43)). For simplicity, we assume that $\rho[n, m] = 1$ and that the actual sensitivity functions are described exactly by the selected basis. The three plots show cases where $R = 3$ (star markers), $R = 4$ (circular markers), and $R = 5$ (square markers). These plots reveal that the solution becomes more sensitive to noise as the polynomial order is increased.

sensitivity functions, and should not be confused with the additive noise considered in (5.42).

Figure 5.6 shows plots of SNR_{out} (averaged over the five trials) as a function of input SNR for cases where $R = 3$ (star markers), $R = 4$ (circular markers), and $R = 5$ (square markers). The plots reveal that the solution becomes more sensitive to noise as the polynomial order is increased. Thus, while Figure 5.5 shows that the error due to the polynomial approximation is reduced for larger R , Figure 5.6 shows that the conditioning is improved for smaller R . In practice, the best results are observed using $R = 3$ or $R = 4$; in experiments, we find that using $R \geq 5$ usually produces erroneous estimates of the sensitivity functions. The example in Figure 5.5 demonstrates that the increase in approximation accuracy using polynomial orders greater than 4 is negligible.

5.4 Coil Estimation and Reconstruction Results

Figure 5.7 presents an experiment using simulated sensitivity functions for an eight-channel head array coil, where the full-resolution image function is $N = 128$ by $M = 128$ pixels. To estimate the sensitivity functions, we applied our technique and SOS to the low-resolution images formed using $N' = 64$ by $M' = 64$ blocks of autocalibration data from each coil. Figures 5.7(a)-(c) compare the actual and estimated sensitivities for coil 4 (selected as a representative example). The sensitivity estimate using our approach is observed to be more accurate than the SOS estimate. We observe similar performance for the other coils. Figure 5.7(d) shows the root sum of the squares of the actual sensitivity functions; SOS assumes that the sum is constant over the entire image, but the figure reveals that this assumption is not accurate. Figures 5.7(e)-(h) compare the original image and reconstructed images using SENSE with the proposed technique, SENSE with SOS, and GRAPPA.³ In this experiment, the k -space data were subsampled using an acceleration factor of $A = 2$ in the k_y dimension. The contrast in the SOS SENSE and GRAPPA reconstructions is not as good as the reconstruction using our approach, and the SNR (measured with respect to the original image) is much lower. This is due to the SOS assumption being wrong towards the center of the image as shown in Figure 5.7(d), thus resulting in wrong image magnitudes at the center of the reconstructed images.

Figure 5.8 presents an experiment using *actual* data from an eight-channel head array coil. In this experiment, the full k -space data has dimensions $N = M = 256$ and the autocalibration data size is $N' = M' = 64$. As in the previous experiment, we use an acceleration factor of $A = 2$ in the k_y dimension. Figures 5.8(a)-(c) compare the reconstructed images using SENSE with our approach, SENSE with SOS, and GRAPPA. The reconstruction using the proposed technique is observed to have much better contrast than the SOS SENSE and GRAPPA reconstructions towards the center of the image. In particular, we observe that the SOS reconstruction has an artifact at the center of the image. This is an aliasing error due to wrong sensitivity estimates toward the center

³The implementation of GRAPPA used in this work was produced by Dr. Jim Ji of Texas A & M University, and is available online at http://www.ece.tamu.edu/~mrs1/JIMJI_TAMU/pulsarweb/.

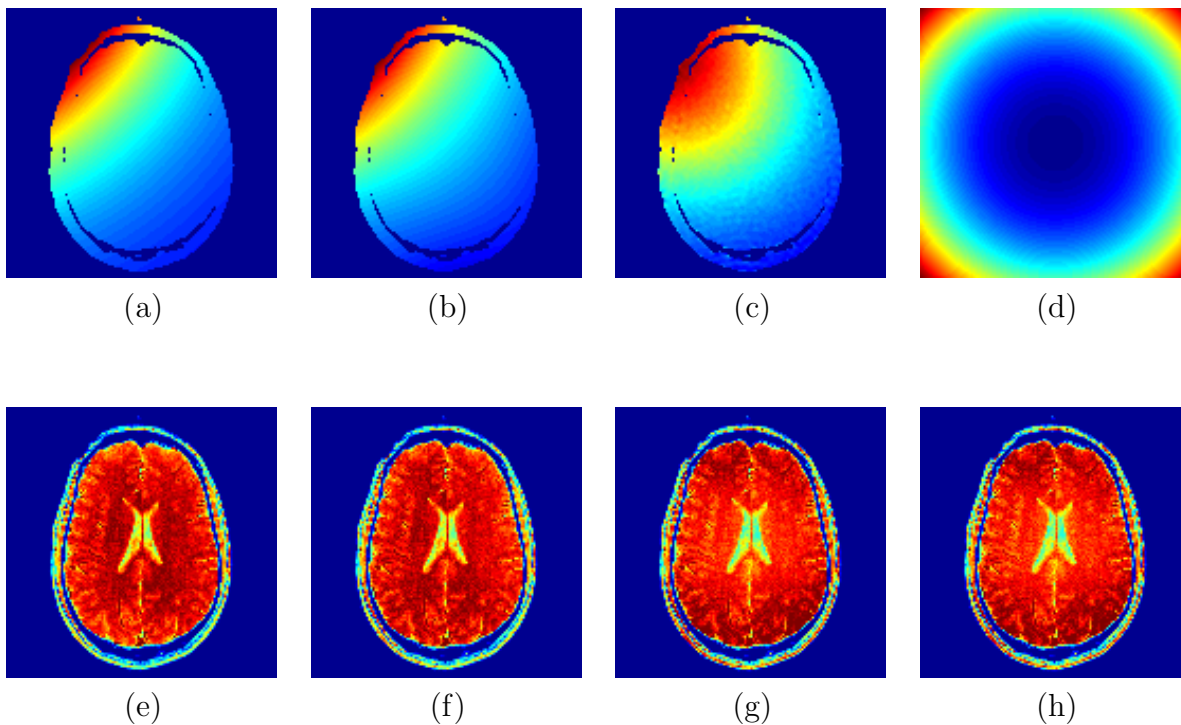


Figure 5.7 Experiment using *simulated* sensitivity functions for an eight-channel head array coil, where the full-resolution image function is $N = 128$ by $M = 128$ pixels. An acceleration factor of $A = 2$ is used along the k_y -dimension, and a $N' = 64$ by $M' = 64$ block of autocalibration data is collected from each coil. In addition, additive white complex Gaussian noise with variance $NM(0.01a)^2$ (where a is the peak pixel magnitude) has been applied to the k -space data from each coil. (a) Applied sensitivity function for coil 4, (b) estimated sensitivity function using the proposed technique, (c) SOS sensitivity estimate, (d) the root sum of the squares of all the sensitivity functions (note that this is not constant over the image), (e) original image, (f) reconstructed image using SENSE with sensitivity estimates from our method (SNR = 26.30 dB), (g) SENSE reconstruction with the SOS sensitivity estimates (SNR = 17.10 dB), and (h) GRAPPA reconstruction (SNR = 17.06 dB).

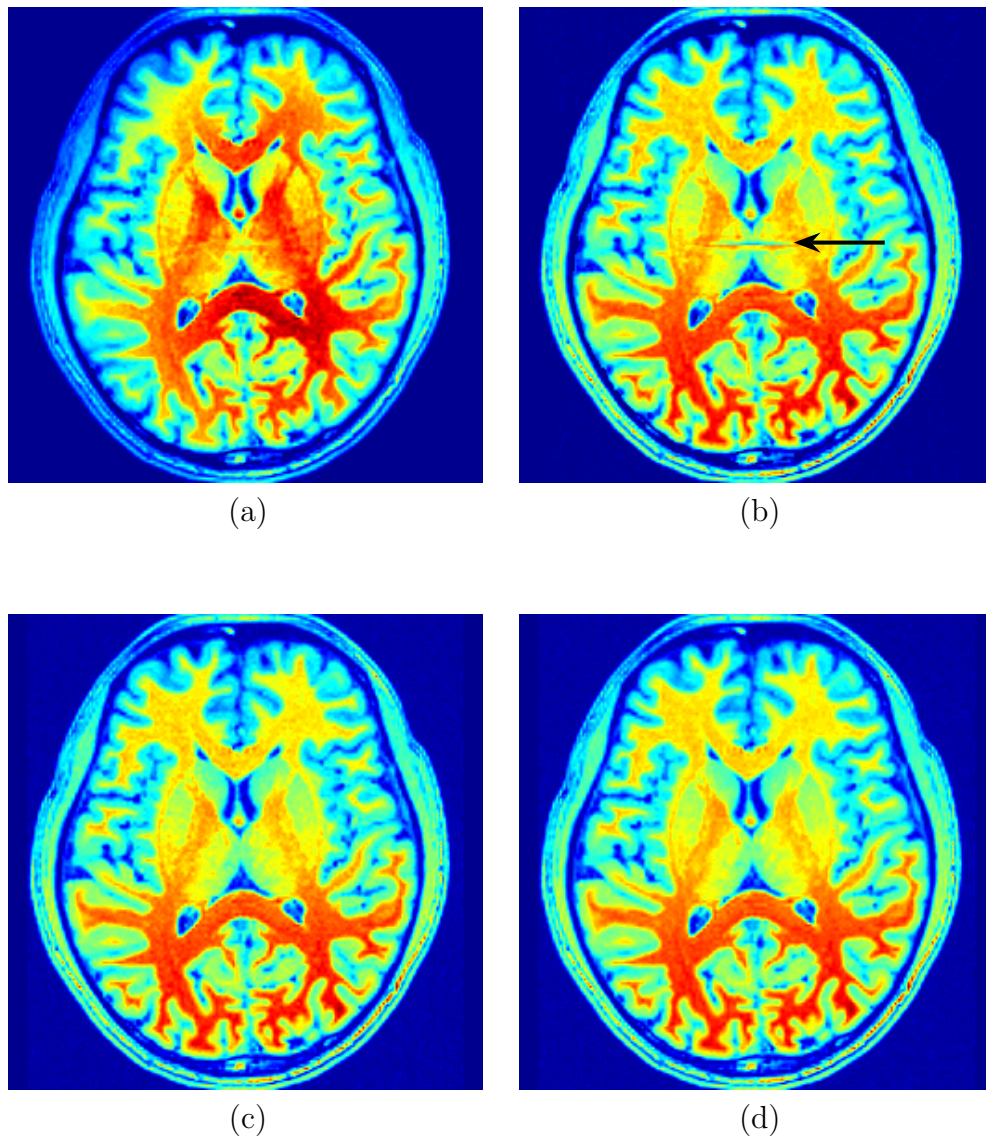


Figure 5.8 Experiment using *actual* data from an eight-channel head array coil, where $A = 2$, $N = M = 256$, and $N' = M' = 64$: (a) SENSE image reconstruction using sensitivity estimates from the proposed technique, (b) SENSE reconstruction using SOS sensitivity estimates, (c) GRAPPA reconstruction, and (d) image reconstruction formed by applying SOS to the full k -space data where no subsampling is assumed ($N' = M' = 256$ and $A = 1$). Note the aliasing artifact at the center of the SOS SENSE reconstruction in (b) (indicated by the arrow), which is due to wrong sensitivity estimates towards the image center; in the proposed reconstruction (a), such artifacts are reduced, and the contrast is improved towards the center of the image in comparison with (b)-(d).

Table 5.1 SNR (dB) of the image reconstruction using the proposed technique versus acceleration factor and autocalibration data size. The SNR, using SOS estimates, is shown in parentheses for comparison.

N', M'	$A = 2$	$A = 4$	$A = 8$
32	21.68 (11.94)	10.71 (9.32)	6.48 (-2.92)
64	22.17 (12.05)	10.87 (10.60)	6.82 (-4.62)
128	27.98 (12.08)	11.29 (11.82)	7.12 (-1.87)

of the image. It comes from the edge of the brain being aliased to the center. For comparison, Figure 5.8(d) shows the reconstruction produced by SOS using the full k -space data from each coil ($N' = M' = 256$ and $A = 1$). The result demonstrates that even in the best case where all of the k -space data are available, the SOS reconstruction has poorer contrast than the proposed reconstruction. In Table 5.1, we compare the reconstructed image quality using our approach under different acceleration factors A and autocalibration data sizes N', M' . The SNR of the reconstructed images is measured with respect to a gold standard image formed by applying the proposed technique to the full k -space data from each coil (i.e., $N' = M' = 256$ and $A = 1$). The SNR of the reconstructions using the SOS estimates is also shown in parentheses for comparison. We observe that the performance under both approaches degrades as the acceleration factor increases.

CHAPTER 6

CONCLUSION

6.1 Summary

This dissertation addressed modern image restoration methodologies for computed imaging. The goal of the work was to create approaches that moved the effort of imaging system calibration and error correction away from the physical hardware realm and into the signal processing realm. Such an approach reduces expensive hardware modifications and provides greater flexibility. The dissertation was focused on problems in two imaging modalities: the autofocus problem in synthetic aperture radar (SAR), and the problem of estimating coil sensitivities in parallel magnetic resonance imaging (PMRI). A common thread in both problems is their inherent multichannel nature. By explicitly exploiting the multichannel structure of the problems, novel algorithms were developed providing improved restoration performance.

6.1.1 Autofocus by sharpness optimization

We have presented analytical results providing new insight into metric-based methods for the restoration of SAR images. Considering the intensity-squared metric, and a dominant point-targets image model, we have derived a simple approximation for the resulting objective function. We demonstrated, in general, that a single-column image model does not correspond to a stationary point. Thus, we observed that it is not the sharpness metric alone that makes these approaches successful, but the reinforcement of metric minima that takes effect with many image columns; it is here that the multi-

channel defocusing model of SAR autofocus is exploited implicitly. The necessity of the implicit multichannel assumption suggested that a means for exploiting the multichannel condition *explicitly* was needed.

We also demonstrated that the multivariate objective function has a special structure near the perfectly focused image: it is approximately a separable function of the phase perturbations. As a consequence, when the phase errors are small, the metric minima are displaced from the origin by an amount equal to the phase errors. This allows the phase error to be estimated by performing M 1-D searches along each coordinate direction simultaneously. The analysis provides a formal justification for observations and assumptions in recent work [17, 18].

6.1.2 A multichannel approach to SAR autofocus

We have proposed a new subspace-based approach to the synthetic aperture radar (SAR) autofocus problem, termed the MultiChannel Autofocus (MCA) algorithm. In this approach, an image focusing operator is determined directly using a linear algebraic formulation. Assuming that a small portion of the perfectly focused image is zero-valued, or corresponds to a region of low return, near-perfect restorations of the focused image are possible without requiring prior assumptions about the underlying scene; the success of existing autofocus approaches tends to rely on the accuracy of such prior assumptions, such as the suitability of image sharpness metrics or the presence of isolated point scatterers. In practice, the desired image support condition can be achieved by exploiting the spatially limited nature of the illuminating antenna beam.

The MCA approach is computationally efficient, and robust in the presence of noise and deviations from the ideal image support assumption. The restoration quality of the proposed method is independent of the severity of the phase error function; existing autofocus approaches sometimes perform poorly when the phase errors are large and rapidly-varying. In addition, the vector-space formulation of MCA allows sharpness metric optimization to be incorporated into the restoration framework as a regularization term, enabling SAR autofocus to be cast into a more unified paradigm with other image

restoration problems. Here, the parameter set over which the optimization is performed is greatly reduced in comparison to the number of unknown phase error components. We have presented experimental results, using actual and simulated SAR images, demonstrating that the proposed technique can produce superior restorations in comparison with existing autofocus approaches.

6.1.3 Multichannel estimation of coil sensitivities

We have proposed a novel subspace-based technique for estimating coil sensitivities in PMRI. By exploiting the multichannel nature of the problem, where multiple acquisitions of the same image function are obtained with different sensitivity encodings, a subspace-based framework for directly solving for the sensitivity functions is obtained. The multichannel relationship is used to form a subspace where the sensitivity functions reside. To obtain unique sensitivity estimates within this subspace, the unknown sensitivity functions are expressed in terms of a known polynomial basis expansion, allowing the polynomial coefficients of the coil sensitivity functions to be determined using a linear algebraic formulation. Our method does not rely on the SOS assumption used in previous approaches, and thus avoids potential problems such as poor contrast and aliasing artifacts associated with previous approaches. In addition, the proposed restoration procedure is noniterative, computationally efficient, and applicable both to cases where pilot scans are available or where autocalibration data are collected with each scan. Experimental results using actual and simulated data demonstrate improved performance in comparison with existing approaches.

6.2 Future Directions

6.2.1 Extensions to SAR autofocus

In our work in the autofocus problem, we have assumed that the imaged scene is in the far-field relative to the radar platform, so that the wavefronts impinging upon the

scene are planar. Through the far-field assumption, the demodulated pulses are related to the *linear* projection through the scene. A more general case of interest is where the scene is in the near-field. In this case, a different model for the image formation process must be considered [53]; the demodulated pulses here provide projection data along curved wavefronts instead of along a line [54]. The framework for and approaches to the autofocus problem must be reconsidered in this more challenging scenario.

An application of current interest to both homeland security and national defense is *See-Through-The-Wall Imaging* [55], where low-frequency radars, attached to moving vehicles, are used to image the interiors of buildings. This situation poses unique challenges due to the spatially varying permittivity of walls, which imposes unknown signal delays on the received signals. The signal delays produce phase shifts in the imaging data that must be corrected to form a well-focused image [55]. Thus, the problem has a similar flavor to the SAR autofocus problem. Exporting the frameworks and methods for autofocus developed here might be of benefit to this unique application.

In this dissertation, a monostatic imaging scenario has been assumed, where the radar transmitter and receiver are colocated. Recently, there has been renewed interest in multistatic radar and passive radar. In multistatic radar, multiple transmitters and receivers are used, allowing for novel interferometric SAR and 3-D imaging applications [1]. Passive radar uses multiple radio and television transmitters as “illuminators of opportunity” to covertly form images of moving aircraft without actively transmitting signals [56]. In this application, the trajectory of the target must be accurately estimated to form useful imagery. In initial work on this problem, we have found the defocusing effects due to trajectory inaccuracies to be very stressing. Autofocus for passive radar is especially challenging because the illuminating signals are highly narrowband, transcribing very thin arcs of data in the 2-D Fourier plane (analogous to radio astronomy) [56–58]. Thus, the multichannel assumption used in MCA is no longer available, and likewise, existing autofocus techniques cannot be directly applied. However, there is a redundancy in the phase errors associated with each receiver, due to the common trajectory of the

target, that should be exploited to create an extension of SAR autofocus applicable to the passive case.

In spotlight-mode SAR, the range of look angles (i.e., the angles of the projection data) is often assumed to be small relative to the radar carrier frequency [1]. As a result, the multichannel defocusing model can be utilized, where each row of the SAR imaging data is assumed to have only a constant phase shift applied. When the range of angles is large, then the defocusing effect produced by the phase errors on each pulse is spatially varying, i.e., the phase errors are no longer a 1-D function of the cross-range frequencies. If an inverse DFT is applied directly to the demodulated pulses without first performing polar-to-Cartesian interpolation, the resulting image will be a warped version of the true image [1]. In this warped version of the image, the multichannel condition is satisfied. This suggests that MCA can be applied to the warped image first to estimate the phase errors; with the phase errors in hand, the regular image formation process using polar-to-Cartesian interpolation can then be performed. We have performed initial simulations using simulated images where this approach is found to be successful.

In our study of SAR autofocus, we have neglected the problem of *motion compensation*. In cases where the transmitted SAR pulses cannot be approximated as narrowband signals, the effect of the signal delays on each received pulse is to impart a linear phase ramp that varies with the range frequencies, resulting in different shifts along the range dimension for each cross-range frequency. Motion compensation is concerned with estimating the unknown linear phase terms associated with each pulse, while autofocus estimates the constant phase offsets; these procedures are usually performed as two separate steps in the image formation sequence [1]. Techniques for motion compensation are often heuristic (e.g., cross-correlation of range bins to align dominant scatterers). It may be beneficial to integrate both motion compensation and autofocus into a single unified procedure using the frameworks developed in this dissertation.

Lastly, the implementation of MCA within an actual SAR image formation chain, and the evaluation of its performance, is of great importance in enabling the technique to achieve widespread use.

6.2.2 Extensions to optical coherence tomography

Optical coherence tomography (OCT) uses backscattered light to form an image of the susceptibility of an object [59, 60]. In [59], a mathematical model for the inverse scattering problem in OCT has been derived that allows the image to be reconstructed using a linear transformation of the acquired data; here, the distortions inherent to previous hardware-based image formation approaches are reduced using digital means. In practice, system measurement errors can produce constant phase and group delay errors in the acquired signals that result in an incorrect restoration of the object [61, 62]. These effects can be modeled as multiplicative phase errors in the OCT data, analogous to the SAR autofocus problem [61]. An approach for correcting the phase errors using a coverslip as a reference reflector has been proposed [61]. However, it is of interest to develop an algorithmic approach to the phase correction that does not rely on a physical coverslip [62]. The development of such an approach would provide an opportunity to export some of the technologies proposed here for SAR to OCT.

REFERENCES

- [1] C. V. Jakowatz, Jr., D. E. Wahl, P. H. Eichel, D. C. Ghiglia, and P. A. Thompson, *Spotlight-Mode Synthetic Aperture Radar: A Signal Processing Approach*. Boston: Kluwer Academic Publishers, 1996.
- [2] D. C. Munson, Jr., J. D. O'Brien, and W. K. Jenkins, "A tomographic formulation of spotlight-mode synthetic aperture radar," *Proceedings of the IEEE*, vol. 71, no. 8, pp. 917–925, August 1983.
- [3] J. Walker, "Range-doppler imaging of rotating objects," *IEEE Transactions on Aerospace and Electronic Systems*, vol. AES-16, pp. 23–52, January 1980.
- [4] D. C. Munson, Jr. and R. L. Visentin, "A signal processing view of strip-mapping synthetic aperture radar," *IEEE Transactions on Acoustics, Speech, and Signal Processing*, vol. 37, no. 12, pp. 2131–2147, December 1989.
- [5] C. E. Mancill and J. M. Swiger, "A map drift autofocus technique for correcting higher order SAR phase errors," presented at the Tri-Service Radar Conference, Monterey, California, June 23-25, 1981.
- [6] W. D. Brown and D. C. Ghiglia, "Some methods for reducing propagation-induced phase errors in coherent imaging systems – I: Formalism," *J. Opt. Soc. Amer. A*, vol. 5, pp. 924–942, 1988.
- [7] D. C. Ghiglia and W. D. Brown, "Some methods for reducing propagation-induced phase errors in coherent imaging systems – II: Numerical results," *J. Opt. Soc. Amer. A*, vol. 5, pp. 943–957, 1988.
- [8] T. C. Calloway and G. Donohoe, "Subaperture autofocus for synthetic aperture radar," *IEEE Transactions on Aerospace and Electronic Systems*, vol. 30, no. 2, pp. 617–621, April 1994.
- [9] P. H. Eichel, D. C. Ghiglia, and C. V. Jakowatz, Jr., "Speckle processing method for synthetic-aperture-radar phase correction," *Optics Letters*, vol. 14, no. 1, pp. 1101–1103, January 1989.
- [10] C. V. Jakowatz, Jr. and D. E. Wahl, "Eigenvector method for maximum-likelihood estimation of phase errors in synthetic-aperture-radar imagery," *Journal of the Optical Society of America A*, vol. 10, no. 12, pp. 2539–2546, December 1993.
- [11] D. E. Wahl, P. H. Eichel, D. C. Ghiglia, and C. V. Jakowatz, Jr., "Phase gradient autofocus—a robust tool for high resolution SAR phase correction," *IEEE Transactions on Aerospace and Electronic Systems*, vol. 30, no. 3, pp. 827–835, July 1994.

- [12] R. G. Paxman and J. C. Marron, "Aberration correction of speckled imagery with an image sharpness criterion," in *Statistical Optics, Proceedings of the SPIE*, vol. 976, San Diego, CA, 1988, pp. 37–47.
- [13] F. Berizzi and G. Corsini, "Autofocusing of inverse synthetic aperture radar images using contrast optimization," *IEEE Transactions on Aerospace and Electronic Systems*, vol. 32, no. 3, pp. 1185–1191, July 1996.
- [14] L. Xi, L. Guosui, and J. Ni, "Autofocusing of ISAR images based on entropy minimization," *IEEE Transactions on Aerospace and Electronic Systems*, vol. 35, no. 4, pp. 1240–1252, October 1999.
- [15] J. Fienup and J. J. Miller, "Aberration correction by maximizing generalized sharpness metrics," *Journal of the Optical Society of America A*, vol. 20, no. 4, pp. 609–620, April 2003.
- [16] R. L. Morrison, Jr. and D. C. Munson, Jr., "An experimental study of a new entropy-based SAR autofocus technique," in *Proc. of the IEEE International Conference on Image Processing*, vol. II, Rochester, NY, 2002, pp. 441–444.
- [17] M. P. Hayes and S. A. Fortune, "Recursive phase estimation for image sharpening," in *Image and Vision Computing New Zealand*, Dunedin, New Zealand, 2005.
- [18] T. J. Kragh, "Monotonic iterative algorithm for minimum-entropy autofocus," in *Proc. Adaptive Sensor Array Processing (ASAP) Workshop*, Lexington, MA, June 2006.
- [19] R. L. Morrison, Jr., "Entropy-based autofocus for synthetic aperture radar," M.S. thesis, University of Illinois at Urbana-Champaign, 2002.
- [20] W. Hoen and R. L. Morrison, Jr., "Atmospheric phase error measurement and correction for the haystack ultra-wideband satellite imaging radar (HUSIR)," in *Proc. IEEE Radar*, Boston, MA, April 2007, to appear.
- [21] C. V. Jakowatz, Jr., (private communication), 2003.
- [22] Z. Liang and P. C. Lauterbur, *Principles of Magnetic Resonance Imaging: A Signal Processing Perspective*. New York: IEEE Press, 2000.
- [23] R. M. Heidemann, M. A. Griswold, A. Haase, and P. M. Jakob, "VD-AUTO-SMASH imaging," *Magnetic Resonance in Medicine*, vol. 45, pp. 1066–1074, 2001.
- [24] M. A. Griswold, P. M. Jakob, R. M. Heidemann, M. Nittka, V. Jellus, J. Wang, B. Kiefer, and A. Haase, "Generalized autocalibrating partially parallel acquisitions (GRAPPA)," *Magnetic Resonance in Medicine*, vol. 47, pp. 1202–1210, 2002.
- [25] K. P. Pruessmann, M. Weiger, M. B. Scheidegger, and P. Boesiger, "SENSE: Sensitivity encoding for fast MRI," *Magnetic Resonance in Medicine*, vol. 42, pp. 952–962, 1999.
- [26] A. Papoulis, "Generalized sampling expansion," *IEEE Transactions on Circuits and Systems*, vol. CAS-24, no. 11, pp. 652–654, 1977.

- [27] J. Ji, J. B. Son, M. P. McDougall, and S. M. Wright, “Highly accelerated parallel imaging methods for localized massive array coils: Comparison using 64-channel phased array data,” in *Proc. of the IEEE International Symposium on Biomedical Imaging*, Arlington, VA, April 2006, pp. 734–737.
- [28] R. L. Morrison, Jr., M. N. Do, and D. C. Munson, Jr., “SAR image autofocus by sharpness optimization: A theoretical study,” submitted to *IEEE Transactions on Image Processing*, 2006.
- [29] R. A. Muller and A. Buffington, “Real-time correction of atmospherically degraded telescope images through image sharpening,” *Journal of Optical Society of America*, vol. 64, no. 9, pp. 1200–1209, 1974.
- [30] C. T. Kelley, *Iterative Methods for Optimization*. Philadelphia: SIAM, 1999.
- [31] T. G. Kolda, R. M. Lewis, and V. Torczon, “Optimization by direct search: New perspectives on some classical and modern methods,” *SIAM Review*, vol. 45, no. 3, pp. 385–482, 2003.
- [32] D. G. Luenberger, *Linear and Nonlinear Programming*. Boston: Kluwer Academic Publishers, 2003.
- [33] R. L. Morrison, Jr. and M. N. Do, “Multichannel autofocus algorithm for synthetic aperture radar,” in *Proc. of the IEEE International Conference on Image Processing*, Atlanta, GA, 2006, pp. 2341–2344.
- [34] R. L. Morrison, Jr. and M. N. Do, “A multichannel approach to metric-based SAR autofocus,” in *Proc. of the IEEE International Conference on Image Processing*, vol. 2, Genoa, Italy, 2005, pp. 1070–1073.
- [35] R. L. Morrison, Jr., D. C. Munson, Jr., and M. N. Do, “Avoiding local minima in entropy-based SAR autofocus,” in *Proc. of the IEEE Signal Processing Workshop on Statistical and Array Processing*, St. Louis, MO, 2003, pp. 454–457.
- [36] D. C. Munson, Jr. and J. L. C. Sanz, “Image reconstruction from frequency-offset Fourier data,” *Proceedings of the IEEE*, vol. 72, no. 6, pp. 661–669, June 1984.
- [37] J. W. Goodman, *Statistical Optics*. New York: John Wiley and Sons, 1985.
- [38] H. Stark and J. W. Woods, *Probability, Random Processes, and Estimation Theory for Engineers*. Upper Saddle River, NJ: Prentice Hall, 1994.
- [39] W. Feller, *An Introduction to Probability Theory and Its Applications*. New York: John Wiley and Sons, 1968.
- [40] R. L. Morrison, Jr., M. N. Do, and D. C. Munson, Jr., “MCA: A multichannel approach to SAR autofocus,” submitted to *IEEE Transactions on Image Processing*, 2007.
- [41] L. Tong and S. Perreau, “Multichannel blind identification: From subspace to maximum likelihood methods,” *Proceedings of the IEEE*, vol. 86, no. 10, pp. 1951–1968, October 1998.

- [42] M. Gurelli and C. Nikias, "EVAM: An eigenvector-based algorithm for multichannel blind deconvolution of input colored signals," *IEEE Transactions on Signal Processing*, vol. 43, no. 1, pp. 134–149, January 1995.
- [43] G. Harikumar and Y. Bresler, "Blind restoration of images blurred by multiple filters: Theory and efficient algorithms," *IEEE Transactions on Image Processing*, vol. 8, no. 2, pp. 202–219, 1999.
- [44] G. H. Golub and C. F. Van Loan, *Matrix Computations*. Baltimore: Johns Hopkins University Press, 1996.
- [45] R. A. Horn and C. R. Johnson, *Matrix Analysis*. New York: Cambridge University Press, 2005.
- [46] M. Soumekh, *Synthetic Aperture Radar Signal Processing with MATLAB Algorithms*. New York: John Wiley, 1999.
- [47] R. E. Blahut, *Theory of Remote Image Formation*. Cambridge: Cambridge University Press, 2004.
- [48] M. I. Skolnik, *Introduction to Radar Systems*. New York: McGraw-Hill, 2002.
- [49] M. Vetterli and J. Kovacevic, *Wavelets and Subband Coding*. New Jersey: Prentice Hall, 1995.
- [50] R. L. Morrison, Jr., M. Jacob, and M. N. Do, "Multichannel estimation of coil sensitivities in parallel MRI," in *Proc. of the IEEE International Symposium on Biomedical Imaging*, Arlington, VA, April 2007.
- [51] L. Ying, J. Sheng, and B. Liu, "Joint estimation of image and coil sensitivities in parallel MRI," in *Proc. of the IEEE International Symposium on Biomedical Imaging*, 2006, pp. 17–20.
- [52] F. Lin, "SENSE: Sensitivity-Encoding MRI MATLAB Tools," January 2007, www.nmr.mgh.harvard.edu/~fhlin/tool_sense.htm.
- [53] D. L. Mensa, *High Resolution Radar Imaging*. Dedham, MA: Artech House, 1981.
- [54] S. Xiao, "Topics in CT and SAR imaging: Fast backprojection algorithms and optimal antenna spacings," Ph.D. dissertation, University of Illinois at Urbana-Champaign, 2001.
- [55] J. A. Marble and A. O. Hero, "Phase distortion correction for see-through-the-wall imaging radar," in *Proc. of the IEEE International Conference on Image Processing*, Atlanta, GA, October 2006, pp. 2333–2336.
- [56] Y. Wu and D. C. Munson, Jr., "Multistatic synthetic aperture imaging of aircraft using reflected television signals," in *Algorithms for Synthetic Aperture Radar Imagery VIII*, Orlando, FL, April 2001, pp. 1–12.
- [57] O. Arikan and D. C. Munson, Jr., "A tomographic formulation of bistatic synthetic aperture radar," in *Proc. of ComCon 88, Advances in Communications and Control Systems*, Baton Rouge, LA, October 1988, pp. 289–302.

- [58] A. R. Thompson, J. M. Moran, and G. W. Swenson, Jr., *Interferometry and Synthesis in Radio Astronomy*. New York: John Wiley and Sons, 2001.
- [59] T. S. Ralston, D. L. Marks, S. P. Carney, and S. A. Boppart, “Inverse scattering for optical coherence tomography,” *Journal of the Optical Society of America A*, vol. 23, no. 5, pp. 1027–1037, May 2006.
- [60] T. S. Ralston, D. L. Marks, S. P. Carney, and S. A. Boppart, “Interferometric synthetic aperture microscopy,” *Nature Phys.*, submitted 2007.
- [61] T. S. Ralston, D. L. Marks, S. P. Carney, and S. A. Boppart, “Phase stability technique for inverse scattering in optical coherence tomography,” in *Proc. of the IEEE International Symposium on Biomedical Imaging*, Arlington, VA, April 2006, pp. 578–581.
- [62] T. S. Ralston, (private communication), 2006.

AUTHOR'S BIOGRAPHY

Robert Lee Morrison Jr. was born in Voorhees, New Jersey, on January 19, 1977. His family moved to Sioux City, Iowa in 1978, where he spent his formative years. He graduated from the University of Iowa in 2000 with a degree in electrical engineering. Under the direction of Prof. David C. Munson Jr., he completed his Master of Science in electrical engineering from the University of Illinois at Urbana-Champaign in 2002. Upon completion of his master's degree, he conducted his Ph.D. dissertation work under the supervision of Prof. Minh N. Do. After finishing his Ph.D., Robert will begin work as a member of the technical staff at the Massachusetts Institute of Technology Lincoln Laboratory.